Optogenetic regulation of osmolarity and water flux

Doctoral thesis for a doctoral degree

in Julius-Maximilians-Universität Würzburg

Fei Lin

From Fujian, China

Würzburg, 2023

Submitted on: ……………………………………………………..

Members of the Promotionskomitee:

Chairperson:

Primary Supervisor: Prof. Dr. Georg Nagel

Secondary Supervisor: Prof. Dr. Knut Kirmse

Date of Public Defense: …………………………………….……

Date of Receipt of Certificates: ……………………………………

Contents

Abstract

Optogenetics is a powerful technique that utilizes light to precisely regulate physiological activities of neurons and other cell types. Specifically, light-sensitive ion channels, pumps or enzymes are expressed in cells to enable their regulation by illumination, thus allowing for precise control of biochemical signaling pathways.

The first part of my study involved the construction, optimization, and characterization of two optogenetic tools, KCR1 and NCR1. Elena Govorunova et al. discovered a light-gated potassium channel, KCR1, in the protozoan *Hyphochytrium catenoides*. Traditional potassium ion channels are classified as either ligand-gated or voltage-gated and possess conserved pore-forming domains and K^+-selective filters. However, KCR1 is unique in that it does not contain the signature sequence of previously known K^+ channels and is a channelrhodopsin. We synthesized the KCR1 plasmid according to the published sequence and expressed it in *Xenopus* oocytes. Due to the original KCR1 current being too small, I optimized it into KCR1 2.0 to improve its performance by fusing LR (signal peptide LucyRho, enhances expression) at the N-terminal and T (trafficking signal peptide) and E (ER export signal peptide) at the C-terminal. Additionally, I investigated the light sensitivity, action spectrum, and kinetics of KCR1 2.0 in *Xenopus* oocytes. The potassium permeability of KCR1 2.0, $P_K/P_{na} \cong 24$, makes KCR1 2.0 a powerful hyperpolarizing tool that can be used to inhibit neuronal firing in animals.

Inspired by KCR1, we used the KCR1 sequence as a template for gene sequence alignment with the sequences in *H. catenoides*. We found that NCR1 and KCR1 have similar gene sequences. NCR1 was characterized by us as a light-gated sodium channel. This NCR1 was also characterized and published by Govorunova et al. very recently, with the name *HcCCR*. Due to the original NCR1 current being too small, I optimized it into NCR1 2.0 to improve its performance by fusing LR at the N-terminal and T and E at the C-terminal, which significantly improved the expression level and greatly increased the current amplitude of NCR1. Full-length NCR1 2.0 contains 432 amino acids. To test whether the number of amino acids changes the characteristics of NCR1 2.0, we designed NCR1 2.0 (330), NCR1 2.0 (283), and NCR1 2.0 (273) by retaining the number of amino acids at 330, 280, and 273 in NCR1 2.0, respectively. As the number of amino acids decreased, the current in NCR1 2.0 increased. I also investigated the light sensitivity, action spectrum, and kinetics of NCR1 2.0 (273) in the *Xenopus*

oocytes. We performed four point mutations at amino acid positions 133 and 116 of NCR1 2.0 and analyzed the reversal potentials of the mutants. The mutations were as follows: NCR1 2.0 (273 D116H), NCR1 2.0 (273 D116E), NCR1 2.0 (283 V133H), and NCR1 2.0 (283 D116Q).

The second part of this study focuses on light-induced water transport using optogenetic tools. We explored the use of optogenetic tools to regulate water flow by changing the osmolarity in oocytes. Water flux through AQP1 is driven by the osmotic gradient that results from concentration differences of small molecules or ions. Therefore, we seek to regulate ion concentrations, using optogenetic tools to regulate the flux of water non-invasively. To achieve this, I applied the light-gated cation channels XXM 2.0 and NCR1 2.0 to regulate the concentration of Na^+, while K^+ channel KCR1 2.0 was used to regulate K^+ concentration. As Na^+ flows into the *Xenopus* oocytes, the membrane potential of the oocytes becomes positive, and Cl^- can influx through the light-gated anion channel *Gt*ACR1. By combining these optogenetic tools to regulate NaCl or KCl concentrations, I can change the osmolarity inside the oocytes, thus regulating the flux of water. I co-expressed AQP1 with optogenetic tools in the oocytes to accelerate water flux. Overall, I designed three combinations (1: AQP1, XXM 2.0 and *Gt*ACR1. 2: AQP1, NCR1 2.0 and *Gt*ACR1. 3: AQP1, KCR1 2.0 and *Gt*ACR1) to regulate the flow of water in oocytes. The shrinking or swelling of the oocytes can only be achieved when AQP1, light-gated cation channels (XXM 2.0/NCR1 2.0/KCR1 2.0), and light-gated anion channels (*Gt*ACR1) are expressed together. The illumination after expression of either or both alone does not result in changes in oocyte morphology.

In sum, I demonstrated a novel strategy to manipulate water movement into and out of *Xenopus* oocytes, non-invasively through illumination. These findings provide a new avenue to interfere with water homeostasis as a means to study related biological phenomena across cell types and organisms.

Zusammenfassung

Die Optogenetik ist eine leistungsstarke Technik, die Licht zur präzisen Regulierung der physiologischen Aktivitäten von Neuronen und anderen Zelltypen einsetzt. Konkret werden Licht-empfindliche Ionenkanäle, Pumpen oder Enzyme in Zellen exprimiert, um ihre Regulierung durch Belichtung zu ermöglichen und so eine präzise Kontrolle biochemischer Signalwege zu ermöglichen.

Der erste Teil meiner Studie umfasste die Konstruktion, Optimierung und Charakterisierung von zwei optogenetischen Werkzeugen, KCR1 und NCR1. Elena Govorunova und Mitarbeiter entdeckten einen lichtgesteuerten Kaliumkanal, KCR1, in dem Protozoen *Hyphochytrium catenoides*. Herkömmliche Kalium-Ionenkanäle werden entweder als ligandengesteuert oder spannungsgesteuert klassifiziert und verfügen über konservierte porenbildende Domänen und K^+-selektive Filter. KCR1 ist jedoch insofern einzigartig, als er nicht die Signatursequenz der bisher bekannten K^+-Kanäle enthält und ein Kanalrhodopsin ist. Wir synthetisierten das KCR1-Plasmid entsprechend der veröffentlichten Sequenz und exprimierten es in *Xenopus*-Oozyten. Da der ursprüngliche KCR1-Strom zu klein war, optimierte ich ihn zu KCR1 2.0, um seine Leistung zu verbessern, indem LR (Signalpeptid LucyRho, verbessert die Expression) am N-Terminus und T (Trafficking-Signalpeptid) und E (ER-Export-Signalpeptid) am C-Terminus fusioniert wurden. Außerdem untersuchte ich die Lichtempfindlichkeit, das Wirkungs-Spektrum und die Kinetik von KCR1 2.0 in *Xenopus*-Oozyten. Die Kaliumpermeabilität von KCR1 2.0, $P_K/P_{Na} \cong 24$, macht KCR1 2.0 zu einem leistungsfähigen hyperpolarisierenden Werkzeug, das zur Hemmung von Nervenzellen in Tieren eingesetzt werden kann.

Inspiriert von KCR1 verwendeten wir die KCR1-Sequenz als Vorlage für den Gen-Sequenzabgleich mit Sequenzen in *H. catenoides*. Wir fanden heraus, dass NCR1 und KCR1 ähnliche Gensequenzen haben. NCR1 wurde von uns als lichtgesteuerter Natriumkanal charakterisiert. NCR1 wurde ebenfalls von Govorunova et al. charakterisiert und vor kurzem unter dem Namen *Hc*CCR veröffentlicht. Da der ursprüngliche NCR1-Strom zu gering war, optimierte ich ihn zu NCR1 2.0, um seine Leistung zu verbessern, indem ich LR am N-Terminus und T und E am C-Terminus fusionierte, was das Expressionsniveau erheblich verbesserte und die Stromamplitude von NCR1 stark erhöhte. NCR1 2.0 in voller Länge enthält 432 Aminosäuren. Um zu testen, ob die Anzahl der Aminosäuren die Eigenschaften von NCR1 2.0 verändert,

haben wir NCR1 2.0 (330), NCR1 2.0 (283) und NCR1 2.0 (273) entwickelt, indem wir die Anzahl der Aminosäuren auf 330, 280 bzw. 273 in NCR1 2.0 verkürzt haben. Mit abnehmender Anzahl der Aminosäuren nahm der Strom in NCR1 2.0 zu. Ich untersuchte auch die Licht-Empfindlichkeit, das Wirkungsspektrum und die Kinetik von NCR1 2.0 (273) in *Xenopus*-Oozyten. Wir führten vier Punktmutationen an den Aminosäurepositionen 133 und 116 von NCR1 2.0 durch und analysierten die Umkehrpotentiale der Mutanten. Die Mutationen waren wie folgt: NCR1 2.0 (273 D116H), NCR1 2.0 (273 D116E), NCR1 2.0 (283 V133H), und NCR1 2.0 (283 D116Q).

Der zweite Teil dieser Studie konzentriert sich auf den lichtinduzierten Wassertransport mit Hilfe optogenetischer Methoden. Wir untersuchten den Einsatz optogenetischer Werkzeuge zur Regulierung des Wasserflusses durch Veränderung der Osmolarität in Oozyten. Der Wasserfluss durch AQP1 wird durch den osmotischen Gradienten angetrieben, der durch Konzentrationsunterschiede kleiner Moleküle oder Ionen entsteht. Daher versuchen wir, die Ionenkonzentration mit optogenetischen Mitteln zu regulieren, um den Wasserfluss nicht-invasiv zu steuern. Zu diesem Zweck verwendete ich die lichtgesteuerten Kationenkanäle XXM 2.0 und NCR1 2.0 zur Regulierung der Na^+-Konzentration, während der K^+-Kanal KCR1 2.0 zur Regulierung der K^+-Konzentration eingesetzt wurde. Wenn Na^+ in die *Xenopus*-Oozyten fließt, wird das Membranpotential der Oozyten positiv, und Cl^- kann durch den lichtgesteuerten Anionenkanal *Gt*ACR1 einströmen. Durch die Kombination dieser optogenetischen Werkzeuge zur Regulierung der NaCl- oder KCl-Konzentration kann ich die Osmolarität innerhalb der Oozyten verändern und so den Wasserfluss regulieren. Ich habe AQP1 zusammen mit optogenetischen Werkzeugen in den Oozyten exprimiert, um den Wasserfluss zu beschleunigen. Insgesamt habe ich drei Kombinationen entwickelt (1: AQP1, XXM 2.0 und *Gt*ACR1. 2: AQP1, NCR1 2.0 und *Gt*ACR1. 3: AQP1, KCR1 2.0 und *Gt*ACR1) zur Regulierung des Wasserflusses in den Eizellen. Das Schrumpfen oder Anschwellen der Oozyten kann nur erreicht werden, wenn AQP1, lichtgesteuerte Kationenkanäle (XXM 2.0/NCR1 2.0/KCR1 2.0) und lichtgesteuerte Anionenkanäle (*Gt*ACR1) gemeinsam exprimiert werden. Die Belichtung nach Expression von einem oder beiden allein führt nicht zu Veränderungen der Morphologie der Oozyten.

Zusammenfassend lässt sich sagen, dass ich eine neuartige Strategie zur nicht-invasiven Beeinflussung der Wasserbewegung in und aus *Xenopus*-Oozyten durch Licht demonstriert habe. Diese Ergebnisse eröffnen einen neuen Weg zur Beeinflussung der Wasserhomöostase als Mittel zur Untersuchung verwandter biologischer Phänomene in verschiedenen Zelltypen und Organismen.

1 Introduction

1.1 Aquaporin

Aquaporins (AQPs), also referred to as water channels, are integral membrane proteins that play a crucial role in the transportation of water molecules across cell membranes. The water channel protein "aquaporin-1(AQP1)" was first identified by Peter Agre at the Johns Hopkins University in 1992, and it was named CHIP 28[1]. Water channels are channel proteins that are ubiquitous in both animals and plants and facilitate the movement of water in response to osmotic gradients [2]. Compared to water diffusion through phospholipid bilayers, water molecules pass through AQPs at a faster rate. The direction of water flow through AQPs is dependent on the concentration of the osmotic gradient, with water moving from regions of low to high osmotic potential [3-4]. The osmotic gradient results from differences in solute concentration, which drives water movement across cell membranes. AQPs remain constitutively open and functional under normal conditions, even in the absence of light.

The flow of water through AQPs is regulated by the osmotic gradient, such that if the concentration of solutes inside the cell is larger than outside, the cell will absorb water through the water channel; otherwise, water will exit the cell. AQPs play a key role in facilitating water transport in tissues with a high water content, such as the kidney [5]. Moreover, AQPs are involved in many physiological processes in the human body, including diabetes insipidus, urine transfer, nerve excitation, cell migration, cell proliferation, brain edema, and others [6-7].

1.1.1 Aquaporin-1 (AQP1) structure

Aquaporins are a family of small, integral membrane proteins with a basic structure that is about 30 kDa in size [8-9]. The first water channel to be discovered was isolated from the human red blood cell membrane and was initially named CHIP28, but later renamed AQP1 after its function was analyzed [2-3]. The AQP1 structure is composed of six transmembrane helices (I-VI) connected by five loops (loops A-E), which can be identified by hydrophilic plot analysis of the primary sequence (Figure 1.1a). The transmembrane helix of AQP1 is composed of two sections, with one part of the loop situated on the extracellular side and the other part located on the cytoplasmic side of the cell membrane. Loops A, C, and E are exposed to the extracellular environment, while loops B and D face the cytoplasmic side of the membrane. Within the water channel, there are two tandem repeating structures that comprise the ends of the amino

and carboxyl terminals, which are designated I-III and IV-VI, respectively. The fundamental repeating unit of AQP1 consists of conserved loops B and E.

This conserved loop is composed of three transmembrane helices and a second transmembrane helix. It contains a conserved signature sequence called NPA (Asparagine-Proline-Alanine). An α-helix, which is formed by loop B and loop E, is situated within the cell membrane. While loop B extends through the cytoplasm to the interior of the cell membrane, loop E extends through the extracellular side to the interior of the cell membrane. Loop B and loop E form the seventh transmembrane helix. The two NPAs in the ring are oriented at a 180° to create water-conducting channels (Figure 1.1b) [10].
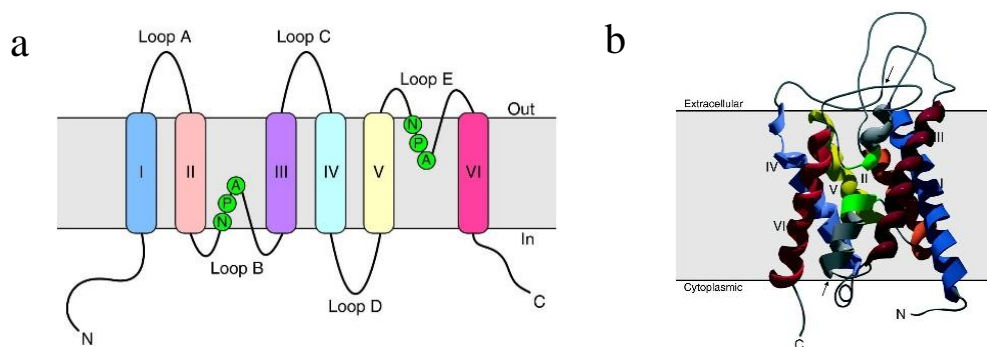
Fig 1.1 Structure of AQP1.

(a) Diagram of AQP1 transmembrane structure. AQP1 is composed of six transmembrane helices (I-VI) connected by five loops (A-E), with two internal tandem repeats (I-III and IV-VI). Loops B and E contain conserved NPA motifs and form short alpha helices that fold back into the membrane from opposite sides. The amino-terminal is located at the N-terminal and the carboxyl-terminal is located at the C-terminal. (b) 3D structure of an AQP1 subunit monomer. The structure consists of 6 tilted membrane helices (I-VI) and two pore-forming domains, made up of two short alpha helices that enter the membrane from the extracellular and intracellular surfaces (indicated by black arrows). The two NPA boxes are shown in green. The amino- and carboxyl-terminal domains are oriented towards the cytoplasmic side of the membrane. This figure is taken from Kruse, E., et al [11].

The structural model of AQP1 has been verified by Cryogenic electron microscopy, as reported in literature [12]. AQP1 is composed of four subunits that form a circular pore, allowing water to pass through. In general, the basic structure of the water channel is a tetramer, with each monomer allowing the passage of water. However, recent experimental studies have demonstrated that the pores of AQP1 can also generate ion conductance when certain ions are present [13-14].

1.1.2 Mechanism of Water transport

Aquaporins share a similar structure with a high degree of similarity in common regions. The pore-forming region is hypothesized to have multiple transport mechanisms for water molecule transport. The hydrophobic region, formed by loop B and loop E, is restricted by the type and size of the substrate, and has a number of conserved hydrophobic residues. Water molecules are able to pass through this region in the form of hydrogen bonds, with the molecules being linked together in a single chain [15]. The AQP1 pore has two constriction-limiting sites, the first being the conserved aromatic region of the arginine residue (Arg195), which constructs the smallest part of the pore [16]. The second site is formed by the highly conserved NPA motif, where water molecules can interact easily with the asparagine residue. When a water molecule interacts with the NPA motif, the two sites form an electrostatic barrier that prevents protons from passing through the pore [17]. The permeability and selectivity of AQPs vary greatly, and their protein activity is also highly variable in different plant species [18].

1.2 Optogenetic toolbox

Optogenetics is a powerful technique that utilizes light to precisely regulate physiological activities of neurons and other cell types. This approach involves the expression of light-sensitive ion channels, pumps, or enzymes in the target cells that can be modulated by specific wavelengths of light. By activating these light-sensitive tools, the biochemical signaling pathways of the cells can be precisely controlled [19]. Optogenetic tools are not limited to light-gated ion channels but also include light-activated pumps and microbial rhodopsins. The application of optogenetics in animal nervous systems has led to significant advancements in our understanding of various physiological processes, such as fear memories [20], mating [21], feeding [22], decision-making [23], and locomotion [24].

1.3 Light-gated ion channels

Ion channels include voltage-gated ion channels, ligand-gated ion channels, mechanosensitive ion channels, and temperature-gated ion channels. Light-gated ion channels are a group of transmembrane proteins that form ion channels, with pores that open in response to light and close in darkness. They form pores in the phospholipid bilayer membrane, and when the protein undergoes a conformational change upon light

stimulation, the ion channels open and ions flow according to the electrochemical gradient [25]. Light-gated ion channels were also synthesized in the laboratory but the natural light-gated ion channels, such as Channelrhodopsin-2, were most successful as optogenetic tools [26, 29].

1.3.1 Channelrhodopsin-2

Channelrhodopsin-1 (ChR1) and Channelrhodopsin-2 (ChR2) are the first discovered rhodopsins from the model organism *Chlamydomonas reinhardtii*. These rhodopsins have been expressed in *Xenopus* oocytes, and their functions were identified by Nagel et al. in 2002 and 2003 [27-29].

The channel rhodopsins are *retinylidene* proteins that contain seven transmembrane helices. These proteins contain the chromophore all-trans retinal, which is an *aldehyde derivative* of vitamin A that can be isomerized. Upon absorption of photons, all-trans retinal is converted to 13-cis retinal. The pore of rhodopsin opens by at least 6 Å, and within a few milliseconds, the 13-cis retinal returns to all-trans retinal, closing the pore. Most natural channel rhodopsins are non-specific cation channels that are able to pass through various cations such as Na^+, K^+, and Ca^{2+} [29-30].
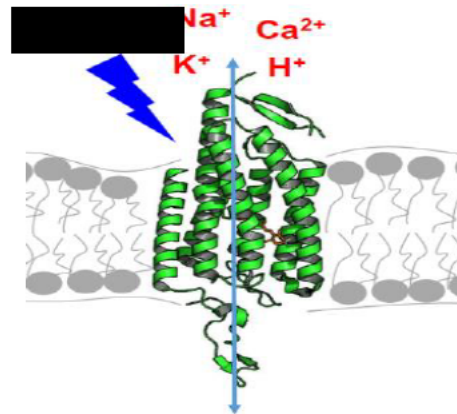
Fig 1.2 Structure of Channelrhodopsin-2.
The structure of Channelrhodopsin-2 (ChR2) consists of seven transmembrane helices connected by three extracellular loops and three intracellular loops. The retinal chromophore is covalently bound to a conserved lysine residue in the seventh transmembrane helix. This figure is taken from Kato, H.E., et al [31].

In order to fulfill diverse experimental requirements, ChR2 has undergone specific improvements through mutagenesis at various sites by researchers. Mutant ChR2 channels have shown significant performance changes compared to the wild-type ChR2.

For instance, after mutation, ChR2 C128 and D156 mutants exhibited enhanced light sensitivity and faster channel closing kinetics [32-33].

The D156C (ChR2-XXL) and D156H (ChR2-XXM) mutants displayed much larger currents compared to the wild-type ChR2. Furthermore, XXM has faster kinetics than XXL and is more permeable to Na^+ and Ca^{2+} than both wild-type ChR2 and XXL [34]. The E90R mutant of ChR2 switches cation conductance to anion conductance [35]. By fusing the enhance expression signaling peptide, the trafficking signaling peptide, and the export signaling peptide to XXM, XXM 2.0 exhibited a larger current than XXM [36].

Fig 1.3 Photocurrent comparison of different ChR2-XXM variants.
(a) Photocurrents were recorded in response to 1 s blue light stimulation, two days after injection in ND96 buffer. The blue light used had a wavelength of 473 nm and an intensity of 3 mW/mm^2. (b) Current statistics of different ChR2-XXM variants were recorded at a holding potential ranging from -100 to 20 mV. This figure is taken from Ruijing Tang [36].
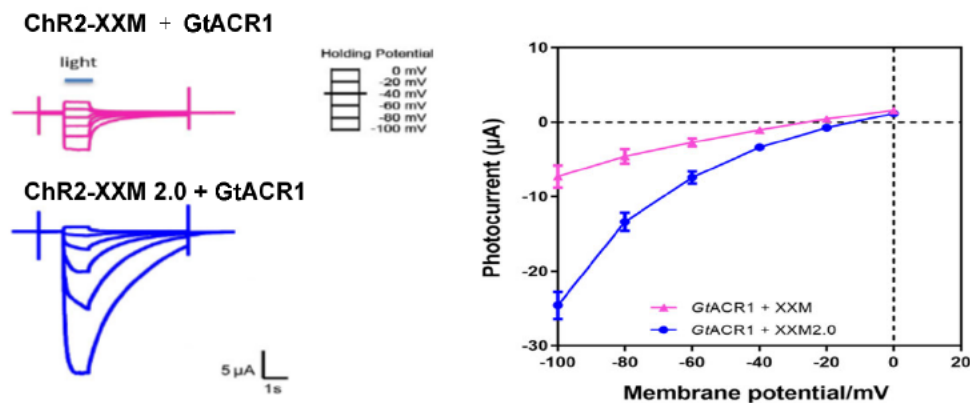
1.3.2 Light-gated anion channels (*Gt*ACR1)

Anion channel rhodopsins (ACRs) are a class of light-gated anion channels discovered in the cryptophyte alga *Guillardia theta*. Two types of ACRs, *Gt*ACR1 and *Gt*ACR2, have been identified based on their distinct properties. *Gt*ACR1 is permeable to both chloride and bromide ions, with a larger permeability for chloride ions under light illumination [25]. *Gt*ACR1 has been widely used for neuronal silencing in various organisms, such as *Drosophila* [37-40], mice [41-44], zebrafish [45], and worms [46]. Compared to other silencing tools, *Gt*ACR1 exhibits excellent features. It generates larger currents under low light illumination than reported natural microbial rhodopsins. Additionally, *Gt*ACR1 has a high expression level and can be easily expressed in

animals and plants. Moreover, its closing kinetics are relatively slow, enabling long-term silencing of neurons.

1.3.3 The structure of *Gt*ACR1

The crystal structure of *Gt*ACR1 has been determined using continuous grid scanning X-ray diffraction and molecular replacement techniques, achieving a resolution of 2.9 Å [47]. *Gt*ACR1 is composed of two monomers linked by disulfide bonds to form a homodimeric structure. Each monomer consists of an extracellular cap domain, 7 transmembrane helices (TM1-TM7), and a cytoplasmic loop at the C-terminal. The amino terminal of the terminal fragment contains two kinked α-helices, while β-hairpins originate from the TM2-3 loop, meeting at the membrane interface. The stability of the *Gt*ACR1 structure is mainly dependent on the interaction between TM3 and TM4, as well as the disulfide bond formed with the C6 residue [48]. The intermolecular disulfide bond is crucial for maintaining the stability of the structure. The helices of TM5, TM6, and TM7 are longer than those of TM1, TM2, TM3, and TM4, giving the structure a funnel-shaped model with a wide opening on one.
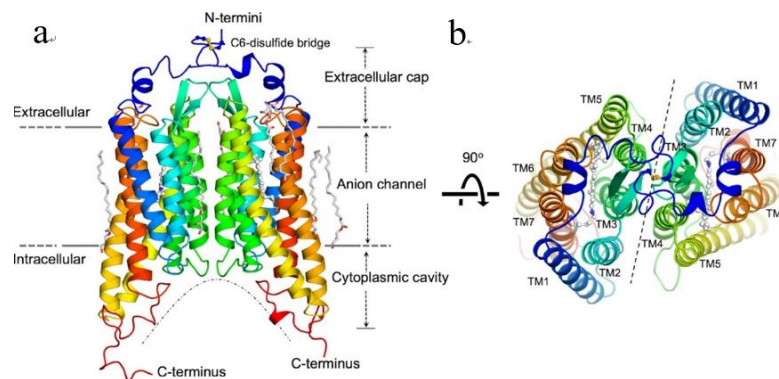
Fig 1.4 Structure of *Gt*ACR1 homodimer.

(a) Side view of *Gt*ACR1 transmembrane domain. The *Gt*ACR1 protomer is depicted in cartoon format, with the N-terminal labeled in blue and the C-terminal labeled in red. The transmembrane region of *Gt*ACR1 consists of seven helices, and intermolecular disulfide bonds are connected by C6 (yellow sticks). (b) Top view of *Gt*ACR1. This figure is taken from Li, Hai, et al [48].

1.3.4 Light-gated potassium channel (KCR1)

Traditional potassium ion channels can be classified into two types: ligand-gated and voltage-gated. They possess conserved pore-forming domains and K^+ selective filters, as well as highly conserved K^+ channel signature sequences [49-52]. These sequences are mainly found in eukaryotic cell, bacterial, archaeal, and viral potassium ion

channels, which are regulated by ligands, voltage, pH, membrane potential, or temperature [49, 52].

KCR is a newly discovered light-gated potassium channel that does not require an additional K^+-selective filter and exhibits fast kinetics [53]. KCR was found in the catenoids of the *protist Hyphochytrium* and has been named KCR1 and KCR2 based on their distinct properties. Both KCR1 and KCR2 are channel rhodopsins with a much larger selectivity for potassium ions over sodium ions. KCR is active for a very short time with a photoactivation kinetic time of 1 ms [54]. KCR1 has been shown to inhibit the firing of cortical neurons in rats by discharging on their excitatory cells [53]. The formation of electrochemical gradients leads to membrane hyperpolarization in neurons, making KCR1 a potent hyperpolarising tool. Therefore, KCR1 is extremely useful in studying neurological and cardiovascular diseases.

1.3.5 The structure of KCR1
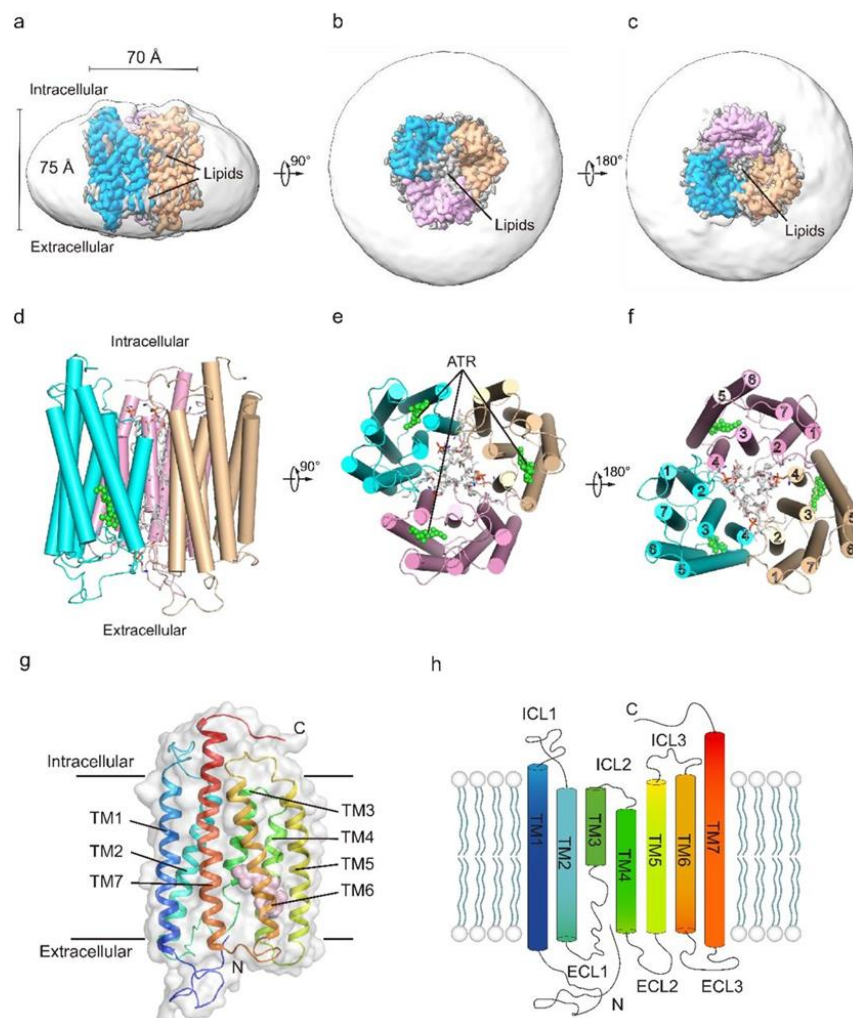
Fig 1.5 Structure of KCR1.

(a) Planar view of the trimer membrane of KCR1. (b) The extracellular side view. (c) The intracellular side view. The detergent is transparent. The three subunits are labelled white, pink and cyan. The color of the central pseudo-pore lipids is grey. (d-f) The color of all-trans retinal (ATR) is green and the transmembrane helical model of the three subunits. (g-h) Helical model and cartoon model of a single subunit. Three extracellular linkers (ECL1-ECL3) at the C-terminal, three intracellular linkers (ICL1-ICL3) at the N-terminal. This figure is taken from Zhang, Mengchen, et al [55].

The molecular structure of KCR1 was determined by Cryogenic electron microscopy at a resolution of 3.17 Å (Fig 1.5a-c) [55]. This high-resolution map was used to construct the model of KCR1, which includes ions, waters, amino acids, and lipids [55]. The structure of KCR1 is similar to the trimer structure of ChRmines [56-57], and a dimer model is not applicable for the activation of non-selective ion channels (Fig 1.5a-f) [58, 31]. Each monomer of KCR1 comprises seven transmembrane helices (TM1-TM7), three extracellular linkers (ECL1-ECL3), three intracellular linkers (ICL1-ICL3), an intracellular C-terminal domain, and an extracellular N-terminal canonical rhodopsin topology (Fig 1.5g-h). The central pseudo-pore of ChRmines is formed by a single lipid layer, while that of KCR1 uses two lipid layers. The interaction between monomers is primarily through amino acid and lipid interactions within each monomer (Fig 1.6a-c). The N-terminal of KCR1 can insert into the pseudo-pore to stabilize the trimer (Fig 1.6d-e). The trimer interface is formed by TM2 and TM3 helices, which combine with TM4 (Fig 1.6f-g). Lipids from the extracellular layer of the cell can also insert into the trimer interface [55]. Furthermore, all-trans-retinal is tightly bound to the trimer (Fig 1.6a-f).

Fig 1.6 Structure of KCR1 and ChRmine.

(a) Top view of the KCR1 membrane. (b) The KCR1 pseudo-pore has two lipid layers, whereas the ChRmine pseudo-pore has only a single lipid layer. Restriction sites of KCR1 (black arrows): P2 and Y4. Restriction sites for ChRmine: I106 and F104. (c-e) Relationship between pseudo-pore radius an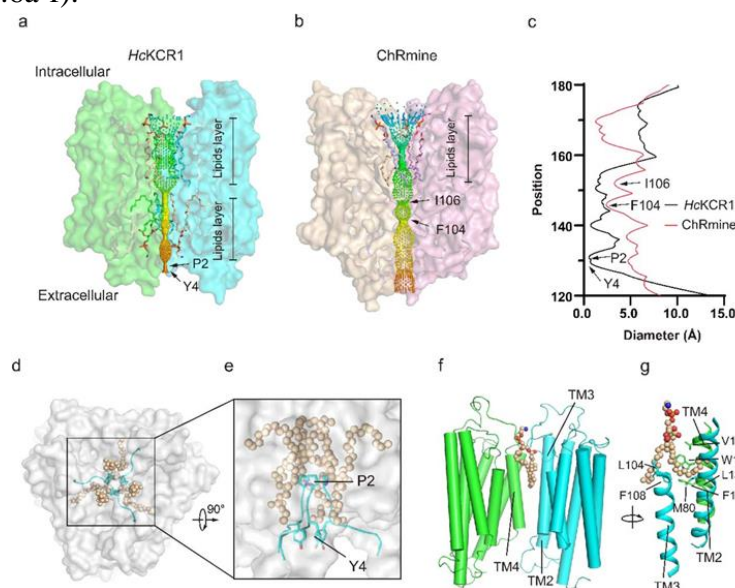d intracellular distance, pseudo-pore including lipids and residues, viewed from outside the cell membrane. View of the structure of KCR1 from different angles. (f-g) Amino acids are indicated by black arrows. This figure is taken from Zhang, Mengchen, et al [55].

1.3.6 High sodium conductance channelrhodopsin (NCR1)

Since the discovery of KCR1 and KCR2, they have drawn the attention of numerous researchers. To investigate the similarities and differences between KCR1 and other gene sequences from the *H. catenoides* group, we used KCR1 as a control template. Our findings revealed that NCR1, a sodium ion channel, shares a similar gene sequence with KCR1, but differs in its permeability to potassium ions [54]. In contrast to KCR1 and KCR2, NCR1 does not exhibit high permeability to potassium ions [59], and is more selective for sodium ions than for potassium ions [54]. Although KCR1, KCR2, and NCR1 are unique and highly homologous light-gated channels, they possess different relative permeabilities for sodium and potassium ions. Experiments have been conducted to characterise the performance of NCR1, and attempts have been made to enhance its permeability for sodium by mutagenesis.

1.4 Light-activated pump rhodopsins
1.4.1 Light-activated proton pumps

Bacteriorhodopsin (BR) is the first type I rhodopsin found in microbes. It was discovered in 1971 by Oesterhelt et al. from *Halobacterium halobium* [60-61], later correctly identified as *Halobacterium salinarum*. This light-activated protein functions as an outward-directed H^+ ion pump, which can pump protons out of the cell under light illumination [62-63]. The change in proton concentration creates a proton gradient, and the formation of the osmotic gradient promotes the transmembrane flux of water and other ions. BR also plays a role in ATP synthesis and other transport coupling processes [60, 64-65]. The structure of BR has been extensively studied by researchers at the end of the 20th century, and the knowledge of its structure facilitates the study of other light-gated channels [66-72]. Another pump, Bacteriorhodopsin-type Archaerhodopsin-3, that pumps hydrogen to the outside, has been found in *Halorubrum*

sodomense, which is also able to amplify and silence the nerves [73-75]. The pump from *Leptosphaeria maculans* is a blue light-sensitive pump that silences nerve cells when exposed to blue light [76]. Recently, a different type of pump that pumps hydrogen ions into cells with larger proton-pumping performance than BR has been discovered, such as NsXeR and PoXeR [77-78]. BR was first expressed in oocytes by Nagel et al. in 1995, and the expressed BR showed a current after being exposed to light, marking the beginning of optogenetics [79].

1.4.2 Light-activated chloride pumps

The discovery and utilization of BR led researchers to discover another type of rhodopsin in *Halobacterium salinarum* in 1977, named *Halorhodopsin (HsHR)* [80-81]. Initially, HR was believed to be a sodium pump, but further experimentation revealed that it is actually a chlorine pump [82-85]. Light-driven chloride pumps, such as HR, have emerged as a class of optogenetic tools that allow for precise spatiotemporal control of chloride ion influx and efflux in various biological systems [75]. After the identification of *HsHR*, researchers discovered in *Natronomonas pharaonis Np*HR [86, 87]. The purification and expression of *Np*HR is easier than that of *HsHR*, and *Np*HR has shown better performance with a more stable photocurrent when exposed to light compared to *HsHR* [88-89]. *Np*HR is a light-activated, inward-directed chloride pump. In order to further improve its performance, researchers have modified the sequence for better expression in the plasma membrane and less accumulation in the endoplasmic reticulum. The modified *Np*HR 2.0 has a larger current compared to *Np*HR after the addition of an ER export signal peptide to the *Np*HR sequence, with a decrease in the amount of *Np*HR2.0 aggregated on the endoplasmic reticulum [90-91]. However, even with these modifications, *Np*HR2.0 is still unable to effectively inhibit nerve excitation due to the strong excitation of the neurons. Therefore, further modification of *Np*HR2.0 is necessary. The addition of a traffic signal (T) from the potassium ion channel Kir2.1 at the C-terminal of *Np*HR2.0 forms the modified *Np*HR3.0, which has a larger efficiency in targeting to the plasma membrane and a stronger inhibition of nerve excitation. To further optimize *Np*HR performance and increase its potency and expression, *Np*HR4 and *Np*HR5 have been continuously improved and introduced [88]. *Np*HR is a light-driven chloride pump that has been extensively studied due to its potential applications in neuroscience and other fields. This protein is derived from the bacterium Natronomonas pharaonis, and its

structure and function have been extensively characterized through various experimental techniques [35].

1.4.2.1 Structure of *Np*HR

*Np*HR and *Hs*HR share similar gene sequences, but their structures are distinctly different, and the timing of their structural identification also differs [92-95]. The protein structure of *Np*HR consists of seven transmembrane helices (H1-H7) that together form a channel across the cell membrane. The N-terminal resides in the cytoplasm, while the C-terminal is located in the extracellular space. The retinal chromophore is covalently bound to a lysine residue situated in the middle of helix H7 [96] (Fig 1.7a). Among these helices, there is a half-helix originating from the N-terminal known as the A-helix [95]. The A, B, and C helices interact to form the hydrophobic cap, which can separate the extracellular environment from the active site. In Figure 1.7b, the main chloride ion-binding site is formed by the interaction between the Schiff's base and D252. The other important residues for chloride ion binding include T126 and S130 [97-99]. In the dark, *Np*HR inhibits neurons by polarizing the neuronal membrane [100]. The transport mechanism of *Np*HR has been studied extensively over the years [80, 84, 101-102, 103-105]. In the resting state, the retinal chromophore of *Np*HR is in an all-trans configuration. Upon illumination with yellow or amber light (wavelengths around 590-600 nm), the retinal chromophore undergoes a photo isomerization to a 13-cis configuration, which induces a conformational change in the protein structure [106-108]. Overall, *Np*HR serves as a light-activated chloride pump that allows for the selective inhibition of neural activity in response to light stimulation. The detailed structure and working mechanism of *Np*HR have been thoroughly characterized, making it a powerful tool for optogenetic research.
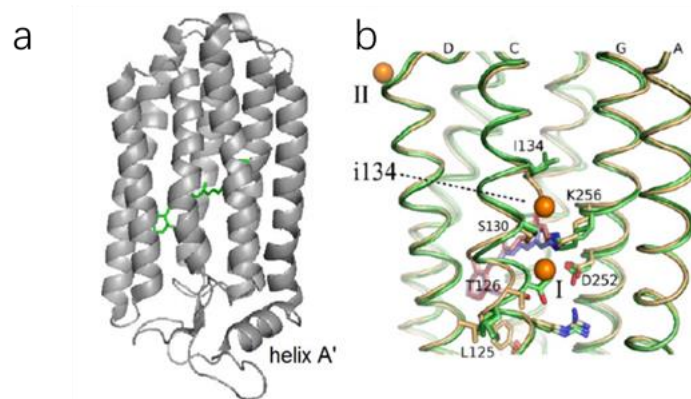

Fig 1.7 Structure and binding site of *Np*HR.

(a) The structure of *Np*HR consists of seven transmembrane helices (grey), with helix A located at the N-terminal, and a retinal chromophore (green) [95]. (b) Bromide binding sites of *Np*HR are located in various spirals in the resting state [97]. Bromine binding sites near T126 are present in both subunits I and II. Assisted movement of T126 and I134 allows bromine to move and bond to I134 [98].This figure is taken from Shang, Yang [96].

1.4.3 Light-activated sodium pump rhodopsin

For a significant period of time after the discovery of bacteriorhodopsin (BR), the light-driven sodium pumps it was capable of remained a mystery. However, a covalent bond is formed through the combination of BR with the protonated Schiff base and ATR as revealed by chemical fundamentals analysis. Sodium ions are positively charged, which makes them repel each other, thereby preventing the pump from transporting them [109-110]. In 2013, Inoue, K and his research team discovered the first light-activated sodium pump from the marine flavor bacterium *Krokinobacter eikastus*, which they named KR2 [111-113]. The presence of KR2 led the researchers to hypothesize a mechanism where the protonated Schiff base is shielded temporarily by D116 in the resting state, neutralizing the Schiff base charge and enabling sodium ions to pass through easily [114-116]. KR2 is an efflux-pumping sodium channel that has been extensively analyzed in terms of its structure and function. Its ratio of sodium to hydrogen ion permeability is approximately 8000 [112-113, 117]. In addition to KR2, researchers have identified several other sodium-pumping channels, including TrNaR1, TrNaR2, GLR, SrNaR, NdNaR, NdR2, and NyNaR [118-121]. Grimm, C, and colleagues optimized and transformed KR2 at its N and C termini, resulting in a modified KR2 with greater current flow and stronger membrane targeting. This modified KR2 was successfully applied to silent experiments in mouse hippocampal neurons [122]. However, the application of KR2 in animals and plants is limited due to its poor membrane targeting, low current flow, and tendency to aggregate intracellularly.

1.5 Enzyme rhodopsins toolbox

The rhodopsin enzyme is a widespread biomolecule in nature and the first rhodopsin enzyme discovered is named *Be*GC1. *Be*GC1, a rhodopsin guanylyl cyclase, was found in the fungus *Blastocladiella emersonii*. The structure of *Be*GC1 includes a guanylyl cyclase catalytic domain and a microbial rhodopsin domain [76]. BeGC1 was expressed

in various cell types, including oocytes, HEK293 T cells, and neurons. After analyzing its performance characteristics, BeGC1 was renamed *Be*CyclOp, a cyclase opsin, by Gao, S. et al. BeGC1 was also expressed in Caenorhabditis elegans and its performance was analyzed by Scheib, U. et al, where it was renamed RhGC, a rhodopsin-guanylyl cyclase [123, 124]. The structure of *Be*CyClOp comprises eight transmembrane helices, with both N- and C-terminal cytosolic regions. *Be*CyClOp demonstrates a strong photoregulatory ability and can rapidly and precisely regulate the cyclic guanosine monophosphate (cGMP) signaling within cells [125]. Tian et al. discovered *Sr*RhoPDE (rhodopsin phosphodiesterase) in *Salpingoeca rosetta*, which has a strong hydrolytic activity on cGMP. *Sr*RhoPDE has eight transmembrane helices as well [126]. Moreover, *Cr*2c-Cyclop1 was discovered in *C. reinhardtii* and *Vc*2c-Cyclop1 was found in *V. carteri*. Tian et al. found that in both Cr2c-Cyclop1 and Vc2c-Cyclop1, light can inhibit guanylyl cyclase activity in an ATP-dependent manner. The combination of 2c-Cylop and Cyclop or *Sr*RhoPDE can be used to modulate cGMP signaling [127].

1.6 Objectives of this study

In my thesis, the characterization and analysis of KCR1 and NCR1 are the main focus. KCR1 is a non-conventional potassium ion channel, characterized by its light-gated properties and alternative K^+ selectivity mechanism. Due to the original KCR1 current being too small, I optimized it into KCR1 2.0 to improve its performance by fusing LR at the N-terminal and T and E at the C-terminal. The light sensitivity, action spectrum, kinetics, and ion selectivity of KCR1 2.0 were identified.

Similarly, NCR1 was optimized as NCR1 2.0 by fusing LR to its N-terminal and TYE to its C-terminal. Full-length NCR1 2.0 contains 432 amino acids. Different sequence lengths of NCR1 2.0 were designed and analyzed from light sensitivity, action spectrum, kinetics, and ion selectivity. Four point mutations were also performed at positions 116 and 133 of NCR1, resulting in NCR1 2.0 (273 D116H), NCR1 2.0 (273 D116E), NCR1 2.0 (283 V133H), and NCR1 2.0 (283 D116Q), and their properties will be characterized. In the second part, a light-sensitive water transport system was constructed by combining Aquaporin (AQP1), light-gated cation channels (XXM 2.0, NCR1 2.0, and KCR1 2.0), and a light-gated anion channel (*Gt*ACR1). XXM 2.0 and NCR1 2.0 were used to regulate Na^+ concentration while KCR1 2.0 was used for K^+ transport. *Gt*ACR1 facilitated the transport of Cl^-, and the combination of XXM 2.0 or

NCR1 2.0 and *Gt*ACR1 was used to regulate NaCl concentration. The combination of KCR1 2.0 and *Gt*ACR1 was used to regulate KCl concentration. The channels' functions were verified using TEVC. Heterologous AQP1 was expressed in the oocytes to accelerate water transport. An edema model was constructed using cells (oocytes), optogenetic tools, and solutions to regulate oocyte shrinking and swelling with time and spatial precision using light.

2 Material and methods

2.1 Materials and reagents

All materials and reagents are from Sigma Corporation unless otherwise specified (Table 2.1). Synthesis and optimisation of opsin genes for molecular cloning (Table 2.2).

Table 2.1 Reagents /Kit and Source

Reagents /Kit	Source
Plasmid extraction	QIAGEN
PCR purification	QIAGEN
Gel extraction	QIAGEN
Restriction enzymes	Thermo Fisher Scientific
Ligase enzyme	Thermo Fisher Scientific
DNA Polymerase	Thermo Fisher Scientific

Table 2.2 Genes and expression vector

Opsin genes/ Vector	Source
Aquaporins-1 (AQP1)	Red blood cells
XXM 2.0	*Chlamydomonas reinhardtii*
NCR1 2.0	*Protist Hyphochytrium*
KCR1 2.0	*Protist Hyphochytrium*
*Gt*ACR1	*Cryptophyte Guillardia theta*
pGem (vector)	Thermo Fisher Scientific

2.2 Molecular biology

2.2.1 *E.coli* culture and storage

The bacterial strain MRF of *E. coli* was cultured on LB agar plates or in LB solution as detailed in Table 2.3. The LB culture medium and LB agar plates have a shelf life of one month, after which they must be reconstituted. The LB solution contains a specific amount of antibiotics, which differ in storage concentration from the final use concentration (Table 2.4). *E. coli* was inoculated on LB agar plates and stored at 4 °C for an extended period. Small-scale cloning of *E. coli* was carried out in 15 mL/25 mL centrifuge tubes (SARSTEDT, Nuembrecht, Germany), whereas large-scale cultivation was performed in 250 mL Erlenmeyer flasks (SARSTEDT, Nuembrecht, Germany). The LB bacterial solution in test tubes and conical flasks was cultured in a rotary shaker

(G25 Incubator, New Brunswick Scientific) at 200 rpm with temperature control at 37 °C. Care was taken to avoid cross-infection of *E. coli* during the cultivation process.

Table 2.3 LB medium composition

Composition	Quantity
Yeast extract	2.5 g
Tryptone	5 g
NaCl	5 g
Agar (only for plate)	7.5 g
ddH$_2$O	500 mL

The medium needs to be autoclaved at 125 °C for 30 min.

Table 2.4 Ampicillin antibiotic concentration

Stock Solution	Final concentration
50 mg/mL	50 µg/mL

For short-term storage of *E. coli* bacteria, up to one week, it is recommended to store them in a refrigerator at 4°C. For long-term storage, it is recommended to mix the liquid *E. coli* bacteria with sterilized glycerol, quickly freeze the mixture using liquid nitrogen, and then store the frozen bacteria in a freezer at -80°C. This ensures the stability and viability of the bacteria during long-term storage. Proper labeling of the samples with the strain name, date of preparation, and storage conditions is important for easy identification and retrieval of the samples.

2.2.2 Competent *E. coli* cells

100 µL of Escherichia coli (*E. coli*) was added to a 50 mL centrifuge tube containing 20 mL of Luria-Bertani (LB) medium. The tube was then placed on a rotary shaker overnight. 1 mL of bacterial culture was subsequently transferred to a 100 mL Erlenmeyer flask containing 100 mL of LB medium. The flask was placed on a rotary shaker with a rotation speed of 220 rpm. When the optical density (OD) value of *E. coli* reached 0.3-0.5, the rotating oscillation was stopped. The *E. coli* culture was then transferred to a 50 mL centrifuge tube and resuspended twice with 0.1 M CaCl$_2$. The supernatant was discarded, and the pellet was resuspended with the resuspension buffer (Table 2.5) and placed on ice for 10 minutes. The bacterial suspension was transferred to 1.5 mL test tubes. 50 microliters of bacterial suspension was added to each test tube.

The 1.5 mL test tubes containing bacterial suspension were quickly frozen in liquid nitrogen and stored at -80°C.

Table 2.5 Resuspension buffer

Composition	Quantity
CaCl$_2$	0.1M
Glycerol	15 %

2.2.3 *E. coli* transformation

The plasmids were transformed into competent *E. coli* using the heat shock method. Competent *E. coli* were removed from the -80°C freezer and placed on ice for 20 minutes. Plasmids were then added to the 1.5 mL test tube containing competent *E. coli*, gently mixed, and kept on ice for 20-25 minutes. The tube was placed in a thermo cycler or a heat block at 42°C for 90 seconds, then removed and cooled on ice for 5 minutes. The cooled mixed bacterial solution was carefully spread onto the LB agar plate containing ampicillin and placed overnight in a constant temperature incubator set at 37°C. If the amount of plasmid is too low, the mixed bacteria can be added to the LB medium and incubated for 30 minutes to amplify the plasmids. The amplified mixture was then spread onto the LB agar plate containing ampicillin and incubated overnight in a constant temperature incubator set at 37°C.

2.2.4 Cracking of *E. coli* cells

To efficiently and accurately screen for the correct plasmid, it is necessary to lyse the *E. coli* cells after transformation with the plasmid, as a prerequisite to plasmid extraction. Lysis is commonly performed using a pre-prepared cracking buffer (Table 2.6). After incubation, the culture plate containing colonies of a specific size is removed and colony positions and serial numbers are marked. Subsequently, 10 µL of water is added to a small 1.5 mL tube and the colonies are transferred into the tube using a pipette tip. The colonies are then evenly dispersed in the lysate and incubated at room temperature for 10 minutes. The DNA loading buffer (Table 2.7) is added to the lysate, mixed gently, and the resulting mixture is loaded along with the standard control group onto DNA agarose gel (Table 2.8). The correct colony group is selected based on the band size of the standard control group. To expedite plasmid selection, at least three samples are taken from the correct colonies for plasmid amplification and subsequent extraction.

Table 2.6 Cracking buffer

Composition	Quantity
NaOH	0.1M
SDS	0.25%
Sucrose	10%

Table 2.7 DNA loading buffer (6x)

Composition	Quantity
Bromophenol blue	0.25%
Glycerol	30%
Store	4 ℃

Table 2.8 TAE for DNA Agarose gel (1x)

Composition	Quantity
EDTA	1 mM
Tris-base	40 mM
Acetic acid	20 mM

2.2.5 Polymerase Chain Reaction (PCR)

PCR testing of *E. coli* colonies is also a rapid method for screening the correct *E. coli* colonies. PCR experiments are conducted by mixing plasmids and target primers into *E. coli*, and colonies are deemed correct if the required target bands can be amplified. 10 µL of water is added to a 1.5 mL tube, and the colonies are transferred to the tube with a pipette tip and gently shaken. The tubes are labelled with a pen. The tube containing 10 µL of *E. coli* solution is placed in a thermo cycler or a heat block and incubated for 10 minutes at a temperature of 98 °C. After incubation, the tubes are centrifuged for 10 minutes at 14000 rpm, and the supernatant is retained as a template for PCR. The target primers and templates are mixed according to the ratio shown in Table 2.9 The PCR products mixed with DNA loading buffer are then loaded into a DNA agarose gel electrophoresis for analysis of the product bands. Colonies with correct bands are tested after completion of the PCR procedure (Table 2.10). Using pipette tips, three correct colonies are selected and added to a test tube containing LB solution with antibiotics and placed in a rotary shaker for overnight cultivation at a temperature of 37 °C. *E. coli* is used for the first two days of plasmid extraction. There are many methods for screening *E. coli* colonies for plasmids, including lysis and PCR

23

of *E. coli* cells, both of which are effective for quickly screening the correct colonies. The choice of method depends on the experimental requirements.

Table 2.9 PCR reaction buffer

Composition	Quantity
Template(DNA)	0.5 µL
5×HGD buffer	2.0 µL
dNTP (10 mM)	0.4 µL
Forward primer 1 (10 µM)	0.4 µL
Reverse primer 2 (10 µM)	0.4 µL
Phusion DNA Polymerase	0.1 µL
BSA	0.1 µL
ddH$_2$O	5.3 µL

Table 2.10 PCR procedure

Steps	Repeats	Temperature/°C	Duration/s
I		98	45
II	6	98	20
		72	20 per kb
III	6	98	20
		66	20
		72	20 per kb
IV	26	98	20
		56	20
		72	20 per kb

2.2.6 DNA extraction, ligation and sequencing

DNA extraction can be performed using two methods, namely extraction from *E. coli* after overnight culture and extraction from a DNA agarose gel. The Qiaprep spin miniprep kit (Qiagen, Hilden, Germany) was used to extract plasmids in this study. For *E. coli* extracted after overnight culture, the bacterial solution was centrifuged at 9000 rpm for 10 minutes, and the supernatant was discarded. Next, the bacterial solution was resuspended and transferred to a new tube, and the lysis solution was added to lyse the *E. coli*. After neutralizing the bacterial solution with Neutralization Solution and centrifugation, the QIAprepare 2.0 column was used to filter the bacterial fluid and

extract the plasmid. Finally, water was added dropwise to elute the plasmid. For DNA extracted from an agarose gel, the gel was first cut with a sharp scalpel under UV light and further purified using the QIAquick Gel Extraction Kit (Qiagen, Hilden, Germany). The cut agarose gel was then placed in a tube and added to lysis solution. The tubes were heated to 50 °C to dissolve the agarose gel, and the Minelute column was used to elute the desired fragments or plasmids. Water was added to the column to elute the required fragments. The QIAGEN Plasmid Midi Kit (Qiagen, Hilden, Germany) was used when larger amounts of plasmids were required. The concentration of the plasmids was measured using a nano photometer (Nano Photometer™, Implen, Munich, Germany). The extracted plasmids were stored in a -20°C refrigerator for further use.

2.2.7 Site-directed mutagenesis

PCR Quick Change is a reliable method for introducing point mutations into DNA. This technique allows for the alteration of a single nucleotide or multiple nucleotides (up to 5 bases) in the DNA sequence using specially designed primers. During DNA amplification, multiple point mutations can be incorporated into the primers, which are then used to introduce the mutations into the plasmid. Following PCR, DpnI enzyme was added to the reaction mixture and incubated at 37°C for 2 hours to remove the previous plasmid. The mixture was then transformed into *E. coli*, and after overnight culture, DNA extraction was performed to obtain the plasmids. These plasmids were subsequently sequenced by GATC Biotech (Constance, Germany) to confirm the presence of the desired mutations. For ligation of DNA fragments or DNA fragments with vectors, T4 DNA ligase (Fermentas, Thermo, Waltham, USA) was used. The ligation reaction was performed for 2 hours at room temperature, and the ratio of DNA fragment to vector was maintained at 5:1 to 10:1.

2.2.8 RNA transcription and preparation

In order to synthesize RNA via in vitro transcription, the first step involved linearizing the plasmid, which was then used as a template in a reaction with the AmpliCap-MaxT7 High Yield Message Maker Kit (Epicentre Biotechnologies) reagents to generate RNA. The T7 promoter was used to initiate transcription by T7 RNA polymerase. To linearize the plasmid, NheI enzyme was added to the plasmid-containing tube and incubated at 37°C for two hours. The concentration of the linearized plasmid was determined using a nano photometer (Nano PhotometerTM, Implen, Munic, Germany) and maintained at

approximately 200 ng. Table 2.11 was used as a reference for determining the appropriate ratio of reagents to be mixed for the AmpliCap-MaxT7 High Yield Message Maker Kit, which was then incubated at 37°C for 3 hours to achieve linearity.

After completion of the reaction, 20 µL of ammonium acetate was added to the tube, which was then stored in a refrigerator at -20°C for 2 hours to allow most of the RNA to precipitate completely. The mixture was then centrifuged at 30,000 rpm for 30 minutes at 4°C and the supernatant was removed. 50 µL of 70% ethanol was added to the tube, which was then washed and centrifuged for 1 minute before removing the supernatant. The excess ethanol was removed using a pipette and the tube was dried in a fume cupboard on ice. When the precipitate in the tube became transparent, 15 µL of RNase-free water was added to the tube and gently mixed several times using a pipette gun until the RNA pellet was completely dissolved. The concentration of RNA was determined using a nano photometer (Nano PhotometerTM, Implen, Munic, Germany). The RNA was stored at -20°C for further use.

Table 2.11 In-vitro transcription mix

Composition	Quantity
DNA template	5.4µL
T7 Enzyme Mix (5 U/µL)	2 µL
RNase Inhibitor (20 U/µL)	0.6 µL
10×T7 Transcription Buffer	2 µL
100 mM Dithiothreitol (DTT)	2 µL
AmpliCap-Max Cap/NTP PreMix	8 µL

2.3 *Xenopus laevis* oocyte

2.3.1 Oocyte preparation

Table 2.12 ND96 solution

Composition	Quantity
KCl	2 mM
NaCl	96 mM
$CaCl_2$	1 mM
$MgCl_2$	1 mM
Hepes	5 mM
Adjust pH to 7.5	

Xenopus laevis oocytes were dissected in accordance with approval #70/14 from the Landratsamt Würzburg Veterinaeramt. The dissected oocytes were subsequently washed thrice with ND96 solution, lacking calcium ions (Table 2.12). Thereafter, the oocytes were treated with 5 mg/mL collagenase for 1.5 hours, following which they were rinsed twice with ND96 solution containing $CaCl_2$ (1 mM) and Gentamycin (50 µg/mL). The washed oocytes were then transferred to a petri dish and kept at 16°C until further use.

2.3.2 RNA Microinjection into oocyte

To perform RNA injection, capillaries (3.511 Drummond #3-000-203-G/X; Drummond Scientific Company) were first filled with RNA, followed by injection into oocytes using a nano-injection machine (Nanoject; Drummond Scientific Company). Capillaries of the appropriate size were prepared using a vertical puller (PP83; Narishige) to ensure proper injection of RNA. The injected oocytes were then transferred to a Petri dish and maintained at 16°C, either with (for rhodopsin constructs) or without (for non-rhodopsin constructs) the addition of 10 μM ATR (all-trans retinal). The ND96 solution was regularly replenished to maintain optimal conditions for the oocytes. The animal study was conducted in accordance with the approved protocol #70/14 of the Landratsamt Würzburg Veterinaeramt.

2.3.3 Shrinking and swelling observation in oocyte

In this study, oocytes expressing different channels were incubated for two days after RNA injection. The oocytes were then placed in small Petri dishes containing different solutions and exposed to LED lights. Prolonged illumination time resulted in osmotic pressure differences, causing the oocytes to either swell or shrink. When the internal osmotic pressure was larger than the external pressure, water molecules entered the oocytes, leading to oocyte expansion. If the exposure time was too long, the oocytes could rupture. Conversely, when the internal osmotic pressure was lower than the external pressure, water molecules flowed out of the oocytes, causing them to shrink. The change in osmotic pressure was regulated by the salt concentration, which was controlled by using various optogenetic tools under long-term light exposure. Choosing appropriate solutions, optogenetic tools, and light types is crucial for successful oocyte swelling and shrinking experiments.

For efficient water transport, the *Xenopus* oocytes exhibited swelling or shrinking even after 20 minutes of continuous illumination. This process was limited to the flow of NaCl or KCl between the oocyte and the outside solution. The amount of NaCl flowing into the oocyte during swelling in ND96 buffer through XXM 2.0 and *Gt*ACR1 can be calculated by Faraday's laws:

$$n = It/(Fv)$$

(I: the constant current, 1 μA; t: the total time; F: Faraday constant, 9.6485×10^4 C/mol; v: the valency of the ions, 1). Then n is 6.22×10^{-10} mol per min. The volume for an oocyte can be calculated by the formula:

$$V = (4/3)\pi r^3$$

(r: the radius of an oocyte, 0.6 mm; π: 3.14).

Then V is 0.9 μL, assuming a constant inward current of 1 μA and a radius of 0.6 mm, the concentration of NaCl in the oocyte will increase by 0.691 mM/min. 20 min later, NaCl concentration in an oocyte could only increase 13.82 mM, determining the swelling efficiency.
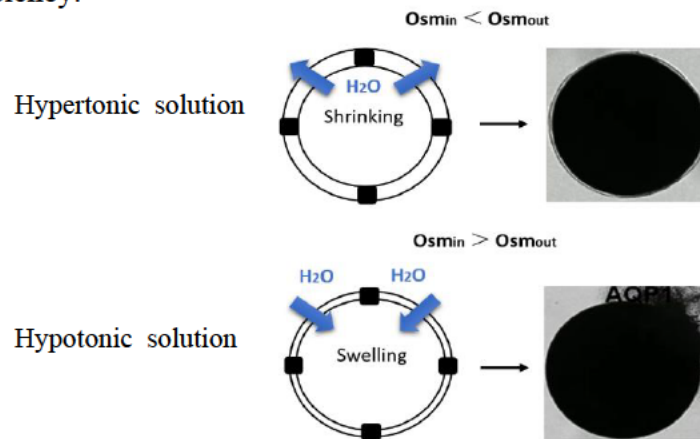

Fig 2.1 Morphological changes of *Xenopus* oocytes.

(a) *Xenopus* oocyte shrinks in the hypertonic solution. (b) *Xenopus* oocyte swells in the hypotonic solution.

Table 2.13 ND96 solution

Composition	Quantity
KCl	2 mM
NaCl	96 mM
$CaCl_2$	1 mM
$MgCl_2$	1 mM

28

Hepes	5 mM
Adjust pH to 7.6	

Table 2.14 High K$^+$ solution

Composition	Quantity
KCl	115 mM
CaCl$_2$	2 mM
MgCl$_2$	1 mM
Hepes	5 mM
Adjust pH to 7.6	

Table 2.15 High Na$^+$ solution

Composition	Quantity
NaCl	115 mM
CaCl$_2$	2 mM
MgCl$_2$	1 mM
Hepes	5 mM
Adjust pH to 7.6	

Table 2.16 Low Na$^+$/K$^+$ solution

Composition	Quantity
NMGCl	112.7 mM
KCl	1.15 mM
NaCl	1.15 mM
CaCl$_2$	2 mM
MgCl$_2$	1 mM
Hepes	5 mM
Adjust pH to 7.6	

2.4 Electrophysiology

Voltage clamps are an essential tool used to measure electrophysiological activity in *Xenopus* oocytes. The origin of the voltage clamp dates back to the pioneering experiments of George Marmont and Kenneth Cole in 1947. Through their experiments on squid, they discovered that the membrane potential of cell membranes could be maintained at a constant value using double electrodes and a feedback circuit [128-129]. Voltage clamps are widely used to measure ionic currents across excitable cell

membranes [130]. To obtain different currents, the experimenter can set different voltage values, allowing researchers to study the mechanism of ion channels, which are abundant in the excitable cell membrane [130-131]. Voltage clamps can be classified into two-electrode voltage clamps and single-electrode voltage clamps. Two-electrode voltage clamps (TEVCs) are frequently used to study membrane proteins, particularly ion channels [132]. It is common practice for researchers to express membrane proteins in *Xenopus* oocytes for research purposes [133]. On the other hand, single voltage clamps are typically used for patch clamp studies.

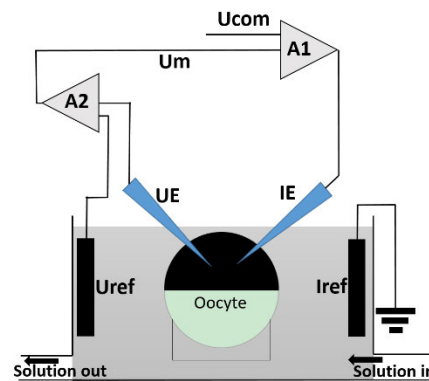### 2.4.1 Two electrode voltage-clamp (TEVC)

Fig 2.2 Two electrode voltage-clamp (TEVC) with *Xenopus* Oocytes.
The dark side of the *Xenopus* Oocyte was injected with a voltage electrode (UE) and a current electrode (IE), respectively. UE: potential electrode, IE: current electrode, Uref: potential reference electrodes, Iref: current reference electrodes, Um is the membrane potential of the oocyte. Ucom is the control potential input by the from the computer program. A1 and A2 are the potential amplifier and the feedback amplifier, respectively.

Xenopus oocytes are widely used for heterologous protein expression, owing to their large size, high efficiency, and good stability. Optogenetic proteins are frequently expressed on *Xenopus* oocytes, and their current on the oocyte membrane can be easily measured using a two-electrode voltage-clamp. The voltage-clamp system comprises a current electrode and a potentiometric electrode. Reference electrodes for current (Iref) and potential (Uref) are immersed in the solution, as shown in Figure 2.2. To measure the current, the *Xenopus* oocyte is placed in a small groove, and the current and potential electrodes are inserted into the oocyte. The membrane potential of the *Xenopus* oocyte (Um) is calculated as the difference between UE and Uref. Ucom is the voltage value set by the computer program. The different solutions flow and exchange through

channels at the bottom of the tank. The solution flow rate should be moderate; if it is too fast, it will easily penetrate the *Xenopus* oocyte and cause noise. Conversely, if the speed is too slow, it will take too long to replace the solution, and the condition of the *Xenopus* oocyte will be affected if it remains in the solution for an extended duration. The two electrode clamp system used in this study was TURBO TEC-03X, manufactured by npi electronic GmbH (Tamm, Germany).

2.4.2 Solutions used for oocytes electrophysiology

Table 2.17 High Na$^+$ solution

Composition	Quantity
NaCl	115 mM
CaCl$_2$	2 mM
MgCl$_2$	1 mM
Hepes	5 mM
Adjust pH to 7.6	

Table 2.18 High K$^+$ solution

Composition	Quantity
KCl	115 mM
CaCl$_2$	2 mM
MgCl$_2$	1 mM
Hepes	5 mM
Adjust pH to 7.6	

Table 2.19 Low Na$^+$/K$^+$ solution

Composition	Quantity
NMGCl	112.7 mM
KCl	1.15 mM
NaCl	1.15 mM
CaCl$_2$	2 mM
MgCl$_2$	1 mM
Hepes	5 mM
Adjust pH to 7.6	

Table 2.20 High NMG$^+$ solution

Composition	Quantity
NMGCl	115 mM
CaCl$_2$	2 mM
MgCl$_2$	1 mM
Hepes	5 mM
Adjust pH to 7.6	

Table 2.21 High Cs$^+$ solution

Composition	Quantity
CsCl	115 mM
CaCl$_2$	2 mM
MgCl$_2$	1 mM
Hepes	5 mM
Adjust pH to 7.6	

Table 2.22 High CH$_3$NH$_3^+$ solution

Composition	Quantity
CH$_3$NH$_3$Cl	115 mM
CaCl$_2$	2 mM
MgCl$_2$	1 mM
Hepes	5 mM
Adjust pH to 7.6	

Table 2.23 High Gdm$^+$ solution

Composition	Quantity
GdmCl	115 mM
CaCl$_2$	2 mM
MgCl$_2$	1 mM
Hepes	5 mM
Adjust pH to 7.6	

Table 2.24 High Li$^+$ solution

Composition	Quantity
LiCl	115 mM
CaCl$_2$	2 mM

MgCl$_2$	1 mM
Hepes	5 mM
Adjust pH to 7.6	

Table 2.25 High Ca^{2+} solution

Composition	Quantity
CaCl$_2$	80 mM
CaCl$_2$	2 mM
MgCl$_2$	1 mM
Hepes	5 mM
Adjust pH to 7.6	

Table 2.26 High Mg^{2+} solution

Composition	Quantity
MgCl$_2$	80 mM
CaCl$_2$	2 mM
MgCl$_2$	1 mM
Hepes	5 mM
Adjust pH to 7.6	

Table 2.27 High Ba^{2+} solution

Composition	Quantity
BaCl$_2$	80mM
CaCl$_2$	2 mM
MgCl$_2$	1 mM
Hepes	5 mM
Adjust pH to 7.6	

2.4.3 Electrodes and capillaries for TEVC

A 1.5 mm diameter electrode capillary with a wall thickness of 0.178 mm (Hilgenberg) was loaded with 3 M KCl solution after assembling the equipment, resulting in an electrode tip resistance of 0.4-1 MΩ. The current and voltage electrodes were connected to capillaries filled with 3 M KCl solution on either side. An AD-DA converter (Digidata 1322A, Axon Instruments) was used to control the stimulation and data acquisition. Various laser light sources were employed to activate the channels on the *Xenopus* oocytes.

2.4.4 Program for TEVC and data analysis

WinEDR (University of Strathclyde) and WinWCP (University of Strathclyde) were used to record the current and voltage of the optogenetic tools. Finally, Clampfit 9.0 (Axon Instruments) was used for data analysis and processing of the recorded current and voltage data.

2.4.5 Light source

This experiment utilized green (532 nm) laser as light sources to activate optogenetic channels on oocytes. Illumination was performed by the mounted 520 nm green LEDs (WINGER WEPGN3-S1 Power LED Star grün 520nm, 3W - 120lm) above the Petri dishes. The lasers were provided by Changchun New Industry Optoelectronics Technology Company. To characterize the action spectrum of the optogenetic tool, we used narrow-band interference filters (Edmund Optics) and a high-power white light generator, the PhotoFluor II light source (89North), in addition to lasers with constant wavelength. The PhotoFluor II light source provides a wavelength range of 420 nm to 620 nm (422 nm, 439 nm, 459 nm, 481 nm, 496 nm, 516 nm, 540 nm, 562 nm, 595 nm, 620 nm). LEDs with various wavelengths were also employed, with a wider range of wavelengths, and the value of the wavelength was confirmed using a spectrometer (Ocean Optics). It is crucial to maintain the same number of photons for each wavelength during spectroscopic experiments. For photosensitivity experiments, different light levels were required, and these were measured using a Laser Check photometer (Coherent Technologies). To test the recovery cycle characteristics of optogenetic tools, light frequencies from 1 to 15 Hz were set using WinWCP (University of Strathclyde). The relationship between illumination duration and peak current was investigated by setting different illumination durations (1ms, 2ms, 5ms, 10ms, 20ms, 50ms, 75ms, and 100ms) using WinWCP (University of Strathclyde).

2.5 Plasmids and RNA Generation for *Xenopus Laevis* Oocyte Expression

The optogenetic tools, namely NCR1 2.0, KCR1 2.0, *Gt*ACR1, and aquaporins (AQP1), were synthesized in accordance with the published amino acid sequences using GeneArt Strings DNA Fragments (Life Technologies, Thermo Fisher Scientific) as previously described. The fragments were inserted into the pGEM vector and cloned. After linearization of the cloned pGEM plasmids by means of digestion (NheI), the

AmpliCap-MaxT7 High Yield Message Maker Kit (Epicentre Biotechnologies) was used for cRNA preparation in a 37°C incubator for 3 hours.

Lucy-Rho (LR) signal peptide, consisting of seventeen N-terminal amino acids from leucine-rich repeat 32 proteins and nineteen N-terminal amino acids from a rhodopsin tag, was shown to significantly promote its plasma membrane targeting in mammalian cells [134]. To enhance expression and plasma membrane targeting, the plasma membrane trafficking signal (T) and a 3'-ER export signal (E) derived from Kir2.1 [89] were fused to the C-terminal of NCR1 and KCR1. Additionally, eYFP was inserted between T and E as an expression marker to semi-quantitatively measure opsin expression levels. The TYE motif, which contains a trafficking signal, an enhanced yellow fluorescent protein, and an endoplasmic reticulum export signal at its C-terminal, respectively [89]. Specifically, NCR1 and KCR1 were fused only with eYFP fragments, while NCR1 2.0, XXM 2.0, and KCR1 2.0 were fused not only with eYFP fragments, but also with LR (enhance expression signal peptide), T (trafficking signal peptide), and E (export signal peptide).

Full-length NCR1 2.0 contains 432 amino acids. To compare NCR1's properties with different lengths, the C-terminal amino acid of NCR1 was truncated by 102 and 149 amino acids, resulting in NCR1 2.0 (330) and NCR1 2.0 (283), with lengths of 330 and 283 amino acids, respectively. In addition, the N-terminal amino acid of NCR1 2.0 was truncated by 10 amino acids and the C-terminal amino acid was truncated by 149 amino acids, resulting in only 273 amino acids being retained in NCR1 2.0 (273). To assess their functional properties, various types of cRNAs, including NCR1, NCR1 2.0, KCR1, KCR1 2.0, *Gt*ACR1, and AQP1, were injected into *Xenopus* oocytes using NanojectIII (Drummond Scientific Company) as single or mixed cRNAs. The oocytes were then incubated in ND96 buffer (96 mM NaCl, 2 mM KCl, 1 mM CaCl$_2$, 1 mM MgCl$_2$, 5 mM Hepes, pH=7.6) containing 1 µM total trans-retinal at 16°C for two days prior to use. All the constructs were verified through commercially available DNA sequencing (Eurofins Genomics Germany GmbH).

2.6 Confocal Images Processing

The laser confocal microscope (Leica SP5, Leica Microsystems CMS, Mannheim, Germany) was utilized to capture fluorescence images of oocytes and observe morphological changes in the oocytes. To determine whether the different channels

were expressed successfully in the oocytes, the oocytes were placed in ND96 in a 35 x 10 mm petri dish (Greiner GBO) for imaging. The fluorescence emission of eYFP was captured between 520 and 580 nm upon excitation by a 496 nm laser. The images were obtained using the laser confocal microscope. Both the experimental and control groups were conducted under the same set of experimental conditions.

2.7 Data Analysis

The fluorescence images obtained from the oocytes were analyzed using ImageJ software. GraphPad 7.0.4 was used to generate the current statistics and oocyte efficiency images. The current images of the different channels were created using Origin 2021 software. The kinetics of NCR1 2.0 (273) in oocytes were analyzed using Clampfit 10.7 software. The results of the experiments were presented as mean ± standard error of the mean (SEM) using GraphPad Prism software.

3 Results

3.1 Discovery of NCR1

3.1.1 Expression and optimization of NCR1
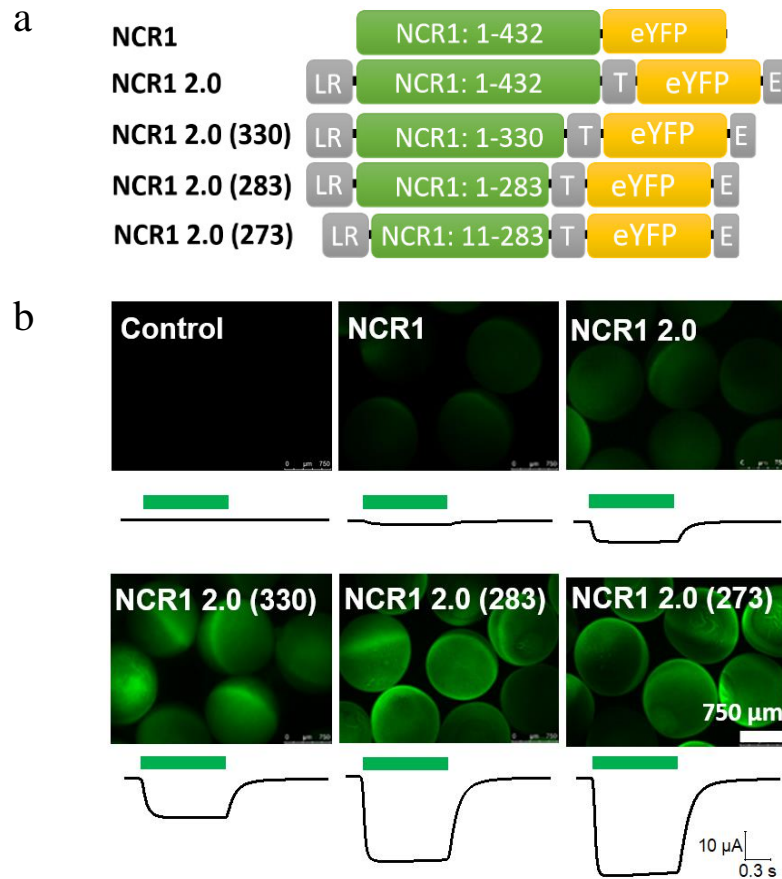
Fig 3.1 Expression and photocurrent of NCR1.

(a) Different truncated constructs of NCR1. LR: the Lucy-Rho membrane targeting signal, T: plasma membrane trafficking signal, E: ER export signal peptides, eYFP: yellow fluorescent protein. Please note that NCR1 2.0(273) had a further 10 aa truncation at the N terminal，while all other NCR1.2 variants were truncated at the C-terminus. (b) Fluorescence pictures and photocurrents of different NCR1 variants. 30 ng cRNA was injected into the *Xenopus* oocyte for each construct. Fluorescence images of NCR1 were taken two days post injection. Photocurrent was measured with extracellular ORi Ca^{2+} solution (110 mM NaCl, 5 mM KCl, 2 mM $CaCl_2$, 1 mM $MgCl_2$, 5 mM HEPES and pH=7.6). The green bar indicated the 0.5 s green light illumination, 532 nm at 0.5 mW/mm². Holding potential: -40 mV.

The above picture shows the plasmids with different structures (Fig 3.1a). The eYFP is fused to the C-terminal of NCR1. To enhance the expression of NCR1 in the plasma membrane, optimized NCR1 2.0 constructs were designed by fusing the LR signal peptide to the N-terminal of NCR1, in addition to the plasma membrane trafficking

signal (T) and ER export signal peptides (E) in the C-terminal. Full-length NCR1 2.0 contains 432 amino acids. To verify whether the number of amino acids affects the properties of NCR1 2.0. NCR1 2.0 (330), NCR1 2.0 (283), and NCR1 2.0 (273) were constructed, retaining the number of amino acids as 330, 280, and 273, respectively. NCR1 2.0 (330) and NCR1 2.0 (283) were generated through C-terminal amino acid sequence cleavage, whereas NCR1 2.0 (273) was produced by N-terminal cleavage of the amino acid sequence. Specifically, 10 amino acids were removed from the N-terminal of NCR1 2.0 (283). The control group did not exhibit any fluorescence, as shown in Figure 3.1b. NCR1 displayed weak fluorescence, while the fluorescence intensity and current of NCR1 2.0 were stronger than that of NCR1, indicating that LR and TYE increased the expression of NCR1 on the plasma membrane of oocytes. The fluorescence intensity of NCR1 2.0 was similar among different amino acid lengths within the NCR1 2.0 groups, but the current increased as the number of amino acids of NCR1 decreased. The shorter length of NCR1 2.0 displayed larger currents. NCR1 2.0 (273) showed the maximum current, and as the number of amino acids decreased, the current in NCR1 2.0 increased. The current in NCR1 2.0 (273) was most abundantly expressed and showed the largest photocurrent under light.

3.1.2 Light sensitivity of NCR1 variants
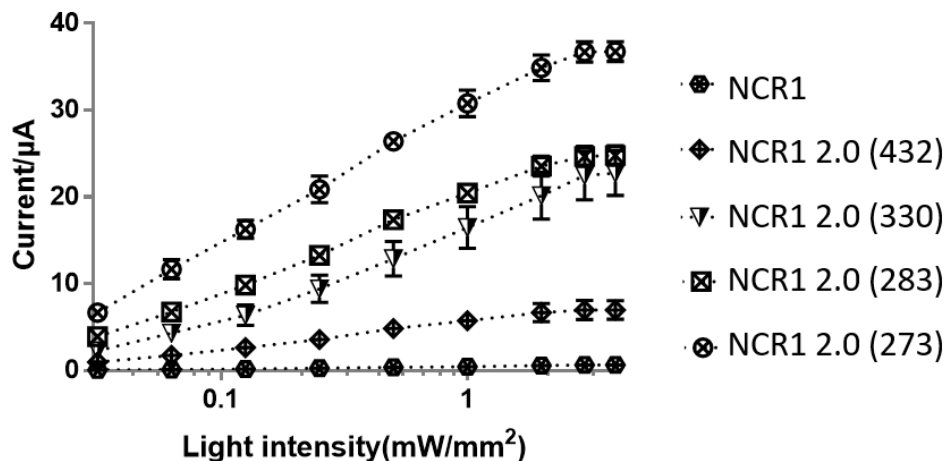
Fig 3.2 Light sensitivity of NCR1 variants.
Light sensitivity of different NCR1 variants under different 532 nm light intensities ranging from 0.03 to 4 mW/mm² (0.031, 0.062, 0.125, 0.125, 0.25, 0.5, 1, 2, 3, 4 mW/mm²). 30 ng cRNA was injected into the *Xenopus* oocyte for each construct. Photocurrent was measured with extracellular ORi Ca^{2+} solution (110 mM NaCl, 5 mM KCl, 2 mM CaCl$_2$, 1 mM MgCl$_2$, 5 mM HEPES and pH=7.6) at 2 dpi. Holding potential: -40 mV.

As the intensity of green light increases from 0.03 to 2 mW/mm², the current of NCR1 exhibits a rapid rise, but the rate of increase slows down when the light intensity is between 2 and 3 mW/mm² (Fig 3.2). The current of NCR1 2.0 reaches a saturation level at around 3 mW/mm² of light intensity. Further, the current remains constant as the light intensity increases from 3 to 4 mW/mm². In comparison to the original NCR1, the photocurrent of NCR1 2.0 (273) was improved ~58 folds.

3.1.3 The action spectrum of NCR1 2.0
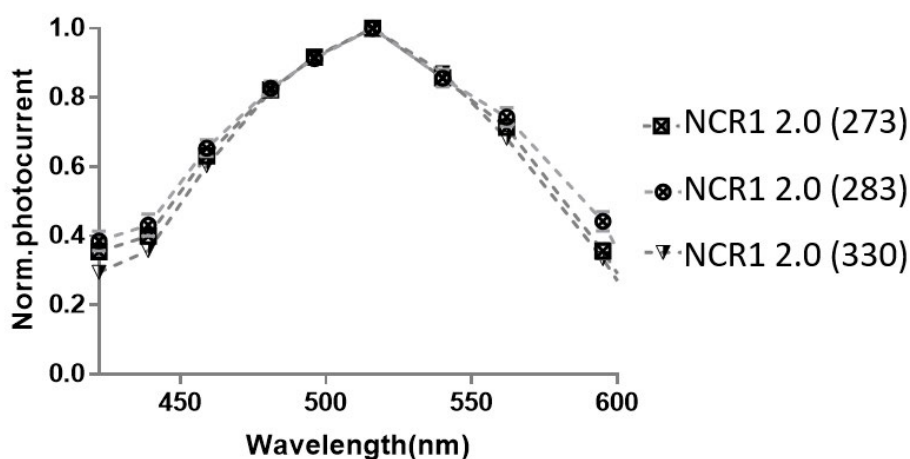
Fig 3.3 The action spectrum of NCR1 2.0.

The action spectrum of NCR1 2.0. The wavelength was changed from 420 nm to 620 nm. The number of photons is the same for each wavelength. NCR1 2.0 has the largest current when the wavelength is around 520 nm. 30 ng cRNA was injected into the oocyte for each construct. Photocurrent was measured with extracellular ORi Ca^{2+} solution (110 mM NaCl, 5 mM KCl, 2 mM $CaCl_2$, 1 mM $MgCl_2$, 5 mM HEPES and pH=7.6) at 2 dpi. Holding potential: -40 mV. n = 6, error bars = SEM.

We further compared the action spectra of the three best-expressed NCR1 variants. All of them showed activation peaks at around 520 nm. The recorded current displayed a gradual increase followed by a decrease as the wavelength was varied from 420 nm to 620 nm in all groups (Fig 3.3). The NCR1 2.0 (273) exhibits the largest current amplitude among all groups. The spectral characteristics of NCR1 2.0 (273), NCR1 2.0 (283), and NCR1 2.0 (330) are similar. The experimental results demonstrate that by decreasing the amino acid sequence length of NCR1 2.0, its current amplitude increases while maintaining the same spectral and photosensitive properties.

3.1.4 Mutation of NCR1 2.0

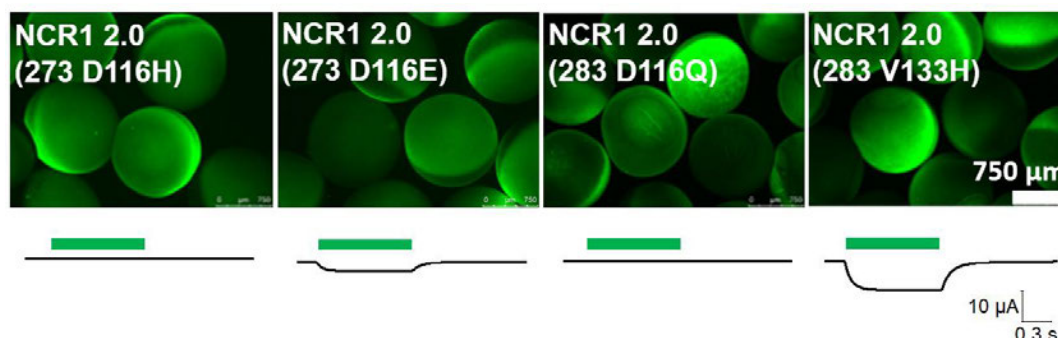### 3.1.4.1 Expression and photocurrent of NCR1 2.0 mutants

Fig 3.4 Expression and photocurrent of NCR1 2.0 mutants.

Fluorescence pictures and photocurrents of different NCR1 2.0 mutants. 30 ng cRNA was injected into the *Xenopus* oocyte for each construct. Fluorescence images of NCR1 2.0 were taken two days post injection. Photocurrent was measured with extracellular ORi Ca^{2+} solution (110 mM NaCl, 5 mM KCl, 2 mM $CaCl_2$, 1 mM $MgCl_2$, 5 mM HEPES and pH=7.6) at 2 dpi. The green bar indicated the 0.5 s green light illumination, 532 nm at 0.5 mW/mm². Holding potential: -40 mV.

The choice of specific amino acid positions for mutation was based on the fact that XXM 2.0 exhibited point mutations at the same positions, resulting in increased current and greater selectivity for Na^+ after mutation. Therefore, we targeted these positions for point mutations of NCR1 2.0 in order to enhance the current and Na^+ selectivity. Successful expression of the four mutants was confirmed by observing fluorescence in oocytes (Fig 3.4), with comparable fluorescence intensities and no significant differences among the four mutants. Notably, NCR1 2.0 (273 D116E) and NCR1 2.0 (283 V133H) showed significant currents in the ORi Ca^{2+} solution, while NCR1 2.0 (273 D116H) and NCR1 2.0 (283 D116Q) showed no obvious currents. This highlights the crucial role of amino acid position 116 in the NCR1 2.0 sequence, and suggests that altering the amino acid type at this position can significantly impact its function.

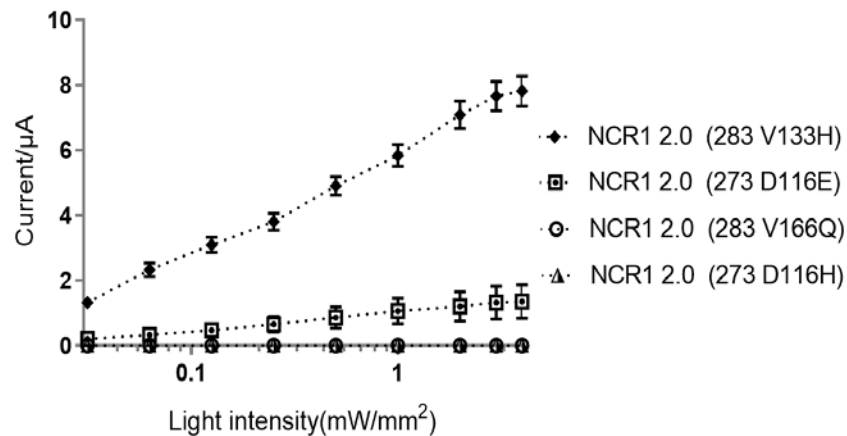### 3.1.4.2 Light sensitivity of NCR1 2.0 mutants

Fig 3.5 Light sensitivity of NCR1 2.0 mutants.

Light sensitivity of different NCR1 2.0 mutants under different 532 nm light intensities ranging from 0.03 to 4 mW/mm² (0.031, 0.062, 0.125, 0.125, 0.25, 0.5, 1, 2, 3, 4 mW/mm²). 30 ng cRNA was injected into the *Xenopus* oocyte for each construct. The NCR1 2.0 (273 D116H) and NCR1 2.0 (283 V166Q) groups displayed negligible photocurrents. Photocurrent was measured with extracellular ORi Ca^{2+} solution (110 mM NaCl, 5 mM KCl, 2 mM CaCl$_2$, 1 mM MgCl$_2$, 5 mM HEPES and pH=7.6) at 2 dpi. Holding potential: -40 mV.

The photocurrents exhibited a steady increase with increasing light intensity ranging from 0.03 to 4 mW/mm² in NCR1 2.0 (283 V133H) and NCR1 2.0 (273 D116E) groups. Conversely, no significant current was detected in the NCR1 2.0 (273 D116H) and NCR1 2.0 (283 D116Q) groups. (Fig 3.5).

3.1.4.3 The action spectrum of NCR1 2.0 mutants
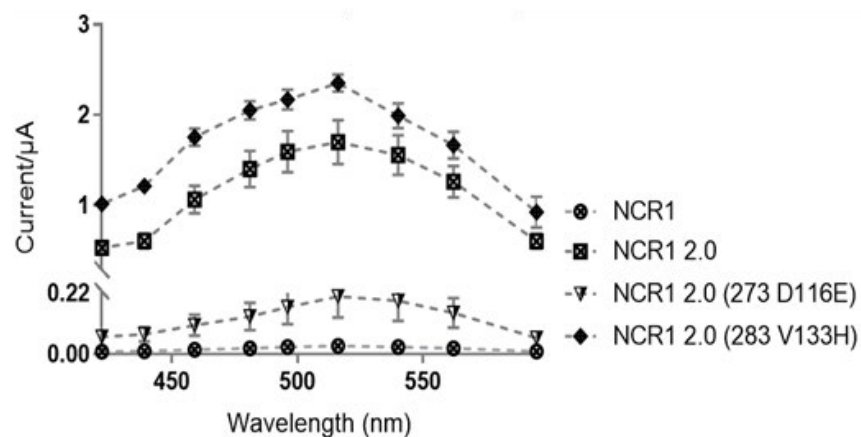
Fig 3.6 The action spectrum of NCR1 2.0 mutants.

The action action spectrum of NCR1 2.0 mutants. The wavelength lengths were changed from 420 nm to 620 nm. The number of photons is the same for each wavelength. NCR1 2.0 has the largest current when the wavelength around 520 nm. 30 ng cRNA was injected into the *Xenopus* oocyte for

each construct. Photocurrent was measured with extracellular ORi Ca^{2+} solution (110 mM NaCl, 5 mM KCl, 2 mM $CaCl_2$, 1 mM $MgCl_2$, 5 mM HEPES and pH=7.6) at 2 dpi. Holding potential: -40 mV. n = 6, error bars = SEM.

The recorded current displayed a gradual increase followed by a decrease as the wavelength was varied from 420 nm to 620 nm in all groups, including NCR1, NCR1 2.0, and the mutant groups (Fig 3.6). Notably, NCR1, NCR1 2.0, NCR1 2.0 (283 V133H), and NCR1 2.0 (273 D116E) demonstrated a maximum current response around 520 nm. These findings suggest that NCR1 2.0 exhibits larger currents at wavelengths around 520 nm compared to other wavelengths.

3.1.5 The current and reversal potential of NCR1 in Na^+ and K^+ solutions

To compare the relevant Na^+ and K^+ conductance, the reversal potentials of different NCR1 variants were measured in three different solutions containing either high Na^+, high K^+ or low Na^+/K^+ concentrations. As the length of NCR1 amino acid sequence decreased, the current generated by NCR1 2.0 gradually increased in high Na^+, high K^+, and low Na^+/ K^+ solutions. In particular, the current of NCR1 2.0 (273) was significantly larger than that of NCR1 2.0 (283) and NCR1 2.0 (330) in all these solutions, suggesting that shorter NCR1 2.0 sequences are associated with larger currents (Fig 3.7a/b). Interestingly, we found similar reversal potentials in different NCR1 variants, indicating that ion selectivity was not influenced by the modifications and truncations (Fig 3.7c).
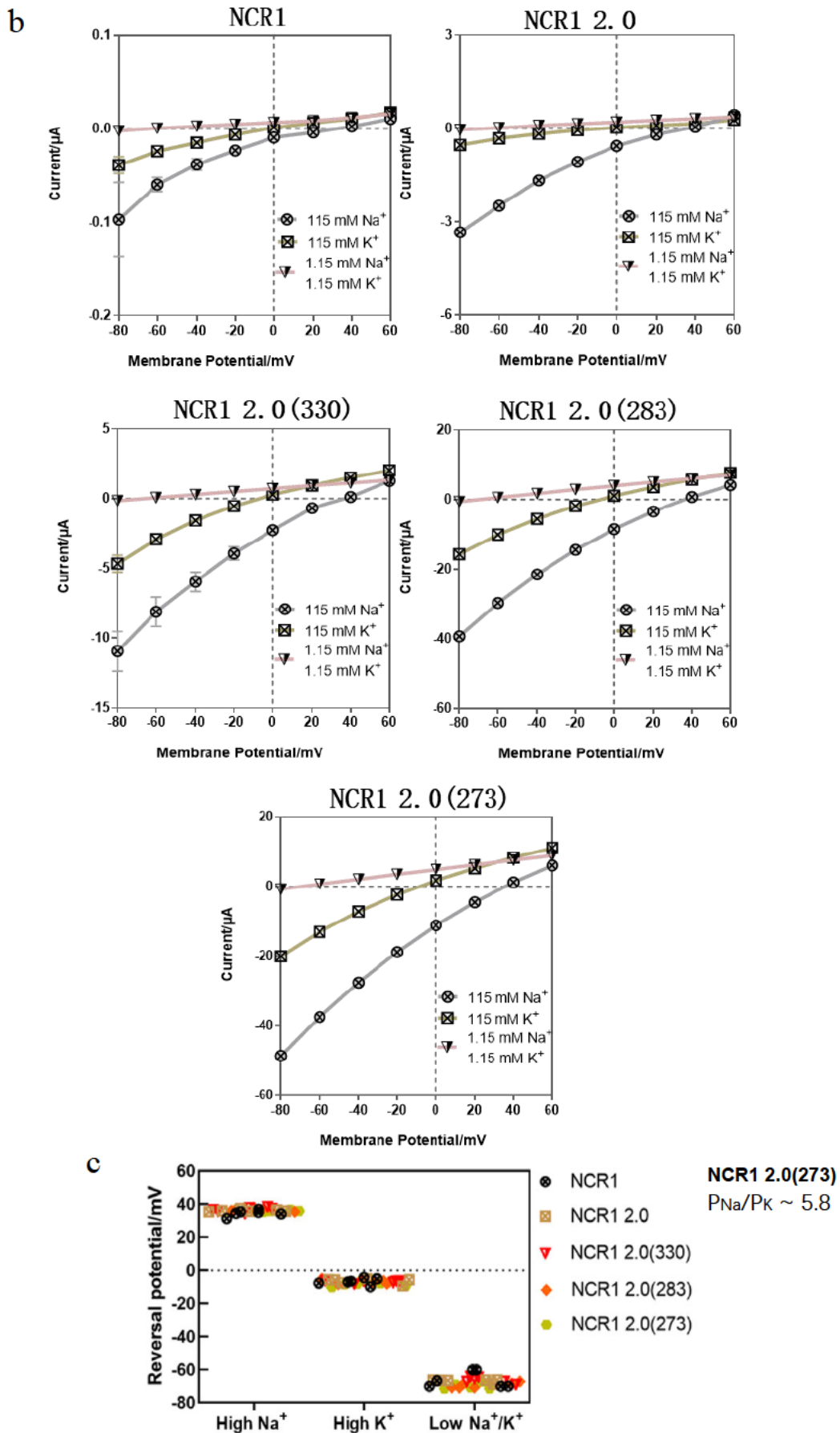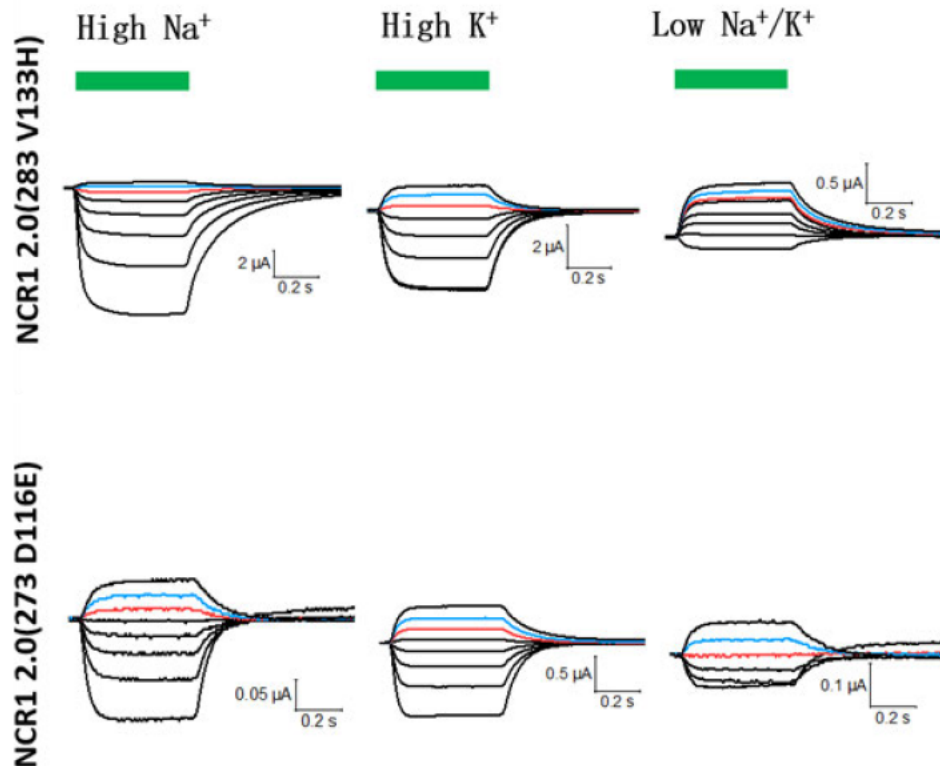
a
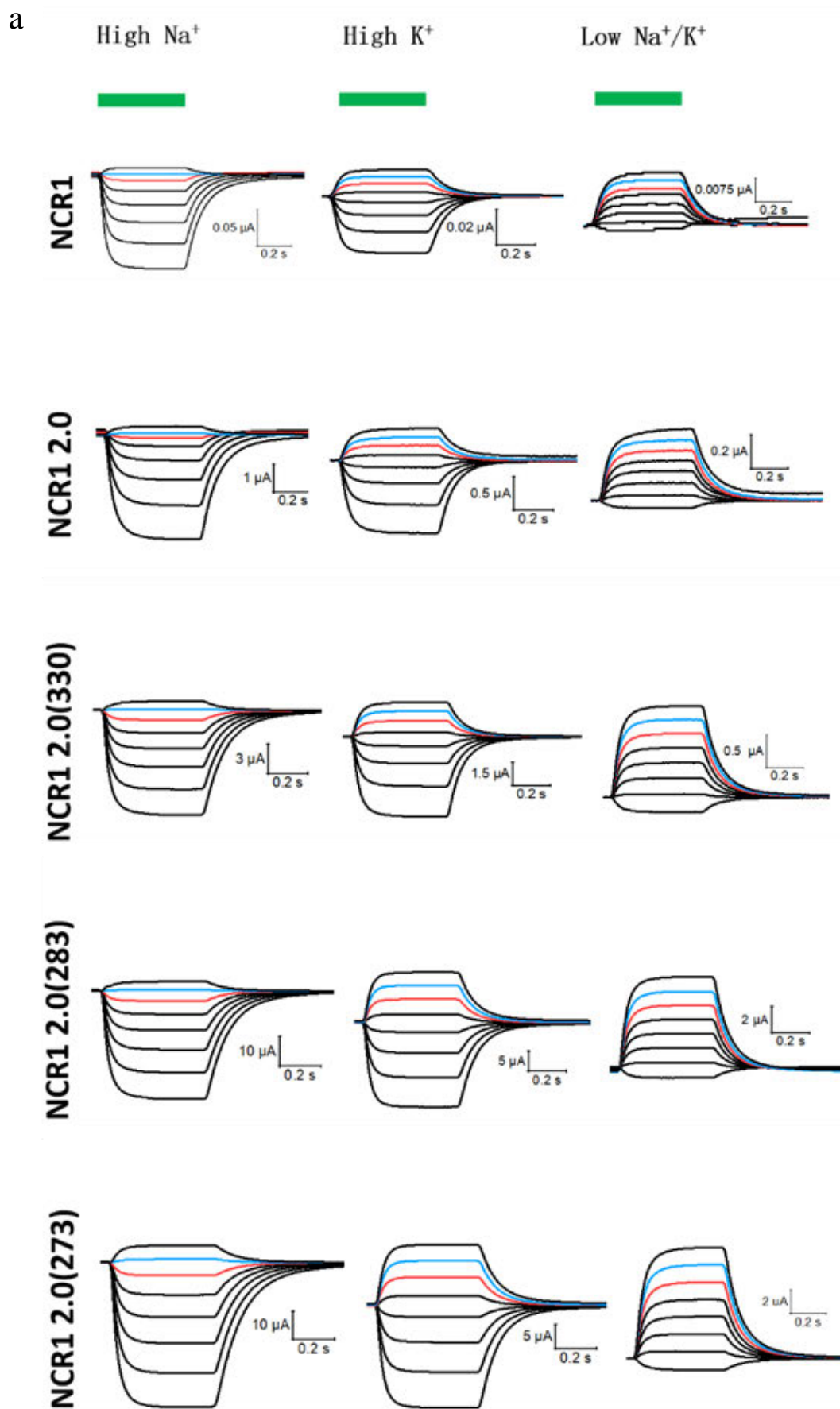
Fig 3.7 The current and reversal potential of NCR1 in Na⁺ and K⁺ solutions.

(a/b) Representative photocurrent traces and current-potential curves of NCR1 in high Na^+, high K^+ and low Na^+/K^+. Photocurrents were measured with oocytes at 2 dpi upon 0.5 s green light (532 nm, 0.5 mW/mm²) illumination, indicated by the green bars. Holding potentials were changed from -80 mV to +60 mV. For the current-potential curves, n = 6 experiments. (c) The calculated reversal potentials of different NCR1s in high Na^+, high K^+ and low Na^+/K^+ solution. The calculated P_{Na}/P_K of NCR1 2.0 (273) was shown on the right, n = 6.

In high Na^+ solution, the NCR1 2.0 (273) showed the most pronounced photocurrent and the reversal potential was calculated to be around +36 mV, while in the high K^+ solution its photocurrent was smaller and the reversal potential was around -9 mV. In the solution with low Na^+/K^+, the photocurrent became much smaller, the reversal potential was determined around -70 mV, which also indicated low proton current. The P_{Na}/P_K permeability ratio of NCR1 2.0 (273) was calculated to be ~ 5.8.

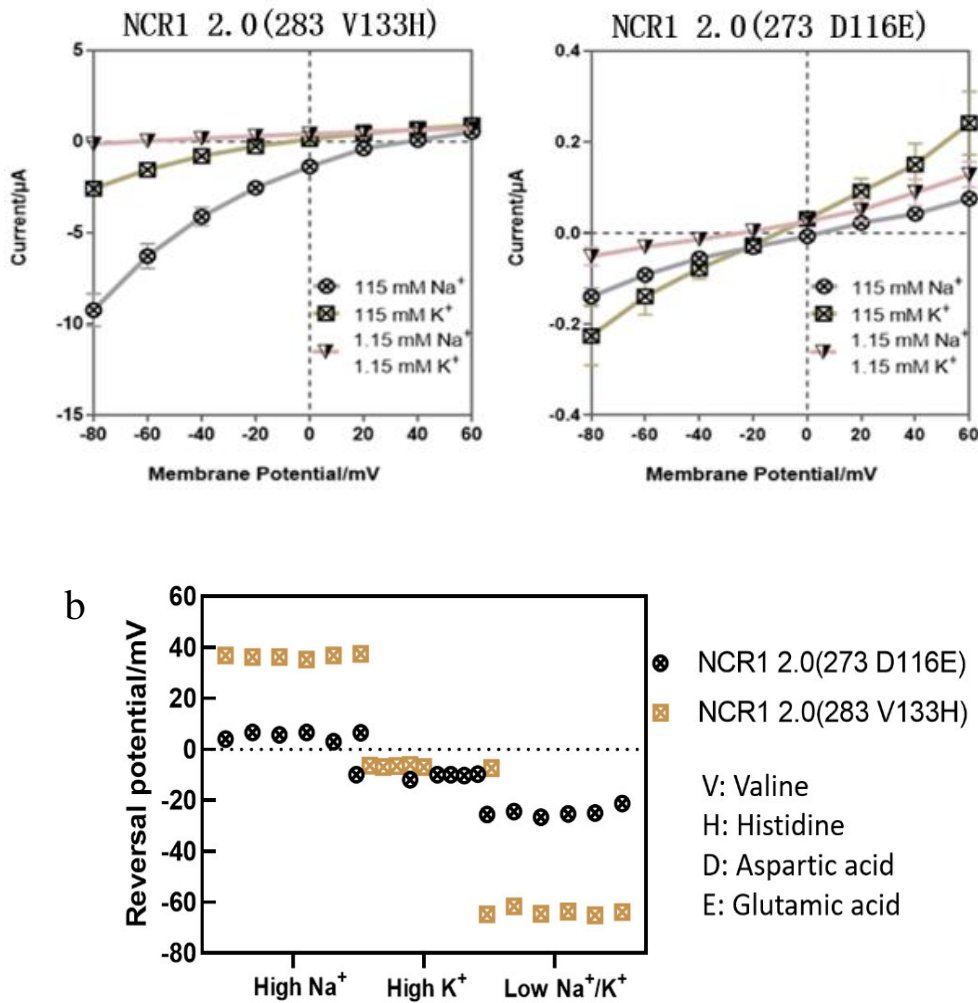## 3.1.6 The current and reversal potential of NCR1 2.0 mutants in Na^+ and K^+ solutions

a

**Fig 3.8 The current and reversal potential of NCR1 2.0 mutants in Na$^+$ and K$^+$ solutions**

(a) Representative photocurrent traces and current-potential curves of NCR1 2.0 mutants in high Na$^+$, high K$^+$ and low Na$^+$/K$^+$ solutions. Photocurrents were measured with oocytes at 2 dpi upon 0.5 s green light (532 nm, 0.5 mW/mm²) illumination, indicated by the green bars. Holding potentials were changed from -80 mV to +60 mV. For the current-potential curves, n = 6 experiments. (b) The reversal potentials of different NCR1 2.0 mutants in high Na$^+$, high K$^+$ and low Na$^+$/K$^+$ solution. For the current-potential curves, n = 6 experiments.

The current of the two NCR1 mutants, NCR1 2.0 (273 D116E) and NCR1 2.0 (283 V133H), are presented in Figure 3.8a. The mutants generated currents in high Na$^+$, high K$^+$ and low Na$^+$/K$^+$ solutions, indicating that they remained functional after the mutations. The reversal potential of the NCR1 2.0 mutants varied in different solutions. Specifically, the reversal potential of NCR1 2.0 (273 D116E) ranged between 0 mV and 20 mV in high Na$^+$ solution, while it ranged between -20 mV and -40 mV in low Na$^+$/K$^+$ solution.

In comparison, the current of NCR1 2.0 (283 V133H) was larger than that of NCR1 2.0 (273 D116E) in in high Na$^+$, high K$^+$, and low Na$^+$/K$^+$ solutions. Furthermore, the reversal potential of NCR1 2.0 (283 V133H) was the same as that of NCR1 2.0 (273) in high Na$^+$, high K$^+$, and low Na$^+$/K$^+$ solutions, as revealed by the statistical charts of the reversal potentials of the mutants (Fig 3.8b). The reversal potentials of NCR1 2.0 (273 D116E) and NCR1 2.0 (283 V133H) were the same in high K$^+$ solution. However, in high Na$^+$ solutions, the reversal potential of NCR1 2.0 (283 V133H) was larger than that of NCR1 2.0 (273 D116E). In low Na$^+$/K$^+$ solution, the reversal potential of NCR1 2.0 (283 V133H) was lower than that of NCR1 2.0 (273 D116E). Despite significant reversal potential changes of NCR1 2.0 (273 D116E) in both high Na$^+$ and low Na$^+$/K$^+$ solutions, the current was much smaller than that of NCR1 2.0 (273), which limits the practical use of NCR1 2.0 (273 D116E).
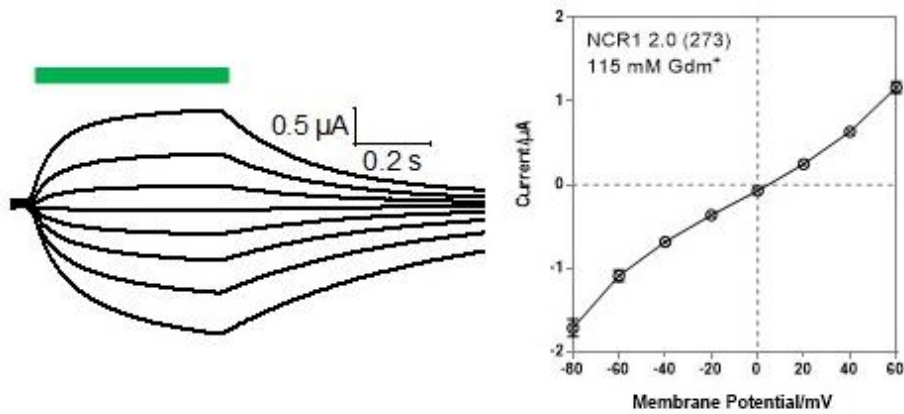
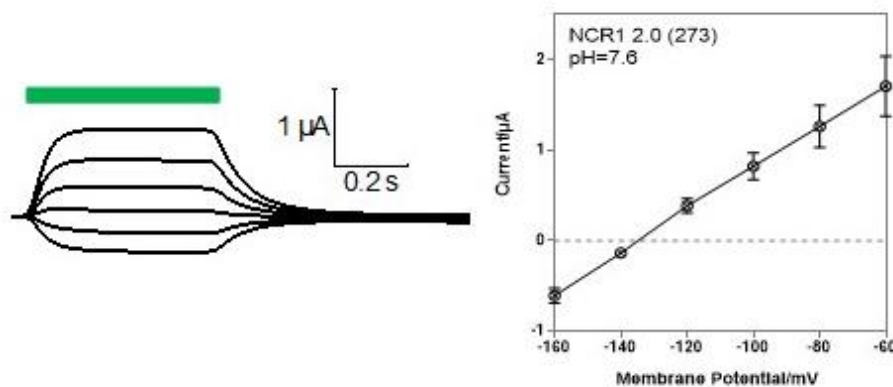### 3.1.7 The ion selectivity of NCR1 2.0
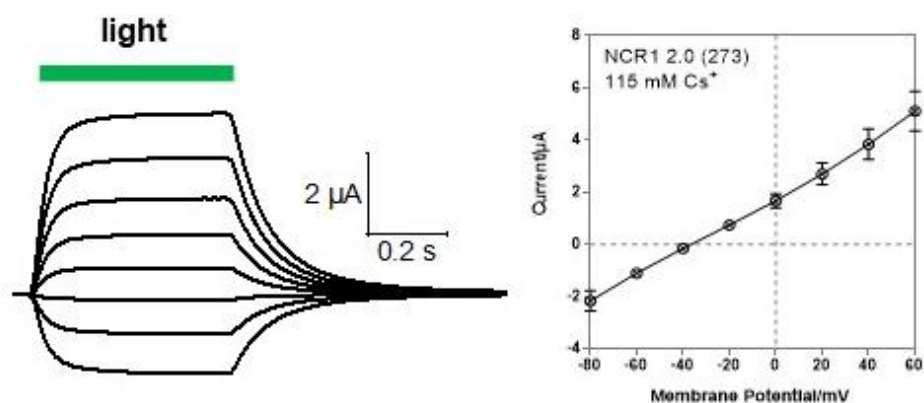
Solution: 115 mM CsCl, 2 mM CaCl$_2$, 1 mM MgCl$_2$, 5 mM Hepes, pH =7.6
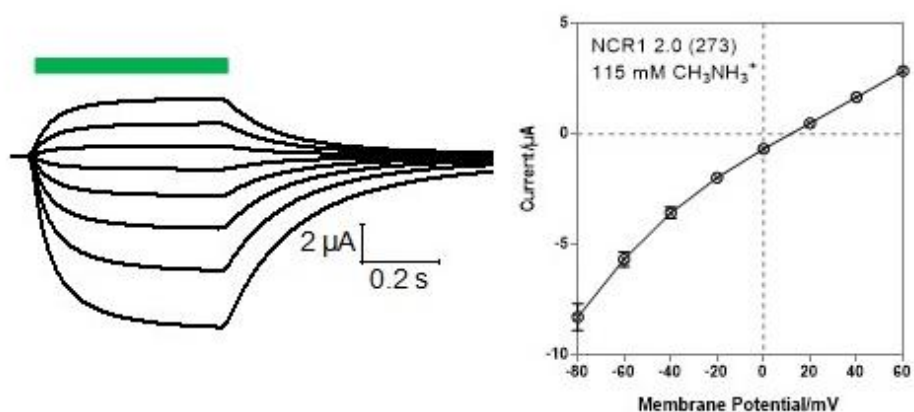
Solution: 115 mM CH$_3$NH$_3$Cl, 2 mM CaCl$_2$, 1 mM MgCl$_2$, 5 mM Hepes, pH =7.6

Solution: 115 mM GdmCl, 2 mM CaCl₂, 1 mM MgCl₂, 5 mM Hepes, pH =7.6

Solution: 115 mM NMGCl, 2 mM CaCl₂, 1 mM MgCl₂, 5 mM Hepes, pH =7.6

Fig 3.9a Analysis of relative permeabilities of NCR1 2.0 for high monovalent solutions.
Representative photocurrent traces and current-potential curves of NCR1 2.0 in different solutions.
Photocurrents were measured with oocytes at 2 dpi upon 0.5 s green light (532 nm, 0.5 mW/mm²)
illumination, indicated by the green bars. Different holding potentials were used. For the current-
potential curves, n = 6 experiments, error bars = SEM.

NCR1 2.0 exhibits inward current in the aforementioned solutions under illumination,
indicating its permeability to Cs^+, $CH_3NH_3^+$, Gdm^+, and H^+.

Solution: 80 mM CaCl₂, 2 mM MgCl₂, 5 mM Hepes, pH =7.6

Solution: 80 mM MgCl₂, 2 mM CaCl₂, 5 mM Hepes, pH =7.6

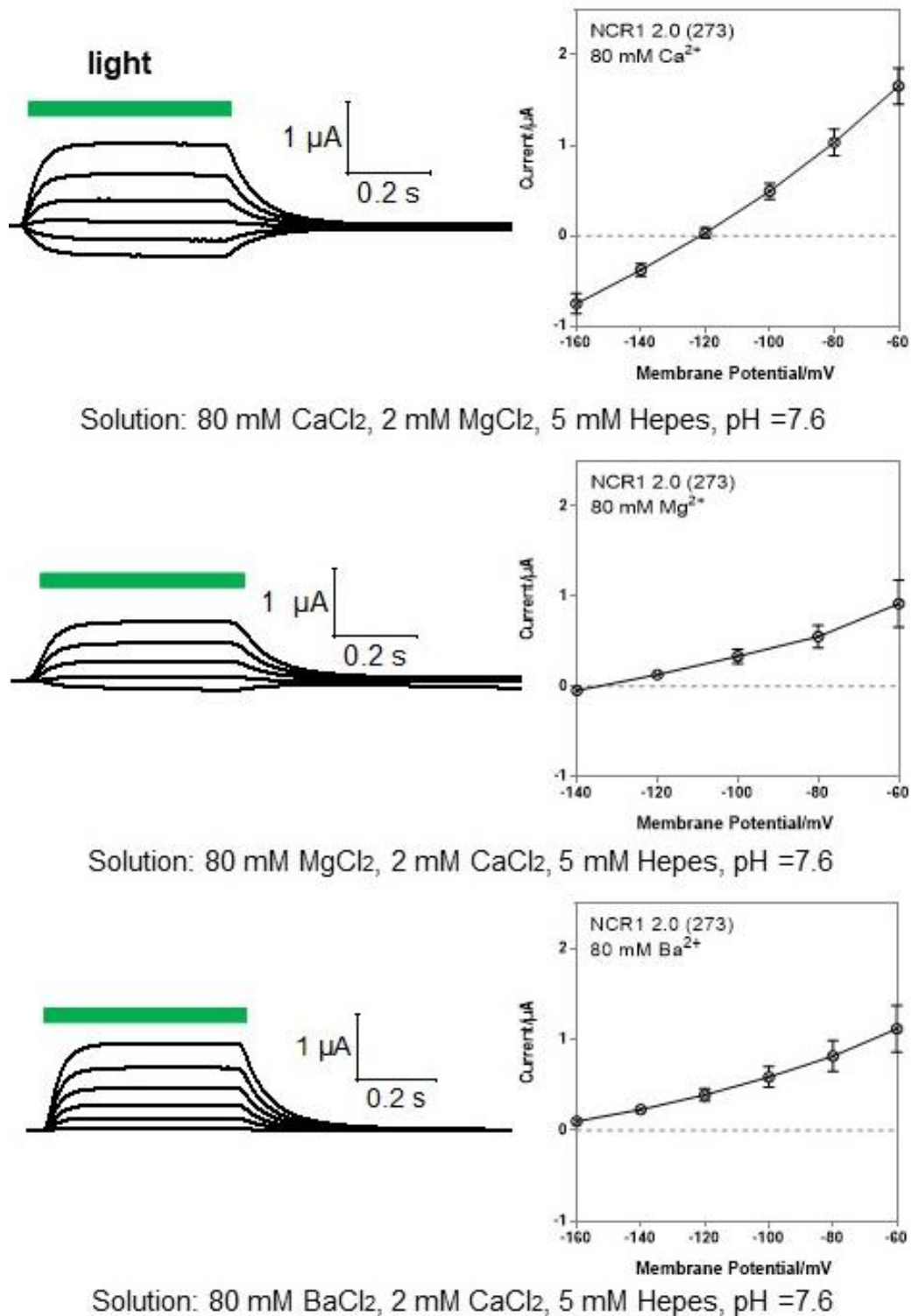Solution: 80 mM BaCl₂, 2 mM CaCl₂, 5 mM Hepes, pH =7.6

Fig 3.9b Analysis of relative permeabilities of NCR1 2.0 for divalent cations at high concentrations.

Representative photocurrent traces and current-potential curves of NCR1 2.0 in different solutions. Photocurrents were measured with oocytes at 2 dpi upon 0.5 s green light (532 nm, 0.5 mW/mm²) illumination, indicated by the green bars. Different holding potentials were used. For the current-potential curves, n = 6 experiments, error bars = SEM.

NCR1 2.0 exhibits inward current under illumination in high Ca^{2+} solution. However, NCR1 2.0 exhibits no significant inward current in high Mg^{2+} or high Ba^{2+} solutions.

The diagram presented representative photocurrent traces recorded in different solutions (Fig 3.9a/b). The trace and reversal potential of NCR1 2.0 (273) varied depending on different solutions. To further explore the ionic permeability of NCR1 2.0 (273), we changed the holding potential from -160 mV to +60 mV and calculated the permeability using the Goldman-Hodgkin-Katz (GHK) equation with the parameters. Our results revealed that the permeability of Na^+ was larger than that of K^+. The permeability ratios of different ions to hydrogen were $Na^+ > Cs^+ > K^+$, no significant currents were observed for Ca^{2+}, Mg^{2+}, or Ba^{2+} (Fig 3.9c).
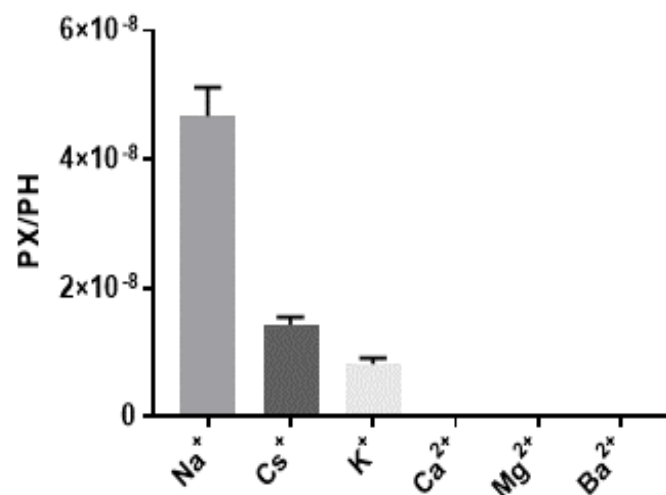

Fig 3.9c The permeability of NCR1 2.0 for different solutions.
The permeability ratios (PX/PH) of NCR1 2.0. For the current-potential curves. Photocurrents were measured with oocytes at 2 dpi upon 0.5 s green light (532 nm, 0.5 mW/mm²) illumination. Different holding potentials were used, n = 6 experiments, error bars = SEM.
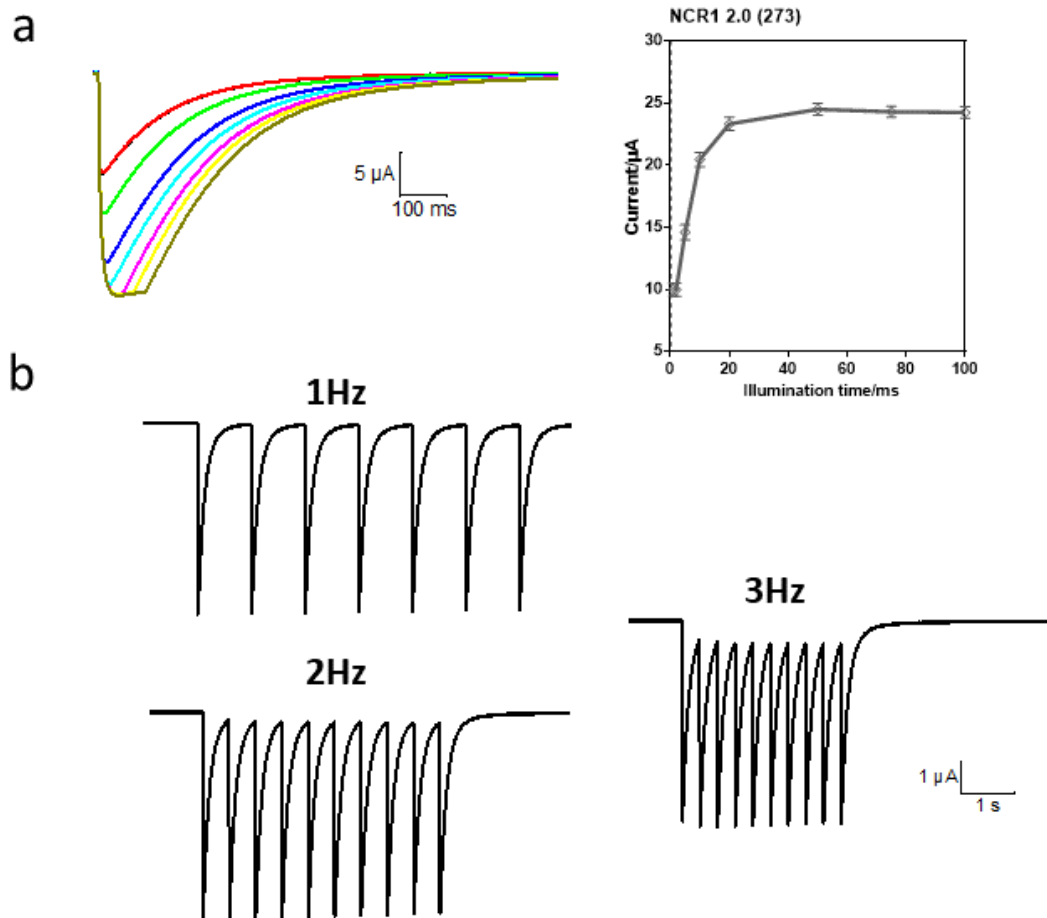
3.1.8 Kinetics of NCR1 2.0

Fig 3.10 Kinetics of NCR1 2.0.

(a) Photocurrent traces and current-potential curves of NCR1 2.0 under various durations of light pulses (1, 2, 5, 10, 20, 50, 75, and 100 ms). Photocurrents were recorded from oocytes 2 days post-injection with holding potentials set at -40 mV. A 532 nm laser at 6 mW/mm² was used. For the current-potential curves, n = 6 experiments, error bars = SEM. (b) Photocurrent traces of NCR1 2.0(273) under different frequencies of light stimulation (1, 2, and 3 Hz), with an illumination time of 1 ms. A 532 nm laser at 6 mW/mm² was used.

Optogenetic tools provide precise control over peak times through short light pulses to activate light-gated ion channels and pumps, such as channelrhodopsin-2 (ChR2) [135-136]. To investigate the relationship between different illumination times and current, a range of illumination times were studied, including 1, 2, 5, 10, 20, 50, 75, and 100 ms (Fig 3.10a). The current of NCR1 2.0 steadily increases as the illumination time is increased from 1 ms to 50 ms, reaching its peak value at a light exposure time of 50 ms. Furthermore, the NCR1 2.0 current peak reaches a steady state when the illumination

time is increased from 50 ms to 100 ms (Fig 3.10a). To optimize the use of optogenetic tools, it is important to determine the reproducible maximum light frequency of NCR1 2.0 in experiments that require repeated light stimulation. In this experiment, the light frequency was varied at 1, 2, and 3 Hz (Fig 3.10b). Our results indicate that the current waveform can be fully recovered and repeated when the light frequency is set to 1 or 2 Hz. However, when the light frequency was increased to 3 Hz, the NCR1 2.0 channels were not closed completely, and the state of NCR1 2.0 did not recover fully. Our findings demonstrate that NCR1 2.0 can be stimulated repeatedly at a light frequency of 2 Hz, and that the evoked current waveform is highly reproducible when the frequency of the light is less than or equal to 2 Hz.
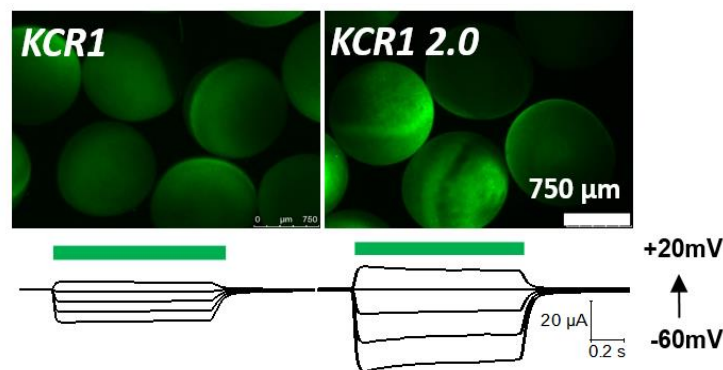
3.2 Optimization and characterization of KCR1

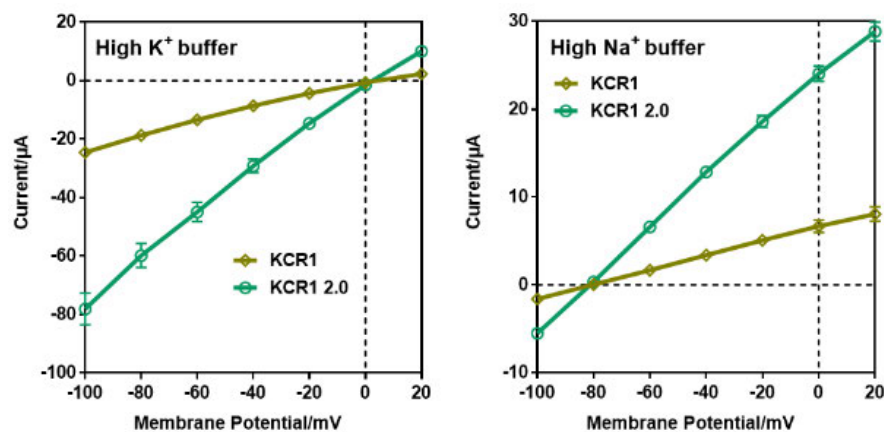### 3.2.1 Improving the expression and photocurrent of KCR1

Fig 3.11 Expression and photocurrent of KCR1.

(a) The schematic diagram of KCR1 and KCR1 2.0. 30 ng KCR1 or 30 ng KCR1 2.0 cRNAs were injected for oocyte expression. (b) Fluorescence images and representative photocurrent traces of KCR1 and KCR1 2.0 at 2dpi with 30 ng cRNAs for each. The green bars indicate the duration of 0.5 s green light illumination, using a 532 nm laser at an intensity of 0.5 mW/mm². The holding potentials ranged from -60 mV to +20 mV. The measurements were performed using the high K^+ solution. (c) Photocurrents of KCR1 and KCR1 2.0 in high Na^+ and high K^+ solutions. Measurements were performed at 2 dpi. 0.5 s 532 nm laser at 0.5 mW/mm² was used for illumination. The holding potentials ranged from -100 mV to +20 mV. n = 6, error bars = SEM.

In addition to sharing the same structure as KCR1, KCR1 2.0 also contains trafficking signals (T) and ER export signal peptides (E) in the C-terminal and LR (enhance expression signal peptide) at the N-terminal (Fig 3.11a). Both KCR1 and KCR1 2.0 groups exhibit fluorescence (Fig 3.11b). The fluorescence intensity and current of KCR1 2.0 were stronger than those of the KCR1 group, indicating that LR and TYE increased the amount of KCR1 expression on the plasma membrane of oocytes. KCR1 2.0 exhibited larger currents than KCR1 in high Na^+ and high K^+ solutions. The reversal potential of KCR1 was the same to that of the KCR1 2.0 group in high Na^+ and high K^+ solutions (Fig 3.11c). The figure presents representative photocurrent traces in high Na^+, high K^+.

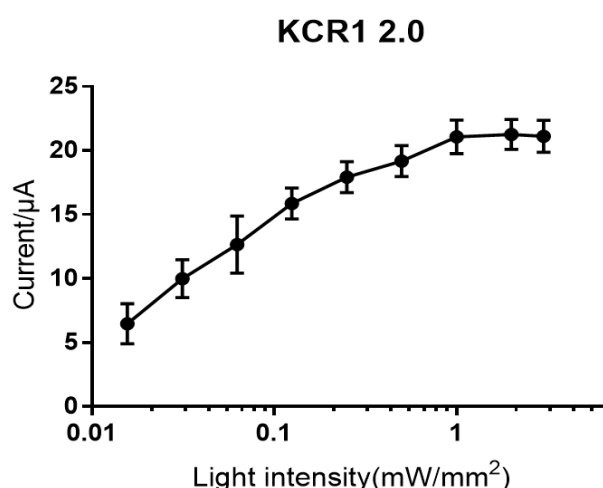### 3.2.2 Light sensitivity of KCR1 2.0

Fig 3.12 Light sensitivity of KCR1 2.0.

Light sensitivity of KCR1 2.0 under different 532 nm light intensities ranging from 0.03 to 3 mW/mm² (0.031, 0.062, 0.125, 0.125, 0.25, 0.5, 1, 2, 3 mW/mm²). 30 ng cRNA was injected into the *Xenopus* oocyte. Photocurrent was measured with extracellular ORi Ca^{2+} solution (Ori, 110 mM

NaCl, 5 mM KCl, 2 mM $CaCl_2$, 1 mM $MgCl_2$, 5 mM HEPES and pH=7.6) at 2 dpi. Holding potential: -40 mV.

The current of KCR1 2.0 exhibits a rapid increase with increasing light intensity from 0.03 to 1 mW/mm², yet the current amplitude does not show any further increment as the light intensity is increased from 1 to 3 mW/mm² (Fig 3.12). The current of KCR1 2.0 reaches saturation when the light intensity is around 1 mW/mm².

NaCl, 5 mM KCl, 2 mM $CaCl_2$, 1 mM $MgCl_2$, 5 mM HEPES and pH=7.6) at 2 dpi. Holding potential: -40 mV.

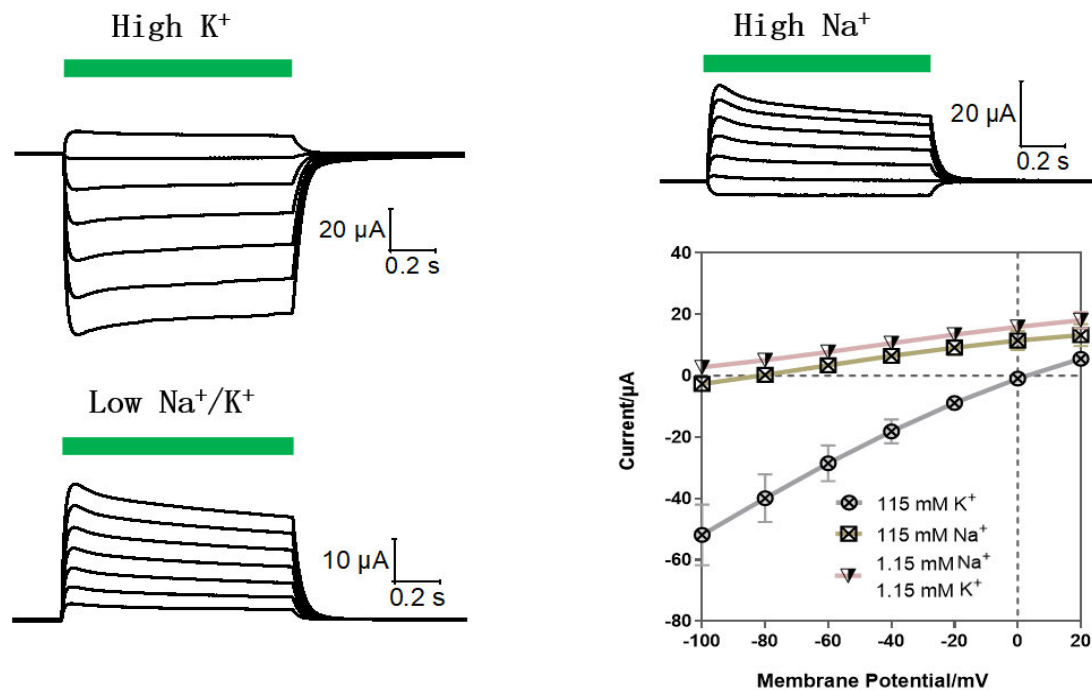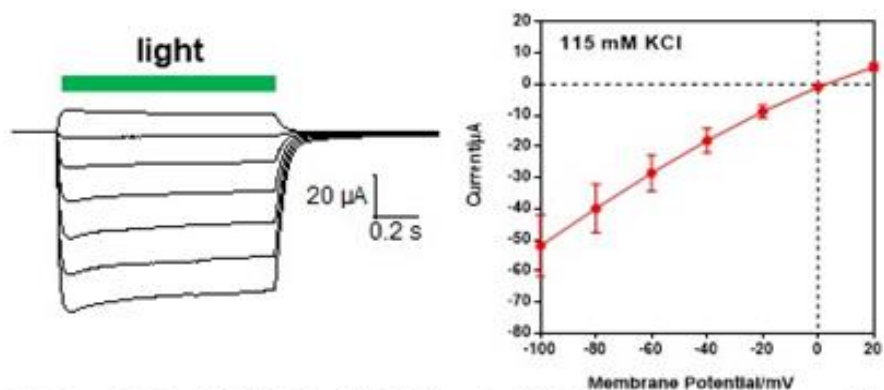### 3.2.3 The current of KCR1 2.0 in Na⁺ and K⁺ solutions

Fig 3.13 The current of KCR1 2.0 in Na⁺ and K⁺ solutions.

Representative photocurrent traces and current-potential curves of KCR1 2.0 in different solutions. Photocurrents were measured with oocytes at 2 dpi upon 0.5 s green light (532 nm, 0.5 mW/mm²) illumination, indicated by the green bars. Holding potentials were changed from -100 mV to +20 mV. For the current-potential curves, n = 6 experiments, error bars = SEM.

Comparing the Na⁺ and K⁺ conductance of KCR1 2.0. Representative photocurrent traces and current-potential curves of different KCR1 2.0 in high Na⁺, high K⁺ and low Na⁺/K⁺ solutions. Photocurrents were measured with oocytes at 2 dpi upon 0.5 s green light (532 nm, 0.5 mW/mm²) illumination, indicated by the green bars. The holding potentials ranged from -100 mV to +20 mV. For the current-potential curves, error bars = SEM, n = 6 experiments.

The reversal potential of KCR1 2.0 was found to be approximately -80 mV in a high Na⁺ solution, whereas it was approximately 0 mV in a high K⁺ solution (Fig 3.13). The permeability of K⁺ over Na⁺ can be calculated from the permeability ratios, a value of P_K/P_{Na} (KCR1 2.0) ≈ 24. The value is calculated using the Goldman-Hodgkin-Katz (GHK) equation.
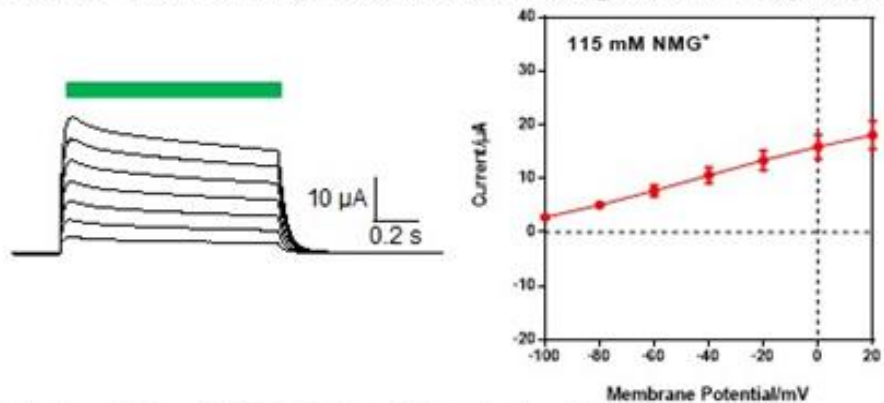
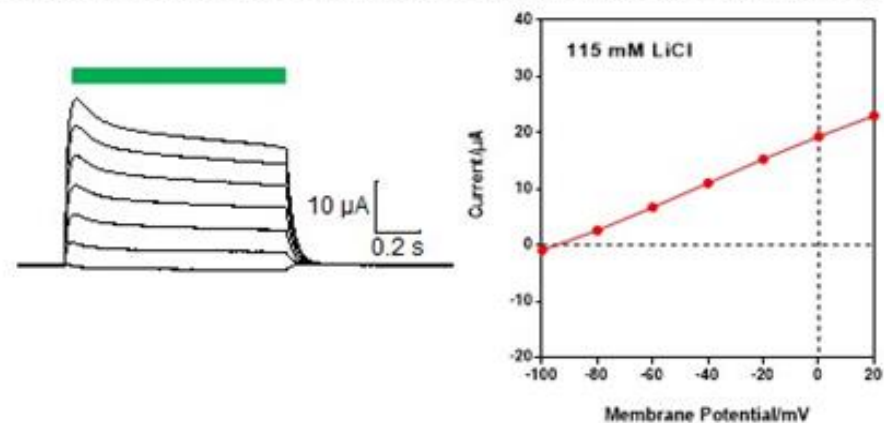## 3.2.4 The ion selectivity of KCR1 2.0

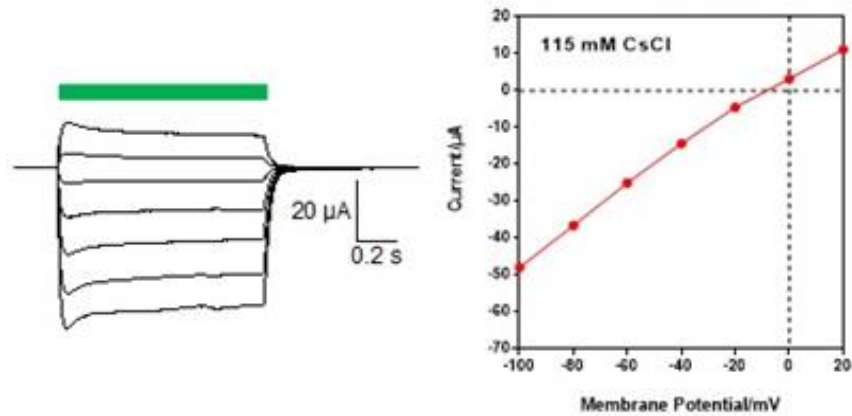Solution: 115 mM KCl, 2 mM BaCl₂, 1 mM MgCl₂, 5 mM Hepes, pH = 7.6
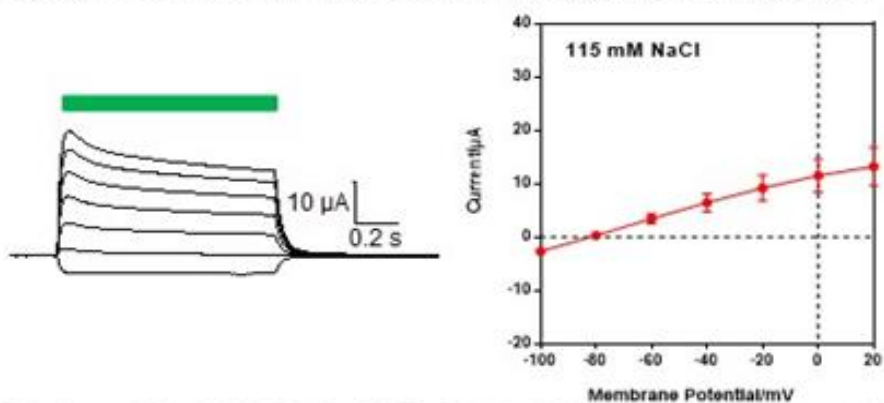
Solution: 115 mM NaCl, 2 mM BaCl₂, 1 mM MgCl₂, 5 mM Hepes, pH = 7.6

Solution: 115 mM NMGCl, 2 mM BaCl₂, 1 mM MgCl₂, 5 mM Hepes, pH = 7.6

Solution: 115 mM LiCl, 2 mM BaCl₂, 1 mM MgCl₂, 5 mM Hepes, pH = 7.6

Solution: 115 mM CsCl, 2 mM BaCl₂, 1 mM MgCl₂, 5 mM Hepes, pH = 7.6

Fig 3.14a Analysis of relative permeabilities of KCR1 2.0 for high monovalent solutions.
Representative photocurrent traces and current-potential curves of KCR1 2.0 in different solutions.
Photocurrents were measured with oocytes at 2 dpi upon 0.5 s green light (532 nm, 0.5 mW/mm²)
illumination, indicated by the green bars. Different holding potentials were used. For the current-
potential curves, n = 6 experiments, error bars = SEM.

KCR1 2.0 exhibits inward current in the aforementioned solutions under illumination,
indicating its permeability to K^+, Na^+, Li^+ and Cs^+.

Solution: 57.5 mM MgCl₂, 2 mM BaCl₂, 5 mM Hepes, pH = 7.6
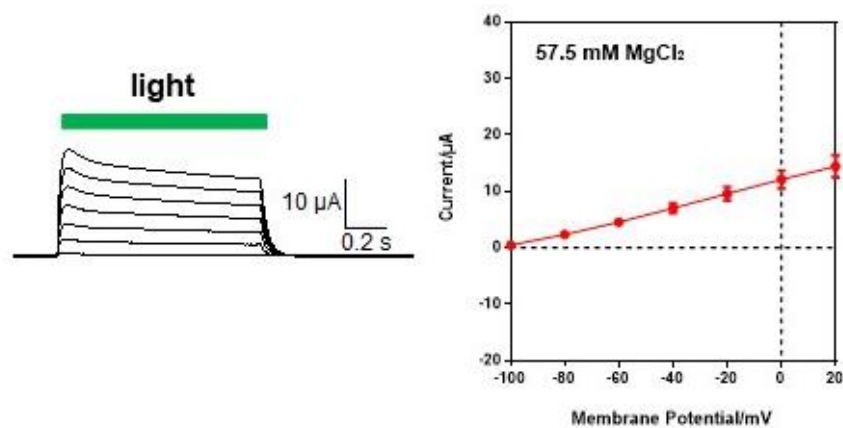

Solution: 57.5 mM BaCl₂, 1 mM MgCl₂, 5 mM Hepes, pH = 7.6

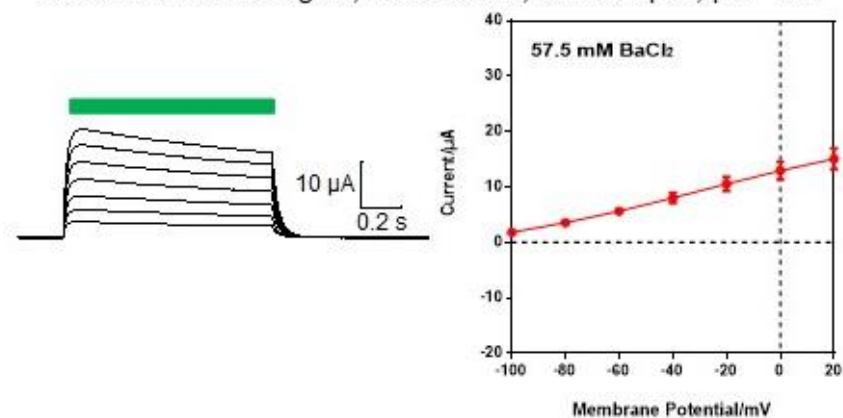Solution: 57.5 mM CaCl₂, 1 mM MgCl₂, 5 mM Hepes, pH = 7.6)
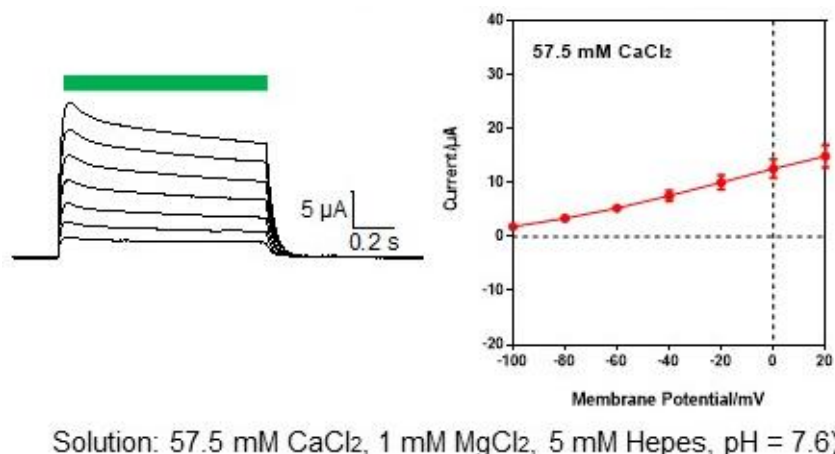
Fig 3.14b Analysis of relative permeabilities of KCR1 2.0 for high divalent solutions.
Representative photocurrent traces and current-potential curves of NCR1 2.0 in different solutions. Photocurrents were measured with oocytes at 2 dpi upon 0.5 s green light (532 nm, 0.5 mW/mm²) illumination, indicated by the green bars. Different holding potentials were used. For the current-potential curves, n = 6 experiments, error bars = SEM.

KCR1 2.0 exhibits no obvious inward current in high Ca^{2+} solution, high Mg^{2+} solution, and high Ba^{2+} solution under green light illumination.

Fig 3.14c The permeability of KCR1 2.0 for different solutions.
The permeability ratios (P_X/P_K) of KCR1 2.0. For the current-potential curves. Photocurrents were measured with oocytes at 2 dpi upon 0.5 s green light (532 nm, 0.5 mW/mm²) illumination. Different holding potentials were used, n = 6 experiments, error bars = SEM.

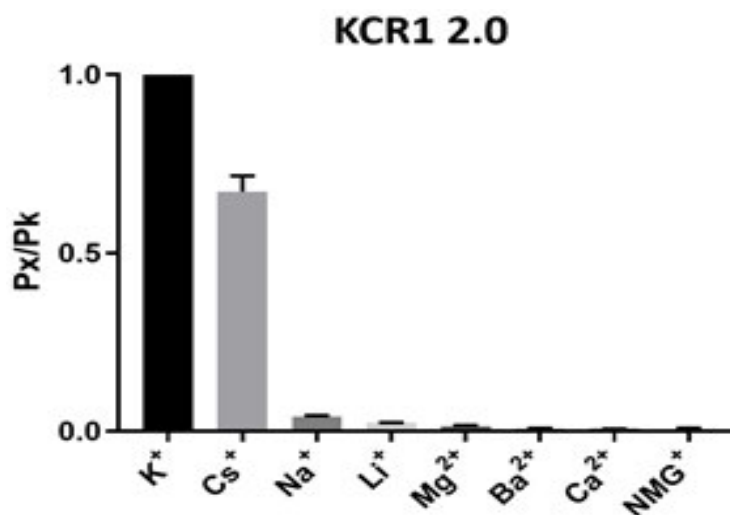Representative photocurrent traces, recorded in different solutions, are shown in Fig 3.14a/b. The reversal potential of KCR1 2.0 current traces varied depending on different solutions. To further explore the ionic permeability of KCR1 2.0, we changed the holding potential from -100 mV to +20 mV and calculated the permeability using the Goldman-Hodgkin-Katz (GHK) equation with the parameters. Our results revealed that the permeability to K^+ was larger than that to Na^+. The permeability ratios (P_k/P_{Na}) of KCR1 2.0 were determined as follows: $P_k/P_{Na}\approx24$, where permeability is in the order of $K^+ > Cs^+ > Na^+$. There were no currents observed for Ca^{2+}, Mg^{2+}, or Ba^{2+} (Fig 3.14c).

3.2.5 Kinetics of KCR1 2.0

Fig 3.15 Kinetics of KCR1 2.0.
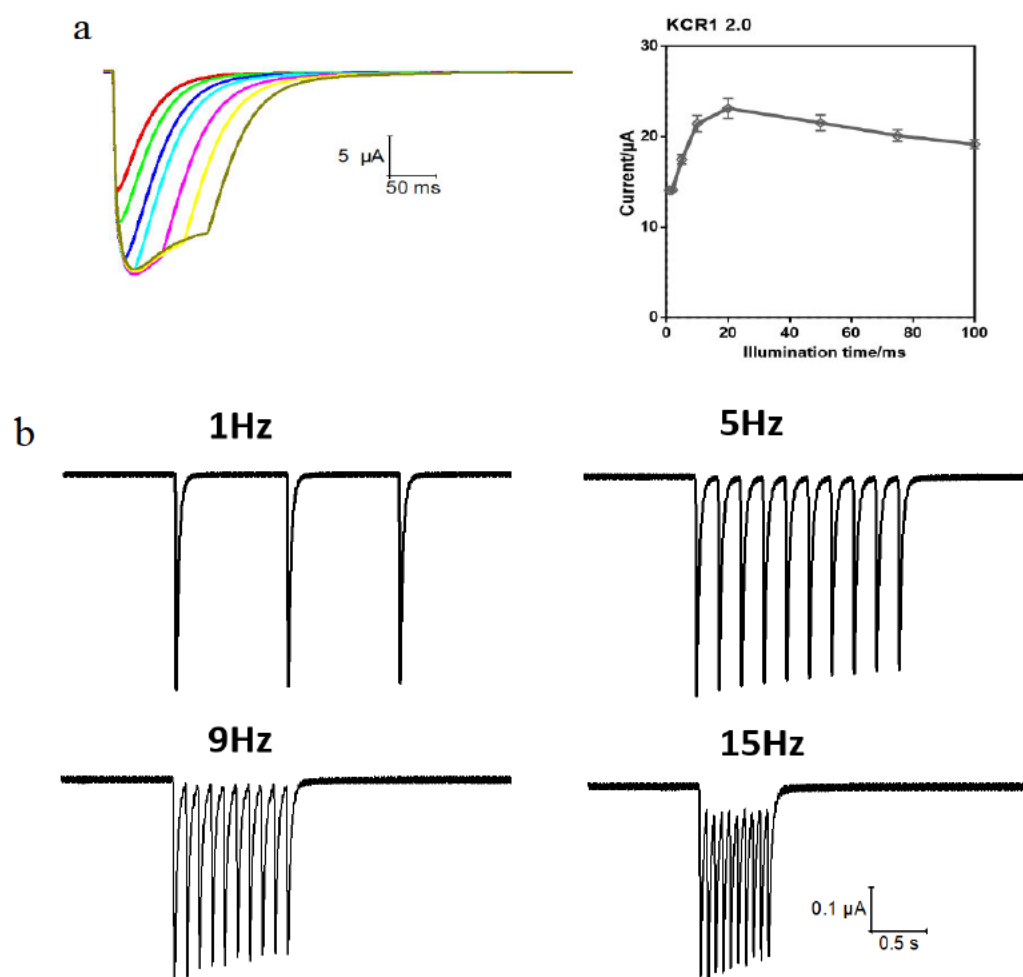
(a) Photocurrent traces and current-potential curves of KCR1 2.0 under various durations of light pulses (1, 2, 5, 10, 20, 50, 75, and 100 ms). Photocurrents were recorded from oocytes 2 dpi with holding potentials set at -40 mV. A 532 nm laser at 6 mW/mm² was used. For the current-potential curves, n = 6 experiments, error bars = SEM. (b) Photocurrent traces of KCR1 2.0 under different

frequencies of light stimulation (1, 5, 9 and 15Hz), with an illumination time of 1 ms. A 532 nm laser at 6 mW/mm² was used.

To investigate the correlation between different illumination durations and current, we did experiments with various illumination times: 1, 2, 5, 10, 20, 50, 75, and 100 ms. The current of KCR1 2.0 increased with the increase in illumination time up to 20 ms (Fig 3.15a). The peak current value of KCR1 2.0 was achieved when the light exposure time was 20 ms. The KCR1 2.0 current peak reached a steady state when the illumination time varied from 20 ms to 100 ms (Fig 3.15a). To ensure better utilization of optogenetic tools, it is essential to determine the maximum reproducible light frequency of KCR1 2.0 in experiments that require repeated light stimulation. We set the light frequency to 1, 5, 9, and 15 Hz, respectively (Fig 3.15b). It can be observed from Fig 3.15b that the current waveform can be recovered fully and repeatedly when the light frequency is 1, 5, and 9 Hz, respectively. The KCR1 2.0 channels did not close entirely, and the state of KCR1 2.0 did not recover entirely when the light frequency was 15 Hz. KCR1 2.0 can be repeatedly stimulated when the light frequency is around 9 Hz. Our results indicate that the evoked current waveform of KCR1 2.0 is highly reproducible when the frequency of the light is less than or equal to 9 Hz.

3.3 Light-induced water transport

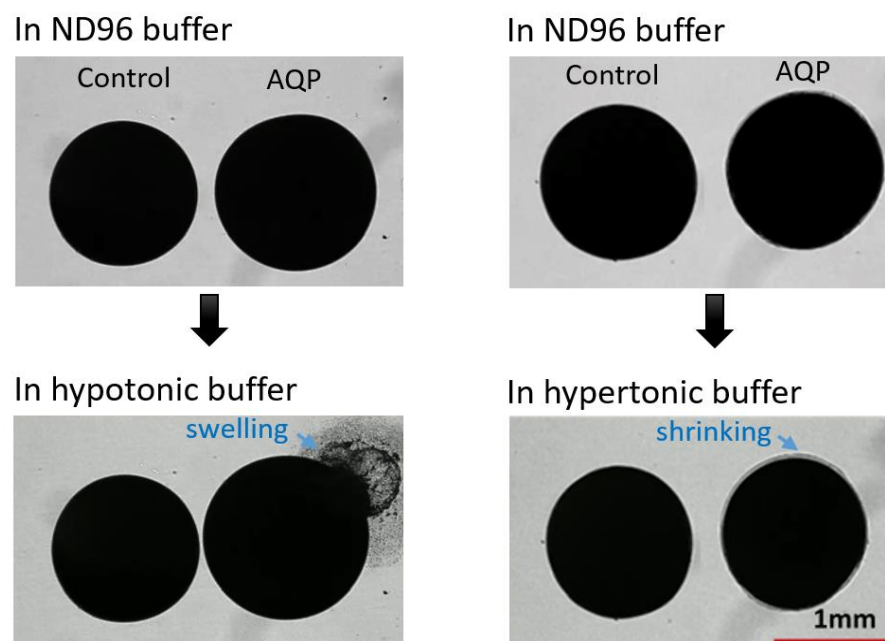### 3.3.1 The AQP1-expressing oocyte in hypertonic or hypotonic solution

Fig 3.16 The AQP1-expressing oocyte in hypertonic or hypotonic solution.

The oocytes were injected with 5 ng of AQP1 cRNA and expressed for 2 days in ND96 solution. The control oocytes were injected with water. The oocytes were tested at 2 dpi in hypertonic solution (2x ND96 containing 192 mM NaCl) or hypotonic solution (water containing 0 mM NaCl). The morphological changes were recorded at different time points using the Leica DMi8 microscope. The blue arrow indicated the separation of the cytoplasmic membrane from the vitelline membrane due to water efflux. The blue arrow indicated the explosive point of the oocytes under the accumulated pressure of water influx.

In order to evaluate the functionality of AQP1, its expression in oocytes was tested by exposing the oocytes to three different solutions: physiological solution (ND96), hypotonic solution (water) and hypertonic solution (2×ND96). Under physiological conditions (ND96), the oocyte morphology remained unchanged. However, under hypotonic conditions, where the osmolarity inside the oocyte is larger than that of the external solution, water was absorbed by the oocyte through AQP1, resulting in an increase in oocyte volume to the point of rupture.

In the hypertonic solution, due to the lower osmolarity inside the oocyte compared to the external solution, water flows through the AQP1 to the external hypertonic solution, causing the oocyte to gradually decrease in volume until it reaches a certain point. As illustrated in the figure, no changes in the morphology of the control and AQP1-injected oocytes were observed after 10 minutes of exposure to the physiological solution (ND96). However, when placed in the hypotonic solution (water), both the control and AQP1-injected oocytes swelled, with the AQP1-injected oocytes eventually rupturing.

In the control group, no significant changes were observed in the morphology of the oocytes. However, in the group where AQP1 was injected, when transferred to the hypertonic solution, the volume of the oocytes gradually decreased until the osmolarity inside and outside the oocyte reached equilibrium, resulting in the visible gap between the cytoplasmic and vitelline membranes within 10 minutes. In contrast, there was no morphological change in the control group where no AQP1 was injected. The successful expression of AQP1 in oocytes and its function in accelerating water transport make it a promising candidate for use in future experiments involving optogenetic tools to regulate water flow in oocytes.

3.3.2 Expression and photocurrent of XXM 2.0 and *Gt*ACR1 in *Xenopus* oocyte
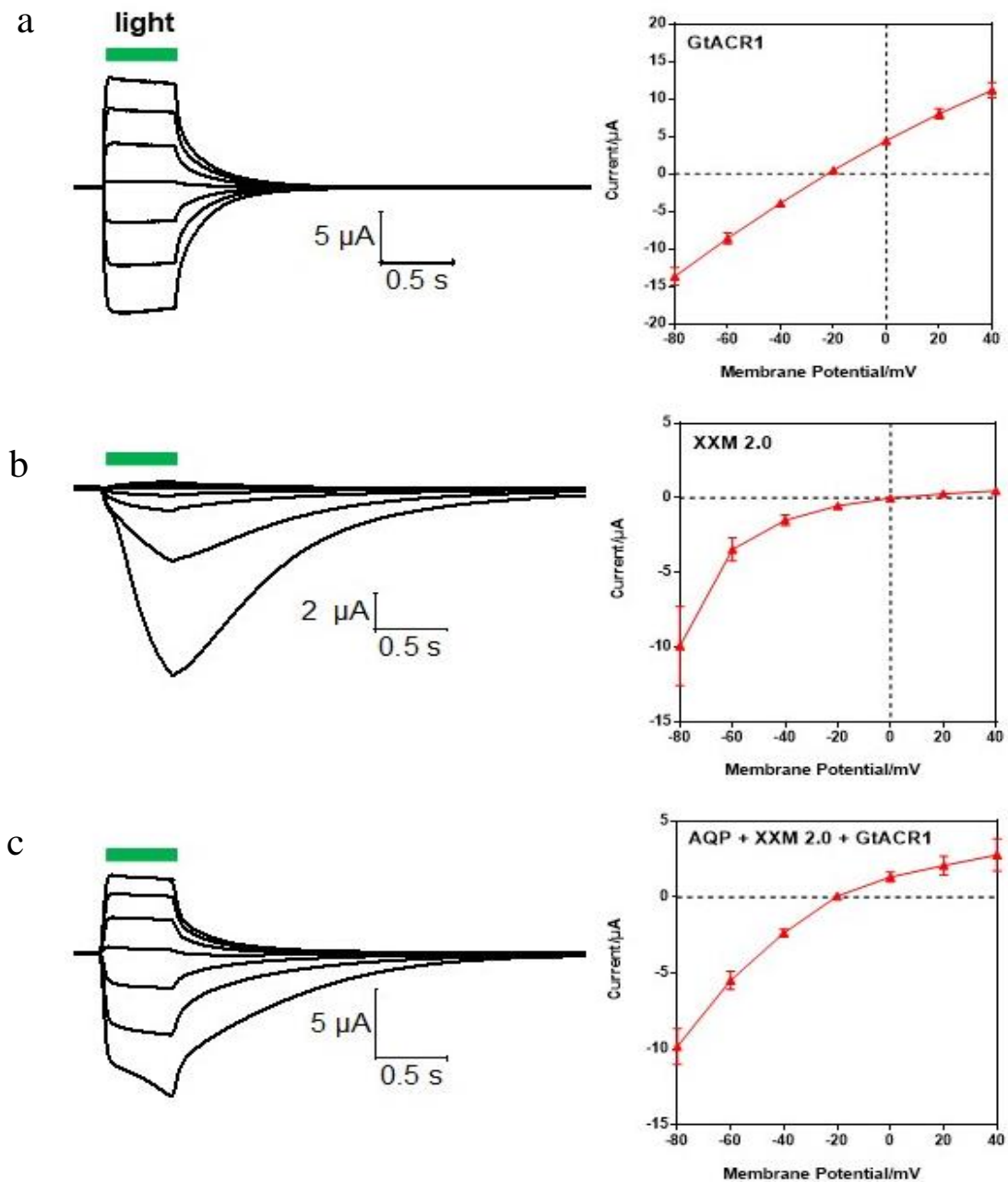
Fig 3.17 Co-expression of XXM 2.0 and *Gt*ACR1 in *Xenopus* oocyte in ND96 buffer.

(a) The current of *Gt*ACR1. (b) The current of XXM 2.0. (c) The current of AQP1, *Gt*ACR1, and XXM 2.0. 5 ng AQP1, 20 ng XXM 2.0, 5 ng *Gt*ACR1 by single or mixed cRNA injection into oocytes were expressed in ND96 buffer (96 mM NaCl, 2 mM KCl, 1 mM MgCl$_2$, 5 mM Hepes, pH=7.6) for two days. The green bars indicate the duration of 0.5 s green light illumination, using a 532 nm laser at an intensity of 0.5 mW/mm². The holding potentials ranged from -80 mV to +40 mV. For the current-potential curves, error bars = SEM, n = 6 experiments.

Validation of expression and function of optogenetic tools is necessary prior to performing oocyte shrinking and swelling experiments. To regulate ion concentrations in oocytes, osmotic gradients are generated using optogenetic tools. This osmotic gradient facilitates the formation of electrochemical driving forces and enables passive transport of ions and water. In order to create osmotic gradients by changing ion concentration, the light-gated cation channel XXM 2.0 is expressed in *Xenopus* oocytes and cation (Na^+) influx is detected in the ND96 buffer under green light illumination. Currents can be detected either by expressing XXM 2.0 or *Gt*ACR1 alone in *Xenopus* oocytes under green light illumination (Figure 3.17a/b). Furthermore, currents can also be detected when co-expressing XXM 2.0 and *Gt*ACR1 in *Xenopus* oocytes (Figure 3.17c), indicating that XXM 2.0 and *Gt*ACR1 can be co-expressed and work together in *Xenopus* oocytes. XXM 2.0 or co-expression of XXM 2.0 and *Gt*ACR1 in *Xenopus* oocytes have similar reversal potentials. For channel closing time, oocytes co-expressing XXM 2.0 and *Gt*ACR1 were slower than those expressing *Gt*ACR1, but similar to those expressing XXM 2.0. The efficacy of oocyte shrinking and swelling experiments is influenced by the optogenetic tool type, the external solution, the type of light, and the intensity of the light utilized.

3.3.3 Expression and photocurrent of NCR1 2.0 and *Gt*ACR1 in *Xenopus* oocyte

NCR1, a light-gated cation channel, exhibits significantly larger photocurrents when compared to the light-gated cation channel XXM 2.0. In *Xenopus* oocytes, AQP1, XXM 2.0 and *Gt*ACR1 were validated to be expressed and functional. Moreover, an additional toolbox, comprising AQP1, NCR1 2.0 and *Gt*ACR1, was designed and validated. To validate that NCR1 2.0 and *Gt*ACR1 can co-express and work together in *Xenopus* oocytes, XXM 2.0 was replaced with NCR1 2.0. As illustrated in Figure 3.18a/b, currents were observed when NCR1 2.0 or *Gt*ACR1 was expressed alone in *Xenopus* oocytes. Similarly, currents were detected when NCR1 2.0 and *Gt*ACR1 were co-expressed in oocytes (Figure 3.18c), suggesting that NCR1 2.0 and *Gt*ACR1 can co-express and work in oocytes. In terms of channel closing times, oocytes co-expressing NCR1 2.0 and *Gt*ACR1 exhibited similar channel closing times than oocytes expressing *Gt*ACR1 alone, and exhibited similar channel closing times as oocytes expressing NCR1 2.0. The above experiments demonstrate that AQP1, NCR1 2.0 and *Gt*ACR1 can be expressed and function together in oocytes.
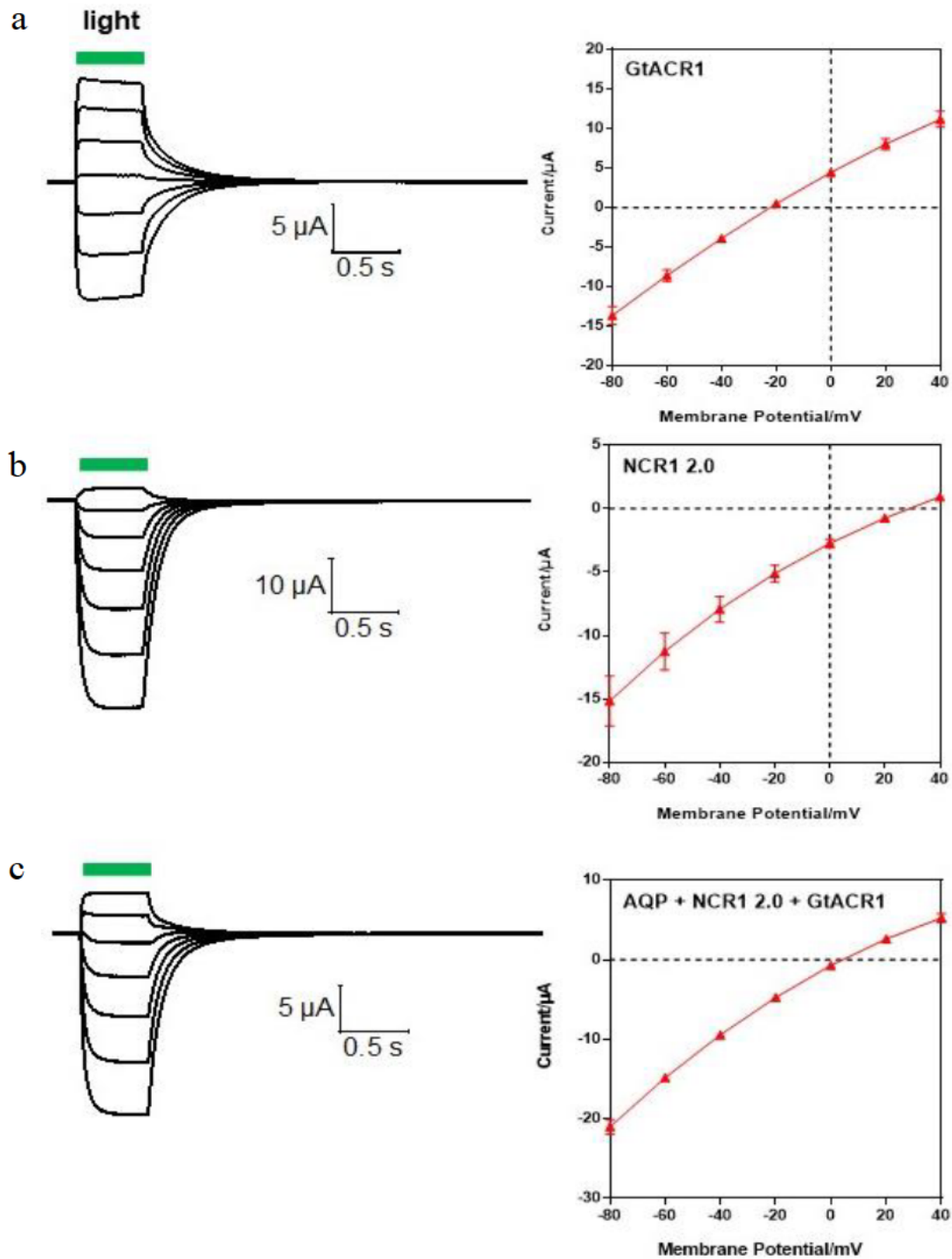
Fig 3.18 Co-expression of NCR1 2.0 and *Gt*ACR1 in *Xenopus* oocyte in ND96 buffer.

(a) The current of *Gt*ACR1. (b) The current of NCR1 2.0. (c) The current of AQP1, *Gt*ACR1, and NCR1 2.0. 5 ng AQP1, 20 ng NCR1 2.0, 5 ng *Gt*ACR1 by single or mixed cRNA injection into oocytes were expressed in ND96 buffer (96 mM NaCl, 2 mM KCl, 1 mM $MgCl_2$, 5 mM Hepes, pH=7.6) for two days. The green bars indicate the duration of 0.5 s green light illumination, using a 532 nm laser at an intensity of 0.5 mW/mm². The holding potentials ranged from -80 mV to +40 mV. For the current-potential curves, error bars = SEM, n = 6 experiments.

3.3.4 Light-induced oocyte swelling in ND96 buffer via Na$^+$/Cl$^-$ influx
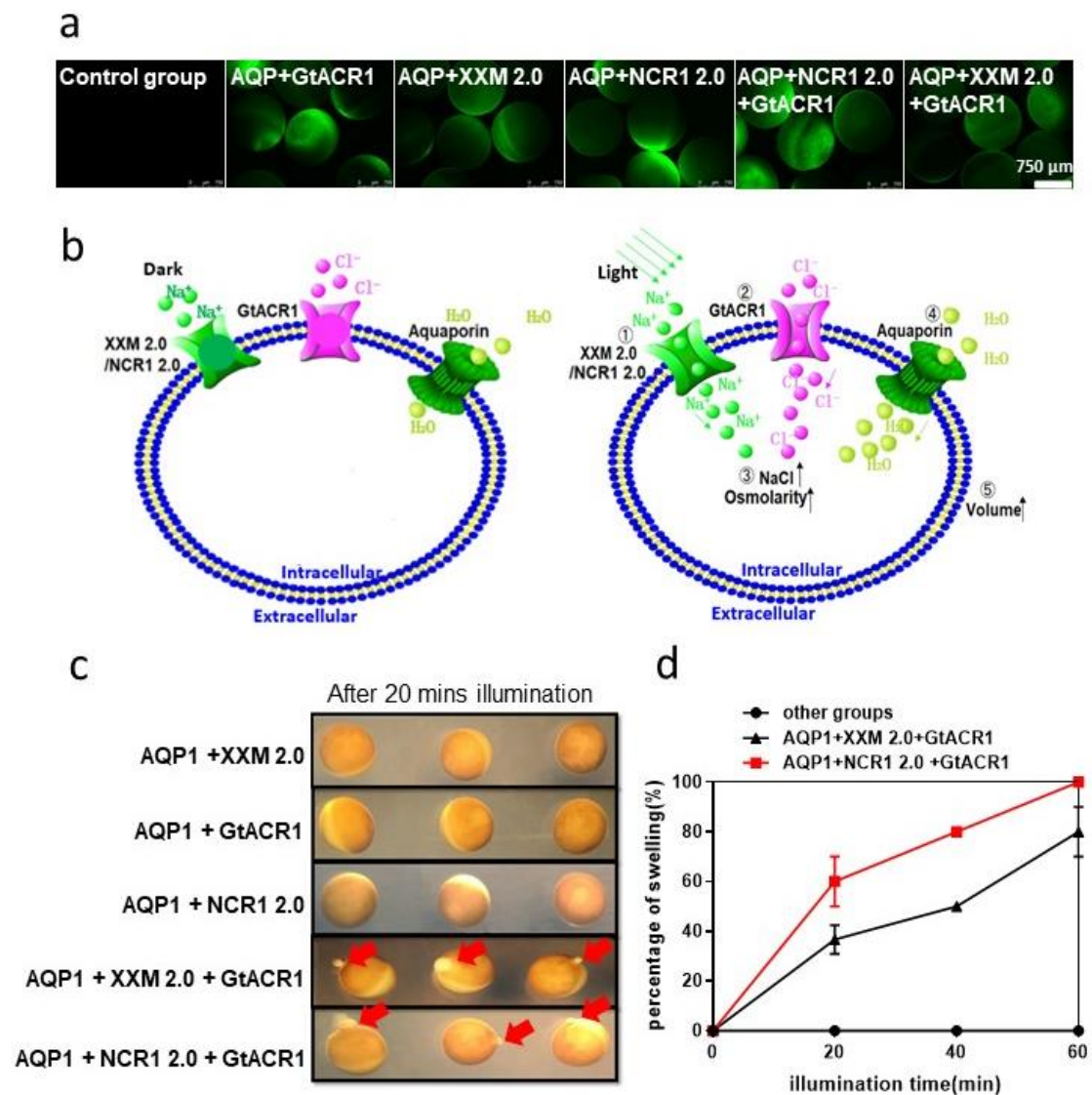
Fig 3.19 Combine the NCR1 2.0 and *Gt*ACR1 for light-controlled water influx into the oocytes.
(a) Fluorescence pictures of oocytes after expressing different proteins. 5 ng AQP1, 20 ng XXM 2.0, 20 ng NCR1 2.0, and 5 ng *Gt*ACR1 by single cRNA injection or mixture injection to oocytes were expressed for two days in ND 96 buffer. Pictures were taken at 2 dpi in ND96 buffer. (b) The schematic diagram shows the water transport through the AQP1 driven by the ion gradients created by the Na$^+$ and Cl$^-$ channels. The aquaporin AQP1 is constitutively active. NCR1 2.0 and *Gt*ACR1 channels are opened by the green light illumination. (c) Light-induced oocyte swelling in ND96 buffer after expressing different combinations of channels for 2 days. The oocyte swelling was indicated by the rupture at the red arrow-marked positions. The oocytes were illuminated by 520 nm LEDs with light intensity of 400 μW/mm². Red arrow: the explosive part in oocytes. cRNA amount: 5 ng AQP1, 20 ng XXM 2.0, 20 ng NCR1 2.0, 5 ng *Gt*ACR1. (d) Oocytes swelling efficacy after different times of green light illumination. The number of swelling oocytes was recorded every 20 min. error bars = SEM, n = 6 groups, each with 10 oocytes.

As shown in Figure 3.19a, no fluorescence was observed in the control group, but obvious fluorescence was detected in the following groups: (1) AQP1+GtACR1, (2) AQP1+XXM 2.0, (3) AQP1+NCR1 2.0, (4) AQP1+XXM 2.0+GtACR1, and (5) AQP1+NCR1 2.0+GtACR1, indicating successful expression in oocytes. Two groups were designed to inject oocytes with three different channels: AQP1, XXM 2.0, and GtACR1 or AQP1, NCR1 2.0, and GtACR1 expressed in oocytes, respectively. AQP1 remains open while XXM 2.0, GtACR1, and NCR1 2.0 are closed in darkness. All channels open under green light illumination (Figure 3.19b).

XXM 2.0, GtACR1, and NCR1 2.0 can regulate the solute concentration inside and outside the cell membrane. Passive water transport across the plasma membrane of oocytes occurs in response to the osmotic gradient formed by the movement of solutes. It has been reported that the Na^+ concentration in the $Xenopus$ oocyte cytoplasm is ~10 mM, and the Cl^- concentration is ~50 mM [7].

To create an osmotic gradient by changing the Na^+ concentration in $Xenopus$ oocytes, the light-gated cation channel NCR1 2.0 or XXM 2.0 was expressed (Fig 3.19b). We hypothesized that based on the Na^+ influx formation by NCR1 2.0 or XXM 2.0 in ND96 buffer, the membrane potential of oocytes could become more positive, creating an electrochemical driving force that facilitates the movement of anions. If the light-gated anion channel GtACR1 was also expressed in the oocytes, it would further accelerate osmotic gradient formation via Cl^- influx. To accelerate water transport based on the osmotic gradient, mammalian AQP1 was expressed in $Xenopus$ oocytes. The increase in osmolality leads to a large influx of water, causing the oocytes to increase in volume until rupture.

To simulate physiological conditions, we used ND96 buffer to evaluate the efficiency of water transport based on the osmotic gradient generated by Na^+/Cl^- influx. Five groups containing different channel proteins were designed to compare the water uptake efficiency of oocytes expressing these channels: (1) AQP1+GtACR1, (2) AQP1+XXM 2.0, (3) AQP1+NCR1 2.0, (4) AQP1+XXM 2.0+GtACR1, and (5) AQP1+NCR1 2.0+GtACR1 (Fig 3.19c). After 20 minutes of green light illumination, oocytes in groups (4) and (5) exhibited significant membrane swelling and rupture, while no changes were observed in the other groups (Fig 3.19c). Oocytes only swelled

and ruptured when AQP1, light-gated cation channels (XXM 2.0 or NCR1 2.0), and the light-gated anion channel (*Gt*ACR1) were co-expressed. Expressing only two types of channels did not cause oocytes to rupture. These results suggest that the co-expression of AQP1, light-gated cation channels, and light-gated anion channels is necessary to induce oocyte swelling until they rupture. The group (5) co-expressing AQP1, NCR1 2.0, and *Gt*ACR1 showed the largest water transport efficiency, which was larger than that of group (4) under green light illumination for one hour (Fig 3.19d). This indicates that NCR1 2.0 has a larger Na^+ permeability than XXM 2.0 under green light illumination.

3.3.5 Expression and photocurrent of KCR1 2.0 and *Gt*ACR1 in *Xenopus* oocyte
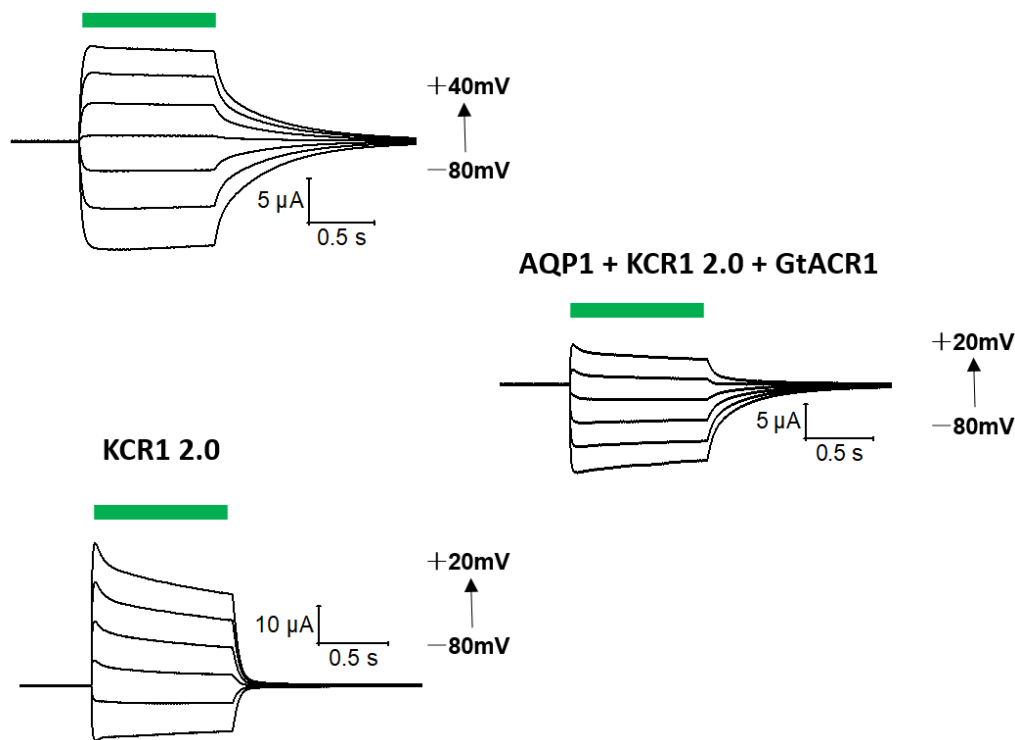
Fig 3.20 Co-expression of KCR1 2.0 and *Gt*ACR1 in *Xenopus* oocyte in ND96 buffer.
The current of *Gt*ACR1 and KCR1 2.0. 5 ng AQP1, 20 ng KCR1 2.0, 5 ng *Gt*ACR1 by single or mixed cRNA injection into oocytes were expressed in ND96 buffer (96 mM NaCl, 2 mM KCl, 1 mM $MgCl_2$, 5 mM Hepes, pH=7.6) for two days. The green bars indicate the duration of 0.5 s green light illumination, using a 532 nm laser at an intensity of 0.5 mW/mm². Different holding potentials were used. For the current-potential curves, n = 6 experiments.

5 ng AQP1, 20 ng KCR1 2.0, 5 ng *Gt*ACR1 by single or mixed cRNA injection into oocytes were expressed in ND96 buffer (96 mM NaCl, 2 mM KCl, 1 mM $MgCl_2$, 5

mM Hepes, pH=7.6) for two days. The green bars indicate the duration of 0.5 s green light illumination, using a 532 nm laser at an intensity of 0.5 mW/mm². The holding potentials ranged from -80 mV to +40 mV. For the current-potential curves, n = 6 experiments.

The experiments described above were aimed at regulating the swelling or shrinking of *Xenopus* oocytes through the use of light-gated cation channels, in which the predominant cations are Na^+. However, since there is also a large amount of K^+ present in *Xenopus* oocytes, it would be a novel approach to adjust the osmotic pressure in the membrane by regulating the concentrations of K^+ and Cl^-, thus controlling the swelling or shrinking of *Xenopus* oocytes.

A novel light-gated potassium channel, KCR1 2.0, was discovered with high permeability for K^+ and a photocurrent larger than that of NCR1 2.0 and XXM 2.0. The expression and functionality of AQP1, XXM 2.0, and *Gt*ACR1 were also confirmed in *Xenopus* oocytes. Furthermore, the additional toolbox comprising AQP1, KCR1 2.0, and *Gt*ACR1 has been designed and validated for use in oocytes. To verify that *Gt*ACR1 and KCR1 2.0 can be co-expressed and work together in *Xenopus* oocytes, XXM 2.0 was replaced by KCR1 2.0. TEVC was then performed to compare oocytes expressing *Gt*ACR1 and KCR1 2.0 under different holding potentials in ND96 buffer.

The currents were detected when KCR1 2.0 was expressed alone in *Xenopus* oocytes. Moreover, currents were also detected when KCR1 2.0 and *Gt*ACR1 were co-expressed in *Xenopus* oocytes (Figure 3.20), indicating that these two channels can be co-expressed and function together in oocytes. The above experiments indicated that AQP1, KCR1 2.0, and *Gt*ACR1 can be expressed and can cooperate in *Xenopus* oocytes. The closing times of the light-gated channels were evaluated in *Xenopus* oocytes co-expressing KCR1 2.0 and *Gt*ACR1, compared to oocytes expressing KCR1 2.0 or *Gt*ACR1 alone. It was observed that oocytes co-expressing KCR1 2.0 and *Gt*ACR1 had slower channel closing times compared to KCR1 2.0 alone but faster compared to *Gt*ACR1 alone. These findings suggest that AQP1, KCR1 2.0 and *Gt*ACR1 can be successfully expressed and functionally cooperate in *Xenopus* oocytes.

3.3.6 Light-induced oocyte swelling in high K$^+$ solution via K$^+$/Cl$^-$ influx
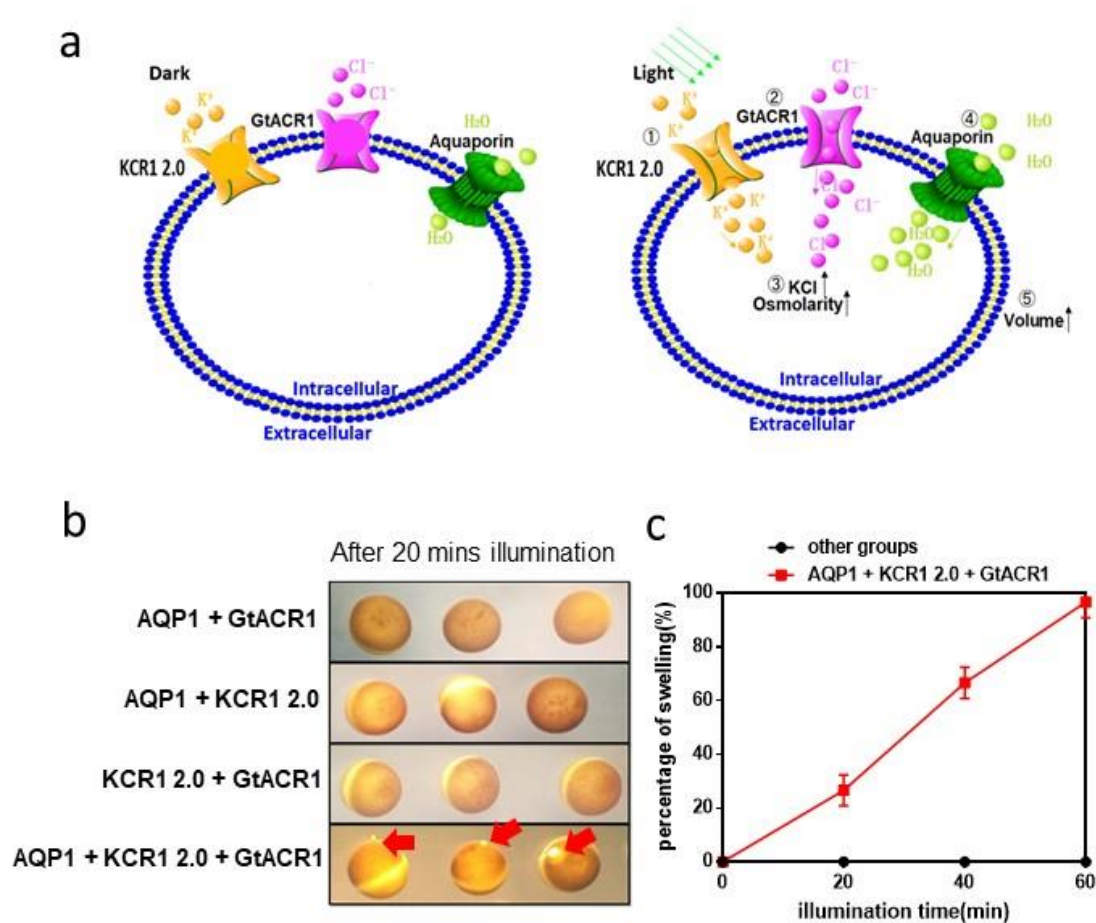

Fig 3.21 Expression and photocurrent of KCR1 2.0.

(a) The schematic diagram shows the water transport through the AQP1 driven by the ion gradients created by the K$^+$ and Cl$^-$ channels. The aquaporin AQP1 is constitutively active. KCR1 2.0 and *Gt*ACR1 channels are opened by the green light illumination. (b) Light-induced oocyte swelling in high K$^+$ solution after expressing different combinations of channels for 2 days. The oocyte swelling was indicated by the rupture at the red arrow-marked positions. The oocytes were illuminated by 520 nm LEDs with light intensity of 400 μW/mm². Red arrow: the explosive part in oocytes. cRNA amount: 5 ng AQP1, 20 ng KCR1 2.0, 5 ng *Gt*ACR1. (c) Oocytes swelling efficacy after different times of green light illumination. The number of swelling oocytes was recorded every 20 min. error bars = SEM, n = 6 groups, each with 10 oocytes.

AQP1, KCR1 2.0, and *Gt*ACR1 were expressed in *Xenopus* oocytes. AQP1 remained open while KCR1 2.0 and *Gt*ACR1 were closed in darkness. Upon green light illumination, all channels opened (Fig 3.21a). The osmotic gradient formed by the movement of solutes drives the passive water transport across the plasma membrane of cells.

To generate an osmotic gradient by changing K^+ in *Xenopus* oocytes, we expressed the light-gated cation channel KCR1 2.0 to induce K^+ influx. Our hypothesis was that this would create a more positive membrane potential, driving the movement of anions Cl^- and facilitating osmotic gradient formation. We further expressed the light-gated anion channel *Gt*ACR1 to accelerate the osmotic gradient formation via Cl^- influx. To increase water transport efficiency based on the osmotic gradient, we expressed mammalian AQP1 in *Xenopus* oocytes. The increase in osmolality leads to a large influx of water which causes the oocytes to swell in volume until the rupture. We tested water transport efficiency using high K^+ solution based on the osmotic gradient produced by K^+/Cl^- influx and designed five groups containing different channel proteins. Water uptake efficiency was compared among oocytes expressing the following groups of proteins: (1) AQP1+*Gt*ACR1, (2) AQP1+KCR1 2.0, (3) KCR1 2.0+*Gt*ACR1, (4) AQP1+KCR1 2.0+*Gt*ACR1 (Fig 3.21b). The oocytes in group (4) exhibited significant membrane rupture due to fast water uptake after 20 minutes of green light illumination, but no changes were observed in the other groups. Expressing only two different channels did not cause oocytes to rupture. Only co-expression of AQP1, KCR1 2.0, and *Gt*ACR1 resulted in oocyte swelling until exploding, indicating the largest water transport efficiency among all groups (Fig 3.21c).

3.3.7 Light-induced oocyte shrinking in ND96 buffer via K^+/Cl^- efflux

In ND96 buffer, the expression of AQP1, KCR1 2.0, and *Gt*ACR1 in oocytes leads to observable shrinking when exposed to green light illumination, owing to the K^+/Cl^- efflux-induced osmotic gradient formation (Fig 3.22a). Expression of KCR1 2.0 and *Gt*ACR1 in oocytes facilitates K^+ efflux, which in turn makes the oocyte membrane potential more negative, promoting Cl^- efflux. To compare the osmotic gradient formed by K^+/Cl^- efflux, oocytes expressing (1) AQP1+*Gt*ACR1, (2) AQP1+KCR1 2.0, (3) KCR1 2.0+*Gt*ACR1, (4) AQP1+KCR1 2.0+*Gt*ACR1 were maintained in ND96 buffer, and 10 oocytes in each group were stimulated by green illumination (Fig 3.22b). After 20 minutes of illumination, cytoplasmic membrane separation from the vitelline membrane was significant in oocytes expressing (4) AQP1+KCR1 2.0+*Gt*ACR1, but no changes were observed in the other groups. This indicates that KCR1 2.0 and *Gt*ACR1 could rapidly produce an osmotic gradient, leading to accelerated water transport through AQP1. The expression of only two different channels did not cause oocyte shrinkage; only the co-expression of AQP1, KCR1 2.0, and *Gt*ACR1 induced

oocyte shrinkage. The results suggest that water transport efficiency was largest in oocytes co-expressing AQP1, KCR1 2.0, and *Gt*ACR1 compared to the other groups (Fig 3.22c).
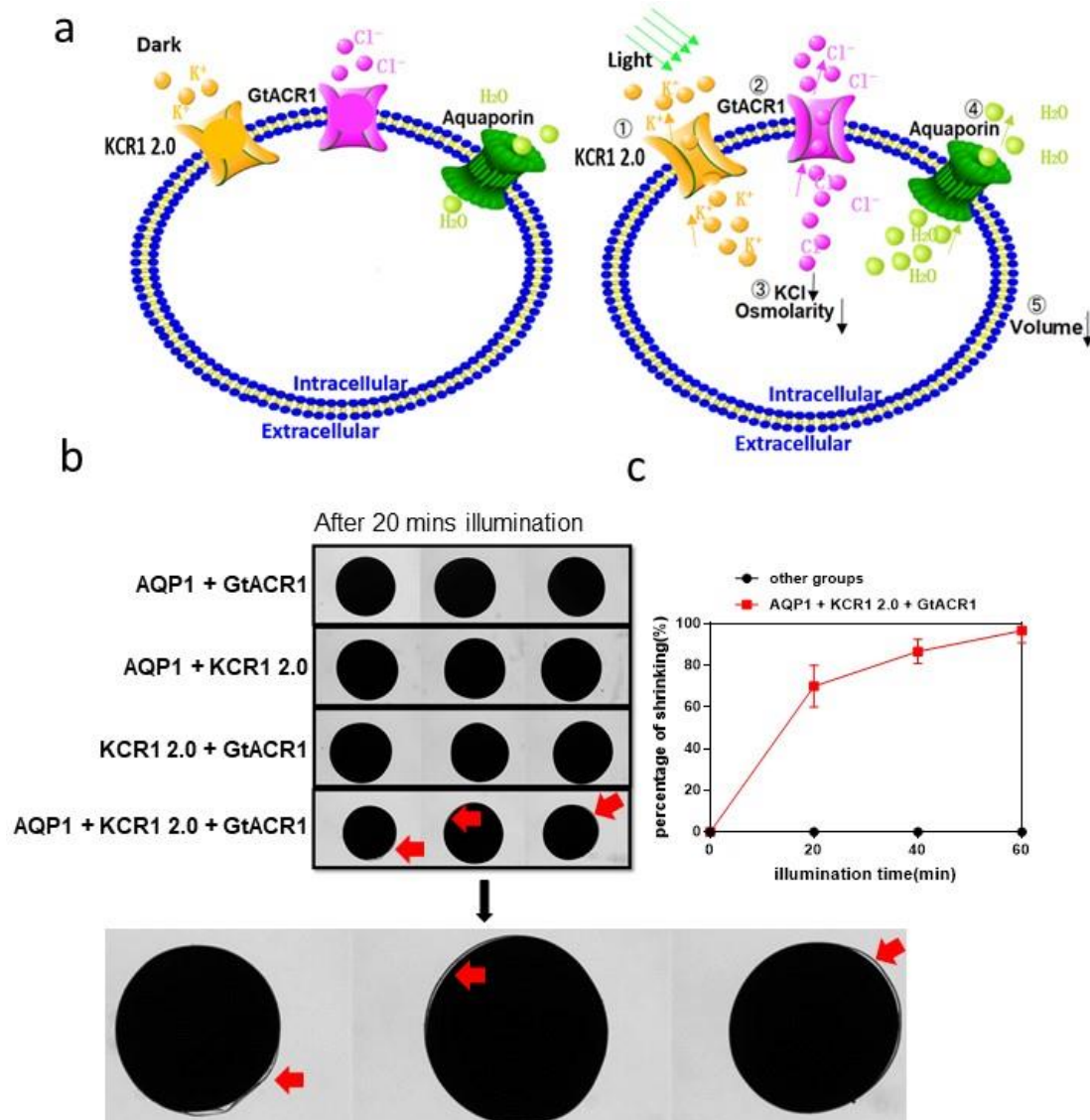
Figure 3.22 The Shrinking efficiency of KCR1 2.0 and *Gt*ACR1 expressed in *Xenopus* oocyte. (a) The schematic diagram shows the water transport through the AQP1 driven by the ion gradients created by the K^+ and Cl^- channels. Only the aquaporin AQP1 is constitutively active. KCR1 2.0 and *Gt*ACR1 channels are opened by the green light illumination. (b) The oocyte shrinking was indicated by the separation of the cytoplasmic membrane and the vitelline membrane at the red arrow-marked positions. The oocytes were illuminated for 20 min by 520 nm LEDs with light intensity of 1 mW/mm². cRNA amount: 5 ng AQP1, 20 ng KCR1 2.0, 5 ng *Gt*ACR1. (c) Oocytes shrinking efficacy after different times of green light illumination. The number of shrinking oocytes was recorded every 20 min. error bars = SEM, n = 6 groups, each with 10 oocytes.

4 Discussion

4.1 Improved KCR1 2.0 expand the optogenetic application

Traditional potassium ion channels are a fundamental component of cellular physiology and are classified as either ligand-gated or voltage-gated, with conserved pore-forming domains and K^+-selective filters. They also possess highly conserved K^+ channel signature sequences, which are primarily found in a variety of organisms including eukaryotic cells, bacteria, archaea, and viruses [52-55]. These channels are modulated by a range of factors including ligands, voltage, pH, membrane potential, and temperature [56-57].

KCR1, a newly identified light-gated potassium channel, exhibits fast kinetics and does not require an additional K^+-selective mechanism [58]. Light-gated potassium channels were discovered in the protist *Hyphochytrium catenoides* and, based on their distinct properties, two variants, KCR1 and KCR2, have been identified. Both KCR1 and KCR2 are channel rhodopsins, and their selectivity for K^+ is significantly larger than that for Na^+. Notably, KCR1 is active for a very brief period following photoactivation, with turn-on time of 1 ms [58-59]. The formation of electrochemical gradients contributes to membrane hyperpolarization in neurons, making KCR1 a powerful hyperpolarising tool. KCR1 is a promising tool for the investigation of neurological and cardiovascular diseases due to its utility in neuronal firing. Compared to KCR2, KCR1 has larger permeability to K^+ and a stronger hyperpolarizing effect. However, the current generated by KCR1 is weak. To address this, we aimed to increase the expression level of KCR1 and to enhance its current amplitude.

Various strategies have been implemented to enhance the performance of optogenetic tools. These strategies include: (1) identification of wild-type optogenetic tools present in nature based on gene sequences, such as PsChRd, Chrimson, and Chronos, among others; (2) identification of desired optogenetic tools by point mutations in gene sequences from large scale genetic mutations, including ChR2 (H134R) [47], ChR2 (ETA) [81], Jaw [23], ChrimsonR [73], and ChR2 (ET/TC) [98]; and molecular engineering of chimeras using different homologous genes, such as C1V1, ReaChR, and ChIEF, among others. However, these traditional strategies are time-consuming and appear to be less effective. In this study, we sought to enhance the performance of optogenetic tools by fusing different signal peptides to DNA sequences. These signal

peptides include LR, membrane trafficking, and ER export signal peptides. LR has been previously shown to enhance eGPCR expression in cell cultures [86], while the motif containing membrane trafficking and ER export signal peptide can increase channel currents. To optimize KCR1, we utilized a traffic signal peptide (T) and an ER export signal peptide (E) inserted between the eYFP at the C-terminal of KCR1. We also introduced eYFP between T and E to facilitate a semi-quantitative measurement of opsin expression level as an expression marker. In addition, we fused the LucyRho (LR) signal peptide to the N-terminal. This resulted in the development of KCR1 2.0 with enhanced performance. Based on light sensitivity experiments, the current of KCR1 2.0 was found to reach saturation at a green light intensity of approximately 1 mW/mm². The turn-on time of the KCR1 2.0 channel was measured to be less than 1 ms after light activation. Additionally, KCR1 2.0 demonstrated extremely reproducible evoked current waveforms when the light frequency was less than or equal to 1 Hz. Due to its large permeability ($P_K/P_{Na} \sim 24$), KCR1 2.0 serves as a powerful hyperpolarizing tool that can effectively inhibit neuronal firing in animals.

4.2 NCR1 2.0 is a new optogenetic tool

Motivated by the KCR1, we aligned the *H. catenoides* gene sequence with the KCR1 sequence as a template, and found that the NCR1 and KCR1 gene sequences are similar. I then optimized NCR1 by fusing LR at the N-terminal and T and E at the C-terminal, resulting in NCR1 2.0, which significantly improved the expression level and increased the current amplitude. Full-length NCR1 2.0 contains 432 amino acids. To investigate the effect of amino acid number on the properties of NCR1 2.0, we designed NCR1 2.0 (330), NCR1 2.0 (283), and NCR1 2.0 (273) by retaining the amino acid number at 330, 280, and 273, respectively. As the amino acid number decreased, the current increased in NCR1 2.0, with the maximum current observed in NCR1 2.0 (273).

In light sensitivity experiments, I observed that the current of NCR1 2.0 reaches saturation at a green light intensity of approximately 3 mW/mm². By shifting the action spectrum to different wavelengths, the maximum current of NCR1 2.0 (273) occurs when the light wavelength is around 520 nm. The reversal potential of NCR1 2.0 (273) differs in high Na$^+$, high K$^+$, and low Na$^+$/K$^+$ solutions, with the reversal potential in high Na$^+$ solution being Er (High Na$^+$) ~ +36 mV, in high K$^+$ solution being Er (High K$^+$) ~ -9 mV, and in low Na$^+$/K$^+$ being Er (Low Na$^+$/K$^+$) ~ -70 mV. Furthermore, the permeability ratio of Na$^+$ and K$^+$ for NCR1 2.0 (273) is P_{Na}/P_K ~ 5.8, which is larger

than that of XXM 2.0. The kinetics of NCR1 2.0 (273) show a faster turn-on time and a slower turn-off time under 50 ms green light illumination in the ORi Ca^{2+} solution. NCR1 2.0 exhibits an extremely reproducible current waveform when the frequency of the light is less than or equal to 2 Hz. To investigate the effect of mutations on the reversal potential and ion selectivity, I tested four mutations, namely NCR1 2.0 (273 D116H), NCR1 2.0 (273 D116E), NCR1 2.0 (283 V133H), and NCR1 2.0 (283 D116Q). Identification of NCR1 2.0 mutants revealed that the amino acids at positions 116 and 133 are crucial for NCR1 2.0 functionality, as mutations at these sites significantly affect NCR1 2.0 performance.

4.3 Optogenetic regulation of water flux in oocytes

In this study, we developed a system for light-regulating water transport in vitro by utilizing *Xenopus* oocytes, water channel proteins, and optogenetic tools. *Xenopus* oocytes have been widely used as a valuable tool for expressing and characterizing membrane proteins due to their advantageous features such as large size, easy culture, high reproductive rate, high expression efficiency, and relatively homogeneous structure. Dr. Ruijing Tang has also conducted similar research, which has greatly inspired me [38].

We designed water regulation models by utilizing *Xenopus* oocytes as a host cell, expressing water channel proteins heterologously, and utilizing optogenetic tools to control the water transport process. *Xenopus* oocytes represent an effective platform for the expression and characterization of diverse membrane proteins. By injecting different types of RNAs into the oocytes, I successfully expressed and stabilized a variety of channel proteins. Normally, water flows through endogenous water channels when osmotic pressure changes both internally and externally of the oocyte membrane. However, due to the limited number of endogenous water channels, the efficiency of water transport is relatively low. I co-expressed AQP1 with optogenetic tools in the oocytes to accelerate water flux. Overall, we designed three combinations (1: AQP1, XXM 2.0 and *Gt*ACR1. 2: AQP1, NCR1 2.0 and *Gt*ACR1. 3: AQP1, KCR1 2.0 and *Gt*ACR1.) of optogenetic tools to regulate the flow of water in *Xenopus* oocytes.

Optogenetic tools comprise of light-gated cation channels (XXM 2.0, KCR1 2.0, NCR1 2.0) and the light-gated anion channel *Gt*ACR1. Among them, the light-gated cation channels XXM 2.0 and NCR1 2.0 are primarily utilized to regulate Na^+ concentration

under illumination. The light-gated cation channel KCR1 2.0 is predominantly used to regulate K^+ concentration under illumination. The light-gated anion channel GtACR1 is mainly employed to regulate Cl^- concentration. NaCl or KCl concentration can be regulated by co-expressing the light-gated cation channel (XXM 2.0, KCR1 2.0, NCR1 2.0) and the light-gated anion channel GtACR1 on $Xenopus$ oocytes.

To create an osmotic gradient by altering the Na^+ concentration in $Xenopus$ oocytes, the light-gated cation channel NCR1 2.0 or XXM 2.0 was expressed, Co-expressing the light-gated anion channel GtACR1 in the oocytes further accelerates the osmotic gradient formation via Cl^- influx. To expedite osmotic gradient-based water transport, I expressed mammalian AQP1 in $Xenopus$ oocytes. In order to create an osmotic gradient by changing the K^+ concentration in $Xenopus$ oocytes, the light-gated cation channel KCR1 2.0 was expressed. Co-expressing the light-gated anion channel GtACR1 in the oocytes would further accelerate the formation of the osmotic gradient via Cl^- influx or efflux. The magnitude of the osmotic gradient is dictated by the influx or efflux of KCl, and regulates the swelling or shrinking of Xenopus oocytes. The regulation of water flow and the shrinking or swelling of the $Xenopus$ oocytes can only be achieved when water channel proteins (AQP1), light-gated cation channels, and light-gated anion channels are expressed together. The expression of either or both alone does not result in changes in $Xenopus$ oocytes morphology.

In summary, co-expression of XXM 2.0, NCR1 2.0, or KCR1 2.0 with GtACR1 and water channel AQP1 in vivo can effectively regulate water transport by light, thereby maintaining cytoplasmic isotonicity in relation to the surrounding environment. This combination of tools holds great potential for future studies of ion transport and water flux in various biological contexts, such as neurons, plant cells, and other related topics. Our experiment showed that combining these different tools was effective in manipulating osmotic gradients and driving water transport. This research opens up more opportunities for optogenetic manipulation and future studies of osmotic regulation and water transport in various biological contexts.

5 References

1. Preston, G.M., et al. "Appearance of Water Channels in *Xenopus* Oocytes Expressing Red Cell CHIP28 Protein." Science, vol. 256, 1992, p. 385-387.
2. Agre, P., et al. "Isolation of the cDNA for erythrocyte integral membrane protein of 28 kilodaltons: member of an ancient channel family." Proc Natl Acad Sci USA, vol. 88, 1991, p. 11110.
3. Cooper, G. The Cell: A Molecular Approach, ASM PRESS, 2009, p. 544.
4. Cooper, Geoffrey. The Cell. 2nd ed., Sinauer Associates, 2000, p. 117.
5. Lodish, Harvey et al. Molecular Cell Biology. 4th ed., W. H. Freeman, 2000.
6. Verkman, A.S. "Mammalian aquaporins: diverse physiological roles and potential clinical significance." Expert Rev Mol Med, vol. 10, 2008, p. e13.
7. Rojek, A., et al. "A current view of the mammalian aquaglyceroporins." Annu Rev Physiol, vol. 70, 2008, p. 301-327.
8. King, L.S., et al. "From structure to disease: the evolving tale of aquaporin biology." Nat Rev Mol Cell Biol, vol. 5, no. 9, 2004, p. 687-698.
9. Papadopoulos, M.C. and Verkman, A.S. "Aquaporin water channels in the nervous system." Nat Rev Neurosci, vol. 14, no. 4, 2013, p. 265-277.
10. Jung, J.S., et al. "Molecular structure of the water channel through aquaporin CHIP. The hourglass model." J Biol Chem, vol. 269, 1994, p. 14648-14654.
11. Kruse, E., et al. "The aquaporins." Genome Biol, vol. 7, no. 2, 2006, p. 206.
12. Walz, T., et al. "The three-dimensional structure of aquaporin-1." Nature, vol. 387, 1997, p. 624-627.
13. Saparov, S.M., et al. "Water and ion permeation of aquaporin-1 in planar lipid bilayers: major differences in structural determinants and stoichiometry." J Biol Chem, vol. 276, 2001, p. 31515-31520.
14. Yool, A.J. and Weinstein, A.M. "New roles for old holes: ion channel function in aquaporin-1." News Physiol Sci, vol. 17, 2002, p. 68-72.
15. Fu, Dongxue, et al. "Structure of a Glycerol-Conducting Channel and the Basis for Its Selectivity." Science, vol. 290, 2000, p. 481-486.
16. de Groot, BL, and H. Grubmuller. "Water permeation across biological membranes: mechanism and dynamics of aquaporin-1 and GlpF." Science, vol. 294, 2001, p. 2353-2357.
17. de Groot, BL, et al. "The mechanism of proton exclusion in the aquaporin-1 water channel." Journal of Molecular Biology, vol. 333, 2003, p. 279-293.
18. Chaumont, F., et al. "Plasma membrane intrinsic proteins from maize cluster in two sequence subgroups with differential aquaporin activity." Plant Physiology, vol. 122, 2000, p. 1025-1034.
19. Shimizu-Sato, S., et al. "A light-switchable gene promoter system." Nature Biotechnology, vol. 20, no. 10, 2002, p. 1041-1044.
20. Liu, X., et al. "Optogenetic stimulation of a hippocampal engram activates fear memory recall." Nature, vol. 484, no. 7394, 2012, p. 381-385.
21. Tanaka, R., et al. "Optogenetic Activation of the fruitless-Labeled Circuitry in Drosophila subobscura Males Induces Mating Motor Acts." The Journal of Neuroscience, vol. 37, no. 46, 2017, p. 11144-11155.
22. Musso, Pierre-Yves, et al. "Closed-loop optogenetic activation of peripheral or central neurons modulates feeding in freely moving Drosophila." eLife, vol. 8, 2019, p. e43963.
23. Guo, Z.V., et al. "Flow of cortical activity underlying a tactile decision in mice." Neuron, vol. 81, no. 1, 2014, p. 179-194.
24. Feng, Kai, et al. "Distributed control of motor circuits for backward walking in Drosophila." Nature Communications, vol. 11, no. 1, 2020, p. 6166.
25. Govorunova, Elena G., et al. "Natural light-gated anion channels: A family of microbial rhodopsins for advanced optogenetics." Science, vol. 349, no. 6248, 2015, p. 647-650.
26. Volkov, Oleg, et al. "Engineering Light-Gated Ion Channels." Biochemistry, vol. 45, no. 51, 2006, p. 15129-15141.
27. Nagel, Georg, et al. "Light Activation of Channelrhodopsin-2 in Excitable Cells of Caenorhabditis elegans Triggers Rapid Behavioral Responses." Current Biology, vol. 15, no. 24, 2005, p. 2279-2284.

28.   Nagel, G., et al. "Channelrhodopsin-1: a light-gated proton channel in green algae." Science, vol. 296, no. 5577, 2002, p. 2395-2398.

29.   Nagel, G., et al. "Channelrhodopsin-2, a directly light-gated cation-selective membrane channel." Proceedings of the National Academy of Sciences of the United States of America, vol. 100, no. 24, 2003, p. 13940-13945.

30.   Bamann, C., et al. "Spectral Characteristics of the Photocycle of Channelrhodopsin-2 and Its Implication for Channel Function." Journal of Molecular Biology, vol. 375, no. 3, 2008, p. 686-694.

31.   Kato, H.E., et al. "Crystal Structure of the Channelrhodopsin Light-gated Cation Channel." Nature, vol. 482, no. 7385, 2012, p. 369-374.

32.   Berndt, A., et al. "Bi-stable Neural State Switches." Nature Neuroscience, vol. 12, no. 2, 2009, p. 229-234.

33.   Dawydow, A., et al. "Channelrhodopsin-2-XXL, a Powerful Optogenetic Tool for Low-Light Applications." Proceedings of the National Academy of Sciences of the United States of America, vol. 111, no. 38, 2014, p. 13972-13977.

34.   Duan, X., et al. "Mutated Channelrhodopsins with Increased Sodium and Calcium Permeability." Applied Sciences, vol. 9, no. 4, 2019, p. 664.

35.   Wietek, J., et al. "Conversion of Channelrhodopsin into a Light-Gated Chloride Channel." Science, vol. 344, 2014, p. 409-412.

36.   Tang, Ruijing. "Optogenetic Methods to Regulate Water Transport and Purify Proteins." Dissertation, University of Wuerzburg, 2021.

37.   Govorunova, E.G., et al. "Extending the Time Domain of Neuronal Silencing with *Cryptophyte Anion Channelrhodopsins*." Journal of Neuroscience, vol. 38, no. 39, 2018, p. 8613-8624.

38.   Mauss, A.S., et al. "Optogenetic Neuronal Silencing in Drosophila during Visual Processing." Science, vol. 347, no. 6226, 2017, p. 977-982.

39.   Mohammad, F., et al. "Optogenetic Inhibition of Behavior with Anion Channelrhodopsins." Nature Methods, vol. 14, no. 3, 2017, p. 271-274.

40.   Steck, K., et al. "Internal Amino Acid State Modulates Yeast Taste Neurons to Support Protein Homeostasis in Drosophila." eLife, vol. 7, 2018, p. e32499.

41.   Forli, Andrea, et al. "Two-Photon Bidirectional Control and Imaging of Neuronal Excitability with High Spatial Resolution in Vivo." Nature Methods, vol. 15, no. 8, 2018, p. 657-660.

42.   Mahn, Maria, et al. "High-Efficiency Optogenetic Silencing with Soma-Targeted Anion-Conducting Channelrhodopsins." Nature Communications, vol. 9, no. 1, 2018, p. 4125.

43.   Messier, Jacob E., et al. "Targeting Light-Gated Chloride Channels to Neuronal Somatodendritic Domain Reduces Their Excitatory Effect in the Axon." Cell Reports, vol. 24, no. 12, 2018, p. 3189-3195.

44.   Wei, Yue-Chen, et al. "Medial Preoptic Area in Mice is Capable of Mediating Sexually Dimorphic Behaviors Regard less of Gender." Nature Communications, vol. 9, no. 1, 2018, p. 279.

45.   Mohamed, Gamal A., et al. "Optical Inhibition of Larval Zebrafish Behaviour with Anion Channelrhodopsins." PLoS ONE, vol. 12, no. 1, 2017, p. e0170275.

46.   Bergs, Alexander, et al. "Rhodopsin Optogenetic Toolbox v2.0 for Light-Sensitive Excitation and Inhibition in Caenorhabditis Elegans." PLoS ONE, vol. 13, no. 1, 2018, p. e0191802.

47.   Wojdyla, James A., et al. "Fast Two-Dimensional Grid and Transmission X-Ray Microscopy Scanning Methods for Visualizing and Characterizing Protein Crystals." Journal of Applied Crystallography, vol. 49, no. 3, 2016, p. 944-952.

48.   Li, Hai, et al. "Crystal Structure of a Natural Light-Gated Anion Channelrhodopsin." eLife, vol. 8, 2019, p. e41741.

49.   MacKinnon, Roderick. "Potassium Channels." FEBS Letters, vol. 555, no. 1, 2003, p. 62-65.

50.   Enyedi, Peter, and Gyorgy Czirjak. "Molecular Background of Leak K^+ Currents: Two-Pore Domain Potassium Channels." Physiological Reviews, vol. 90, no. 2, 2010, p. 559-605.

51.   Mackie, T. D., and J. L. Brodsky. "Investigating Potassium Channels in Budding Yeast: A Genetic Sandbox." Genetics, vol. 209, no. 3, 2018, p. 637-650.

52.   Mironenko, Andrii, et al. "The Persistent Question of Potassium Channel Permeation Mechanisms." Journal of Molecular Biology, vol. 433, no. 7, 2021, p. 167002.

53.   Govorunova, E.G., et al. "Kalium Channelrhodopsins are Natural Light-Gated Potassium Channels that Mediate Optogenetic Inhibition." Nat Neurosci, vol. 25, no. 7, 2022, p. 967-974.

54.   Leonard, G., et al. "Comparative Genomic Analysis of the 'Pseudofungus' Hyphochytrium catenoides." Open Biol, vol. 8, 2018, p. 170184.

55.   Zhang, Mengchen, et al. "Cryo-EM Structures of Kalium Channelrhodopsins KCRs." bioRxiv, 2022.

56.   Tucker, K., et al. "Cryo-EM Structures of the Channelrhodopsin ChRmine in Lipid Nanodiscs." Nat Commun, vol. 13, 2022, p. 4842.

57.   Kishi, K. E., et al. "Structural Basis for Channel Conduction in the Pump-Like Channelrhodopsin ChRmine." Cell, vol. 185, 2022, p. 672-689.

58.   Volkov, Oleg, et al. "Structural Insights into Ion Conduction by Channelrhodopsin 2." Science, vol. 358, 2017.

59.   Govorunova, E.G., et al. "Biophysical Characterization of Light-Gated Ion Channels Using Planar Automated Patch Clamp." Front Mol Neurosci, vol. 15, 2022.

60.   Oesterhelt, D. and W. Stoeckenius. "Rhodopsin-Like Protein from the Purple Membrane of Halobacterium halobium." Nat New Biol, vol. 233, 1971, p. 149-152.

61.   Lorenz-Fonfria, V.A., et al. "Transient Protonation Changes in Channelrhodopsin-2 and Their Relevance to Channel Gating." Proc Natl Acad Sci U S A, vol. 110, 2013, p. E1273.

62.   Kayushin, LP and VP Skulachev. "Bacteriorhodopsin as an electrogenic proton pump: reconstition of bacteriorhodopsin proteoliposomes generating delta psi and delta pH." FEBS Letters, vol. 39, no. 1, 1974, p. 39-42.

63.   Oesterhelt, D. and W. Stoeckenius. "Functions of a New Photoreceptor Membrane." Proceedings of the National Academy of Sciences of the United States of America, vol. 70, no. 10, 1973, p. 2853-2857.

64.   Racker, E. and W. Stoeckenius. "Reconstitution of Purple Membrane Vesicles Catalyzing Light-Driven Proton Uptake and Adenosine Triphosphate Formation." The Journal of Biological Chemistry, vol. 249, no. 2, 1974, p. 662-663.

65.   Mitchell, P. "Keilin's Respiratory Chain Concept and Its Chemiosmotic Consequences." Science, vol. 206, no. 4423, 1979, p. 1148-1159.

66.   Takeda, K. et al. "A Novel Three-Dimensional Crystal of Bacteriorhodopsin Obtained by Successive Fusion of the Vesicular Assemblies." Journal of Molecular Biology, vol. 283, 1998, p. 463-474.

67.   Pebay-Peyroula, E. et al. "X-ray Structure of Bacteriorhodopsin at 2.5 Angstroms from Microcrystals Grown in Lipidic Cubic Phases." Science, vol. 277, 1997, p. 1676-1681.

68.   Mitsuoka, K. et al. "The Structure of Bacteriorhodopsin at 3.0 A Resolution Based on Electron Crystallography: Implication of the Charge Distribution." Journal of Molecular Biology, vol. 286, 1999, p. 861-882.

69.   Luecke, H. et al. "Structure of Bacteriorhodopsin at 1.55 a Resolution." Journal of Molecular Biology, vol. 291, 1999, p. 899-911.

70.   Kimura, Y. et al. "Surface of bacteriorhodopsin revealed by high-resolution electron crystallography." Nature, vol. 389, 1997, p. 206-211.

71.   Grigorieff, N., Ceska, T. A., Downing, K. H., Baldwin, J. M. & Henderson, R. "Electron-crystallographic refinement of the structure of bacteriorhodopsin." Journal of Molecular Biology, vol. 259, 1996, p. 393-421.

72.   Essen, L., Siegert, R., Lehmann, and W. D. & Oesterhelt, D "Lipid patches in membrane protein oligomers: crystal structure of the bacteriorhodopsin-lipid complex." Science, vol. 285, no. 5430, 1999, p. 522-525.

73.   Waschuk, S.A., et al. "Leptosphaeria rhodopsin: bacteriorhodopsin-like proton pump from a eukaryote." Proc Natl Acad Sci U S A, vol. 102, no. 19, 2005, p. 6879-6883.

74.   Ihara, K., et al. "Evolution of the archaeal rhodopsins: evolution rate changes by gene duplication and functional differentiation." Journal of Molecular Biology, vol. 285, no. 1, 1999, p. 163-174.

75. Chow, B.Y., et al. "High-performance genetically targetable optical neural silencing by light-driven proton pumps." Nature, vol. 463, no. 7277, 2010, p. 98-102.

76. Avelar, G. M. et al. "A rhodopsin-guanylyl cyclase gene fusion functions in visual perception in a fungus." Current Biology, vol. 24, no. 11, 2014, p. 1234-1240.

77. Inoue, Keiichi, et al. "A Natural Light-Driven Inward Proton Pump." Nat Commun, vol. 7, 2016, p. 13415.

78. Shevchenko, Vitaliy, et al. "Inward H^+ Pump Xenorhodopsin: Mechanism and Alternative Optogenetic Approach." Sci Adv, vol. 3, no. 9, 2017, p. e1603187.

79. Nagel, G., et al. "Functional expression of bacteriorhodopsin in oocytes allows direct measurement of voltage dependence of light induced H^+ pumping." FEBS Letters, vol. 377, no. 2, 1995, p. 263-266.

80. Matsuno-Yagi, A., and Y. Mukohata. "Two Possible Roles of Bacteriorhodopsin; a Comparative Study of Strains of Halobacterium Halobium Differing in Pigmentation." Biochem Biophys Res Commun, vol. 78, no. 1, 1977, p. 237-243.

81. Mukohata, Y., and Y. Kaji. "Light-induced Membrane-potential Increase, ATP Synthesis, and Proton Uptake in Halobacterium halobium, R1mR Catalyzed by Halorhodopsin: Effects of N, N'-dicyclohexylcarbodiimide, Triphenyltin Chloride, and 3, 5-di-tert-butyl-4-hydroxybenzylidenemalononitrile (SF6847)." Arch Biochem Biophys, vol. 206, no. 1, 1981, p. 72-76.

82. Greene, R.V., and J.K. Lanyi. "Proton Movements in Response to a Light-driven Electrogenic Pump for Sodium Ions in Halobacterium halobium Membranes." J Biol Chem, vol. 254, no. 21, 1979, p. 10986-10994.

83. MacDonald, R.E., et al. "Characterization of the Light-driven Sodium Pump of Halobacterium halobium. Consequences of Sodium Efflux as the Primary Light-driven Event." J Biol Chem, vol. 254, no. 23, 1979, p. 11831-11838.

84. Schobert, B., and J.K. Lanyi. "Halorhodopsin is a Light-driven Chloride Pump." J Biol Chem, vol. 257, no. 17, 1982, p. 10306-10313.

85. Barnberg, E., et al. "The Chromoprotein of Halorhodopsin is the Light-driven Electrogenic Chloride Pump in Halobacterium halobiumt." Biochemistry, vol. 23, no. 25, 1984, p. 6216-6221.

86. Bivin, D.B., and W. Stoeckenius. "Photoactive Retinal Pigments in Haloalkaliphilic Bacteria." J Gen Microbiol, vol. 132, no. 8, 1986, p. 2167-2177.

87. Duschl, A., et al. "Properties and Photochemistry of a Halorhodopsin from the Haloalkalophile, Natronobacterium pharaonis." J Biol Chem, vol. 265, no. 3, 1990, p. 1261-1267.

88. Zhang, F., et al. "Multimodal Fast Optical Interrogation of Neural Circuitry." Nature, vol. 446, no. 7136, 2007, p. 633-639.

89. Gradinaru, V., et al. "Molecular and Cellular Approaches for Diversifying and Extending Optogenetics." Cell, vol. 141, no. 1, 2010, p. 154-165.

90. Zhao, S., et al. "Improved Expression of Halorhodopsin for Light-Induced Silencing of Neuronal Activity." Brain Cell Biology, vol. 36, no. 1-4, 2008, p. 141-154.

91. Gradinaru, V., et al. "eNpHR: A Natronomonas Halorhodopsin Enhanced for Optogenetic Applications." Brain Cell Biology, vol. 36, no. 1-4, 2008, p. 129-139.

92. Blanck, A. and D. Oesterhelt. "The Halo-opsin Gene. II. Sequence, Primary Structure of Halorhodopsin and Comparison with Bacteriorhodopsin." EMBO Journal, vol. 6, no. 1, 1987, p. 265-273.

93. Lanyi, J.K., et al. "The Primary Structure of a Halorhodopsin from Natronobacterium pharaonis. Structural, Functional and Evolutionary Implications for Bacterial Rhodopsins and Halorhodopsins." Journal of Biological Chemistry, vol. 265, no. 3, 1990, p. 1253-1260.

94. Kolbe, M., et al. "Structure of the Light-Driven Chloride Pump Halorhodopsin at 1.8 A Resolution." Science, vol. 288, no. 5470, 2000, p. 1390-1396.

95. Kouyama, T., et al. "Crystal Structure of the Light-Driven Chloride Pump Halorhodopsin from Natronomonas Pharaonis." Journal of Molecular Biology, vol. 396, no. 3, 2010, p. 564-579.

96. Yang, Shang. "Characterization and Engineering of Photoreceptors with Improved Properties for Optogenetic Application." University of Wuerzburg, PhD thesis, 2022.

97.   Engelhard, C., et al. "Microbial Halorhodopsins: Light-Driven Chloride Pumps." Chemical Reviews, vol. 118, no. 21, 2018, p. 10629-10645.

98.   Kouyama, T., et al. "Crystal Structures of the L1, L2, N, and O States of Pharaonis Halorhodopsin." Biophysical Journal, vol. 108, no. 11, 2015, p. 2680-2690.

99.   Chuong, A.S., et al. "Noninvasive Optical Inhibition with a Redshifted Microbial Rhodopsin." Nature Neuroscience, vol. 17, no. 8, 2014, p. 1123-1129.

100.   Han X., Boyden E.S. Multiple-color optical activation, silencing, and desynchronization of neural activity, with single-spike temporal resolution. PLoS One. 2007; 2: e299.

101.   Sato, M., et al. "Stopped-Flow Analysis on Anion Binding to Blue-Form Halorhodopsin from Natronobacterium pharaonis: Comparison with the Anion-Uptake Process during the Photocycle." Biochemistry, vol. 41, 2002, p. 2452-2458.

102.   Bálint, Z., M. Lakatos, and G. Váró. "The Nitrate Transporting Photochemical Reaction Cycle of the Pharaonis Halorhodopsin." Biophysical Journal, vol. 86, 2004, p. 1655-1663.

103.   Hazemoto, N., N. Kamo, and Y. Terayama. "Effect of Salt on Photocycle and Ion-Pumping of Halorhodopsin and Third Rhodopsinlike Pigment of Halobacterium halobium." Biophysical Journal, vol. 45, 1984, p. 1073-1077.

104.   Seki, A., S. Miyauchi, and N. Kamo. "Heterologous Expression of Pharaonis Halorhodopsin in *Xenopus laevis* Oocytes and Electrophysiological Characterization of its Light-Driven Cl- Pump Activity." Biophysical Journal, vol. 92, 2007, p. 2559-2569.

105.   Mattis, J., K.M. Tye, and K. Deisseroth. "Principles for Applying Optogenetic Tools Derived from Direct Comparative Analysis of Microbial Opsins." Nature Methods, vol. 9, 2011, p. 159-172.

106.   Besaw JE, Ou WL, Morizumi T, Eger BT, Sanchez Vasquez JD, Chu JHY, Harris A, Brown LS, Miller RJD, Ernst OP. "The crystal structures of a chloride-pumping microbial rhodopsin and its proton-pumping mutant illuminate proton transfer determinants." Journal of Biological Chemistry, vol. 295, no. 44, 2020, p. 14793-14804.

107.   Vonck J. "Structure of the bacteriorhodopsin mutant F219L N intermediate revealed by electron crystallography." EMBO Journal, vol. 19, no. 10, 2000, p. 2152-2160.

108.   Váró G, Brown LS, Lakatos M, Lanyi JK. "Characterization of the photochemical reaction cycle of proteorhodopsin." Biophysical Journal, vol. 84, no. 2 Pt 1, 2003, p. 1202-1207.

109.   Livnah N, Sheves M. "The Schiff base bond configuration in bacteriorhodopsin and in model compounds." Biochemistry, vol. 32, no. 28, 1993, p. 7223-7228.

110.   Fodor SPA, Ames JB, Gebhard R, van den Berg EMM, Stoeckenius W, Lugtenburg J, Mathies RA. "Chromophore structure in bacteriorhodopsin's N intermediate: implications for the proton-pumping mechanism." Biochemistry, vol. 27, no. 18, 1988, p. 7097-7101.

111   Inoue, K., et al. "A light-driven sodium ion pump in marine bacteria." Nature Communications, vol. 4, 2013, p. 1678.

112.   Gushchin, I., et al. "Structure of the light-driven sodium pump KR2 and its implications for optogenetics." FEBS Journal, vol. 283, no. 7, 2016, p. 1232-1238.

113.   Gushchin, I., et al. "Crystal structure of a light-driven sodium pump." Nature Structural & Molecular Biology, vol. 22, no. 5, 2015, p. 390-395.

114.   Kandori, H., K. Inoue, and S.P. Tsunoda. "Light-Driven Sodium-Pumping Rhodopsin: A New Concept of Active Transport." Chemical Reviews, vol. 118, no. 21, 2018, p. 10646-10658.

115.   Kato, H.E., et al. "Structural basis for Na^+ transport mechanism by a light-driven Na^+ pump." Nature, vol. 521, no. 7550, 2015, p. 48-53.

116.   Kovalev, K., et al. "Structure and Mechanisms of Sodium-Pumping KR2 Rhodopsin." Science Advances, vol. 5, no. 4, 2019, p. 2671.

117.   Kandori, H., K. Inoue, and S.P. Tsunoda. "Light-Driven Sodium Pumping Rhodopsin: A New Concept of Active Transport." Chemical Reviews, vol. 118, no. 21, 2018, p. 10646-10658.

118.   Balashov, S.P., et al. "Light-Driven Na^+ Pump from Gillisia limnaea: A High-Affinity Na^+ Binding Site is Formed Transiently in the Photocycle." Biochemistry, vol. 53, no. 48, 2014, p. 7549-7561.

119.   Beja, O. and J.K. Lanyi. "Nature's Toolkit for Microbial Rhodopsin Ion Pumps." Proceedings of the National Academy of Sciences of the United States of America, vol. 111, no. 18, 2014, p. 6538-6539.

120. Tsunoda, S.P., et al. "Functional Characterization of Sodium-Pumping Rhodopsins with Different Pumping Properties." PLoS One, vol. 12, no. 7, 2017, p. e0179232.
121. Zhao, H., et al. "Coexistence of Light-Driven Na^+ and H^+ Transport in a Microbial Rhodopsin from Nonlabens dokdonensis." Journal of Photochemistry and Photobiology B: Biology, vol. 172, 2017, p. 70-76.
122. Grimm, C., et al. "Electrical Properties, Substrate Specificity and Optogenetic Potential of the Engineered Light-Driven Sodium Pump eKR2." Scientific Reports, vol. 8, no. 1, 2018, p. 9316.
123. Gao, S., et al. "Optogenetic Manipulation of cGMP in Cells and Animals by the Tightly Light-Regulated Guanylyl-Cyclase Opsin CyclOp." Nature Communications, vol. 6, 2015, p. 8046.
124. Scheib, Ulrike, et al. "The Rhodopsin-Guanylyl Cyclase of the Aquatic Fungus Blastocladiella Emersonii Enables Fast Optical Control of cGMP Signaling." Science Signaling, vol. 8, no. 389, 2015, p. 8.
125. Sueki, A., et al., Systematic Localization of Escherichia coli Membrane Proteins, mSystems, 2020. 5(2): e00808-19.
126. Tian, Yang, et al. "A Novel Rhodopsin Phosphodiesterase from Salpingoeca Rosetta Shows Light-Enhanced Substrate Affinity." Biochemical Journal, vol. 475, no. 6, 2018, p. 1121-1128.
127. Tian, Yang, et al. "Two-Component Cyclase Opsins of Green Algae Are ATP-Dependent and Light-Inhibited Guanylyl Cyclases." BMC Biology, vol. 16, no. 1, 2018, p. 144.
128. Bear, Mark F., et al., editors. Neuroscience: Exploring the Brain. 3rd ed., Lippincott Williams & Wilkins, 2006, p. 84.
129. Moore, Jeffrey W., and Michael L. Hines. "A Brief History of Computational Neuroscience." Simulations with NEURON, Duke University, 1994.
130. Hernández-Ochoa, Erick O., and Martin F. Schneider. "Voltage Clamp Methods for the Study of Membrane Currents and SR Ca2+ Release in Adult Skeletal Muscle Fibers." Progress in Biophysics and Molecular Biology, vol. 108, no. 3, 2012, p. 98-118.
131. Kandel, Eric R., et al., editors. Principles of Neural Science. 4th ed., McGraw-Hill, 2000, p. 152-153.
132. Guan, Bo, et al. "Two-Electrode Voltage Clamp." Methods in Molecular Biology, vol. 998, 2013, p. 79-89.
133. Polder, H. R., and Dieter Swandulla. "The Use of Control Theory for the Design of Voltage Clamp Systems: A Simple and Standardized Procedure for Evaluating System Parameters." Journal of Neuroscience Methods, vol. 109, no. 2, 2001, p. 121-134.
134. Shepard, B.D., et al. "A Cleavable N-Terminal Signal Peptide Promotes Widespread Olfactory Receptor Surface Expression in HEK293T Cells." PLoS ONE, vol. 8, no. 7, 2013, p. e68758. 134
135. Kleinlogel, S., et al. "A gene-fusion strategy for stoichiometric and co-localized expression of light-gated membrane proteins." Nat Methods, vol. 8, no. 12, 2011, p. 1083-1088.
136. Beck, S., et al. "Synthetic Light-Activated Ion Channels for Optogenetic Activation and Inhibition." Front Neurosci, vol. 12, 2018, p. 643.

6 Appendix

6.1 Supplement Table

Table S1. List of primers used in this study

KCR1 Bh5F	CGCGGATCCATGCCCTTTTACGAT	For constructs KCR1
KCR1 TM4R	ATGAACCAGCAGCAACCCAGAG	For constructs KCR1
NCR1-10 Bh5F	CGGGATCCGGATGGCACCACGGCAGCAT	For constructs NCR1
NCR1 HD3R	CTCCGCTCGAGTGCCATGGC	For constructs NCR1
NCR1 Bh5F	CGGGATCCATGCCTTTCTGTGGT	For constructs NCR1
NCR1 330 XhR	CCGCTCGAGTGTGGCGCTAGACAGAACCT	For constructs NCR1
NCR1 283 XhR	CCGCTCGAGGCCAGGTCCAGCAAGGTGCT	For constructs NCR1
NCR1 D116Q qcF	CTGCTGCAAGTGCTGTATACCCTGGAA	For NCR1 mutation
NCR1 D116Q qcR	ACAGCACTTGCAGCAGGATCAGAGGAC	For NCR1 mutation
NCR1 D133H qcF	GTTCGCCCACATCATCACCCTTTGGFG	For NCR1 mutation
NCR1 D133H qcR	GATGATGTGGGCGAACACGAATCTC	For NCR1 mutation
NCR1 D116H qcF	CTGCTGCACGTGCTGTATACCCTGGAA	For NCR1 mutation
NCR1 D116H qcR	ACAGCACGTGCAGCAGGATCAGAGGAC	For NCR1 mutation
NCR1 D116E qcF	CTGCTGGAAGTGCTGTATACCCTGGAA	For NCR1 mutation
NCR1 D116E qcR	ACAGCACTTCCAGCAGGATCAGAGGAC	For NCR1 mutation

6.2 Supplement Figure
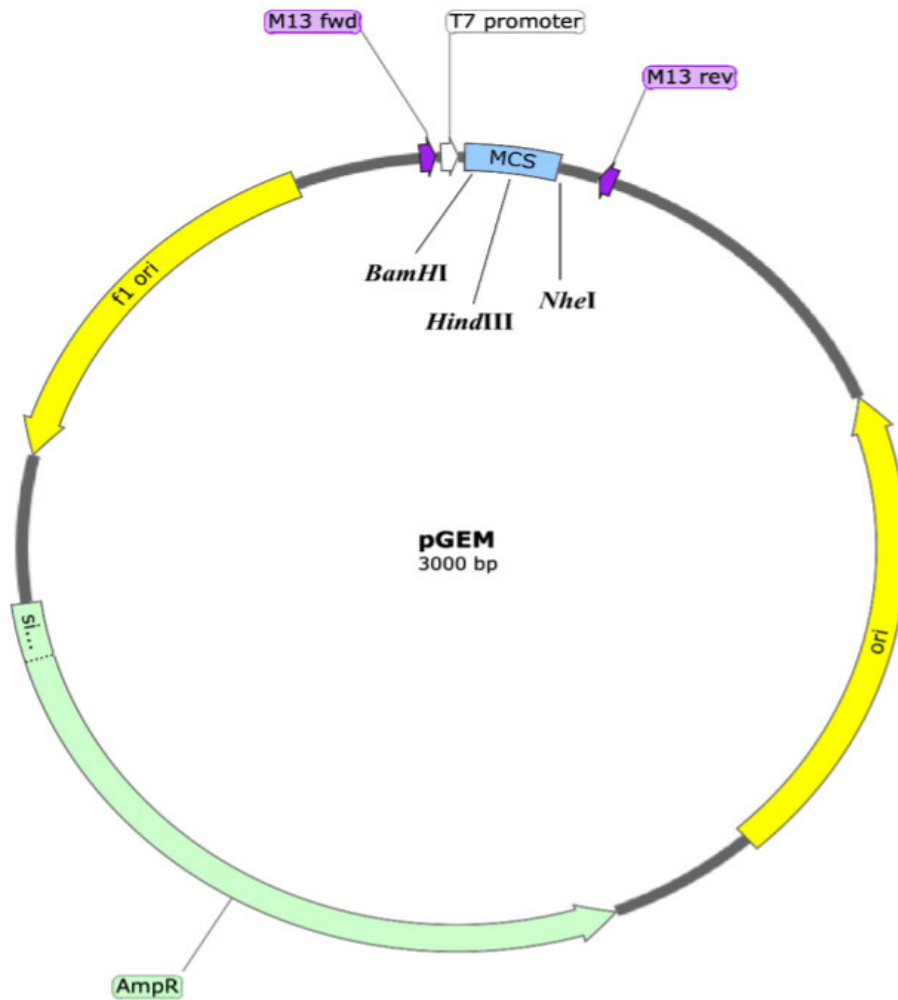
Figure S1. The map of vector pGEM.

The vector is pGEM. The plasmids are linearised by NheI enzyme cleavage. The transcription start site is the T7 promoter. The target gene is linked between BamHIand Hind III in the multiple cloning site (MCS) region.

6.3 Abbreviation

aa	amino acid
ACR	anion channel rhodopsin
AQP1	Aquaporin1
BLUF	sensors of blue light using FAD
bp	base pair
ChR	Channelrhodopsin
cRNA	complimentary ribonucleic acid
dNTP	deoxynucleotide triphosphate
E	ER export signal
kb	kilobase
KCR	Potassium channel rhodopsin
kDa	kilodalton
LB	Lysogeny broth
LR	Leucine rich
mRNA	messenger RNA
mV	MilliVolt
mW	MilliWatt
NCR	Sodium channel rhodopsin
NMG	N-Methyl-(D)-Glutamine
NpHR	Natronomonas pharaonis named
PCR	polymerase chain reaction
RNA	ribonucleic acid
T	Trafficking signal
TEVC	Two Electrode Voltage Clamp
WT	wild type
YFP	yellow fluorescent protein

Affidavit

Eidesstattliche Erklärungen nach §7 Abs. 2 Satz 3, 4, 5
der Promotionsordnung der Fakultät für Biologie

Eidesstattliche Erklärung

Hiermit erkläre ich an Eides statt, die Dissertation: „**Optogenetische Regulation der Osmolarität und des Wasserflusses**", eigenständig, d. h. insbesondere selbständig und ohne Hilfe eines kommerziellen Promotionsberaters, angefertigt und keine anderen, als die von mir angegebenen Quellen und Hilfsmittel verwendet zu haben.

Ich erkläre außerdem, dass die Dissertation weder in gleicher noch in ähnlicher Form bereits in einem anderen Prüfungsverfahren vorgelegen hat.

Weiterhin erkläre ich, dass bei allen Abbildungen und Texten bei denen die Verwertungsrechte (Copyright) nicht bei mir liegen, diese von den Rechtsinhabern eingeholt wurden und die Textstellen bzw. Abbildungen entsprechend den rechtlichen Vorgaben gekennzeichnet sind sowie bei Abbbildungen, die dem Internet entnommen wurden, der entsprechende Hypertextlink angegeben wurde.

Affidavit

I hereby declare that my thesis entitled: „**Optogenetic regulation of osmolarity and water flux**" is the result of my own work. I did not receive any help or support from commercial consultants. All sources and / or materials applied are listed and specified in the thesis.

Furthermore I verify that the thesis has not been submitted as part of another examination process neither in identical nor in similar form.

Besides I declare that if I do not hold the copyright for figures and paragraphs, I obtained it from the rights holder and that paragraphs and figures have been marked according to law or for figures taken from the internet the hyperlink has been added accordingly.

Würzburg, den_____

_____

Signature PhD-student

Curriculum Vitae

Publications

1. **Lin F**, Tang R, Zhang C, Scholz N, Nagel G, Gao S. Combining different ion-selective channelrhodopsins to control water flux by light. 05 May 2023, PREPRINT (Version 1) available at Research Square [https://doi.org/10.21203/rs.3.rs-2880071/v1]. **This publication originated from my thesis, (Under review).**

2. Dong H, **Lin F**, Boccaccini A R, et al. Corrosion behavior of biodegradable metals in two different simulated physiological solutions: Comparison of Mg, Zn and Fe [J]. Corrosion Science, 2021, 182:109278.

3. **Lin F**, Wang X, Wang Y, et al. Preparation and biocompatibility of electrospinning PDLLA/β-TCP/collagen for peripheral nerve regeneration[J]. RSC advances, 2017, 7(66): 41593-41602.

4. Zhu R, Wang X, Yang J, Wang Y, **Lin F**. Influence of hydroxyl-terminated polydimethylsiloxane on high-strength biocompatible polycarbonate urethane films.[J]. Biomedical Materials, 2017, 12(1):015011.

5. Wang Y, Wang X, Shi J, Rong Zhu, Zongrui Zhang, **Fei Lin**, Jing Yang, Mamoru Mizuno. A Biomimetic Silk Fibroin/Sodium Alginate Composite Scaffold for Soft Tissue Engineering [J]. Scientific Reports, 2016, 6:39477.